PHOTOMECHANICS OF POLYMERS AND ITS APPLICATIONS TO ACTIVE STRUCTURES AND ADDITIVE MANUFACTURING

A Dissertation
Presented to
The Academic Faculty

by

Xiaoming Mu

In Partial Fulfillment
of the Requirements for the Degree
Doctor of Philosophy in the
George W. Woodruff School of Mechanical Engineering

Georgia Institute of Technology
August 2017

PHOTOMECHANICS OF POLYMERS AND ITS APPLICATIONS TO ACTIVE STRUCTURES AND ADDITIVE MANUFACTURING

Approved by:

Dr. H. Jerry Qi, Advisor
School of Mechanical Engineering
Georgia Institute of Technology

Dr. Shuman Xia
School of Mechanical Engineering
Georgia Institute of Technology

Dr. Karl I. Jacob
School of Materials Science and
Engineering
Georgia Institute of Technology

Dr. Chuck Zhang
School of Industrial and Systems
Engineering
Georgia Institute of Technology

Dr. Julien Meaud
School of Mechanical Engineering
Georgia Institute of Technology

Date Approved: July 12, 2016

Dedicated to my loving family

ACKNOWLEDGEMENTS

I would like to express my sincere appreciation to my academic advisor Dr. Jerry Qi for his constant support and guidance of my Ph.D. study, for his patience, motivation, and immense knowledge, for the opportunities he provided me with, and for the trust in me. I would also like to thank all my thesis committee: Dr. Karl Jacob, Dr. Julien Meaud, Dr. Shuman Xia, and Dr. Chuck Zhang, who devoted their precious time to serve in my Ph.D. proposal and defense committees, and provided tremendous support to my ongoing research activity by sharing their expertise, insights, and instruments.

I would also like to thank Prof. Patrick Mather, Prof. Christopher Bowman, Prof. Jianliang Xiao and Prof. Devatha Nair. They inspire me greatly with their knowledge, passion, intelligence and patience. I am also thankful to all my previous and current lab members, who have contributed to the excellent working environment and the perfect collaboration in our group. Particularly, I would like to thank Prof. Kai Yu, Jiangtao Wu, Prof. Yiqi Mao, Zeang Zhao, Dr. Hua Yang, Conner Dunn, Chao Yuan, Ming Lei, Dr. Xiao Kuang, Craig Hamel, Devin Roach, Thompson Bertron, and Vincent Li for their helpful discussion at different stages of my research.

Finally, I would like to thank my family who sacrifice their time, and support me with their love and encouragement in all my pursuits. For my loving, supportive, and patient wife Xu Zhang who gave birth to our lovely son Eason, making my Ph.D. experience full of joy and enthusiasm.

TABLE OF CONTENTS

LIST OF TABLES

LIST OF FIGURES

LIST OF SYMBOLS AND ABBREVIATIONS

The following table lists universal abbreviations and symbols used in this dissertation

Abbreviations

LAPs	Light Activated Polymers
SMPs	Shape Memory Polymers
LCEs	Liquid Crystal Elastomers
DLP	Digital Light Processing
CANs	Covalently Adaptive Networks
1D	One Dimensional
2D	Two Dimensional
3D	Three Dimensional
AM	Additive Manufacturing
3DP	3D Printing
SME	Shape Memory Effect
BERs	Bond Exchange Reactions
SLA	Stereolithography
CLIP	Continuous Liquid Interface Production
FDM	Fused Deposition Modelling
SLS	Selective Laser Sintering
CAD	Computer Aided Design
DIW	Direct Ink Write
WLF equation	Williams-Landel-Ferry Equation
SEM	Scanning Electron Microscope

Symbols

T_g Glass Transition Temperature

T_m Melting Temperature

T_c Crystallization Temperature

K_B Boltzman's Constant

R Gas Constant

E_L Modulus of LAPs

E_N Modulus of NOA65

C_I Photoinitiator Concentration

C_R Radical Concentration

T_M WLF Reference Temperature

E_l Loss Modulus

E_s Storage Modulus

$tan\ \delta$ Ratio between Loss and Storage Modulus

SUMMARY

Photopolymer is responsive to ultraviolet or visible light and changes its properties for various applications such as actuation, shape morphing and additive manufacturing. Compared to thermal polymerization, photopolymerization has the similar propagation, termination and chain transfer steps while the initiation step is photoinduced. The objectives of this dissertation research are to study the photomechanics of polymers including light activated polymer and two stage reactive polymer, and explore their applications in photoinduced actuation, material property evolutions, and 3D printing of porous polymers. For the photomechanical study of light activated polymers, a constitutive model based on phase evolution theory is developed to capture the photoinduced stress relaxation. A laminated composite is designed to achieve photo-induced bending in a free-standing state. For two-stage reactive polymers, a photo-thermoviscoelastic model is developed to describe the significant property change during the 2nd stage evolution and the photoinduced viscoelasticity observed in the experiments. Moreover, various photopolymers are mixed with salt particulates to 3D print a polymer-salt composite which can be immersed in water to leach salts and generate pores. Porous polymer structures with 74% porosity can be 3D printed with the advantages of self-supporting, biocompatibility and shape memory effect. The porous parts can be infiltrated by secondary materials to improve the strength or become conductive, and be metalized by electroless nickel plating. In summary, this dissertation presents the study of light interactions with polymers focusing on actuation, property control and 3D printing of functional porous polymers.

CHAPTER 1.   INTRODUCTION

1.1   Background

1.1.1   Overview

Light is essential as the source of energy for living creatures on earth and it is widely used in photopolymerization or as a trigger to actuate active structures. Compared to other external stimuli, such as heat,[1-14] pH,[15-20] humidity,[21-23] magnetic field,[24-27], light provides unique advantages including remote control, localized irradiation, instant pause and resume.[28-38] Spatial activation can be simply achieved by using a photo-mask and adding additives in the polymer formula. The photochemical reaction can be manipulated easily by controlling the light intensity and irradiation time. Various smart materials have been developed to be photo-responsive with individual molecular mechanisms. Besides light triggered actuations, light has been utilized to synthesize thermoset polymers with the general advantages such as fast and localized curing with energy efficiency. Applications including soft active structures, two-stage reactive polymers with tunable material properties, and 3D printing of functional materials are demonstrated in this dissertation. Here, we focus on the photomechanics of polymerization and its applications to active structures and additive manufacturing. The photomechanical model of light activated polymer (LAP) and its laminated composite are presented, followed by the development of a photoviscoelastic model of two-stage reactive polymers whose material property can be improved significantly after 2nd stage reaction. The photomechanical behaviors of both polymers are studied by conducting experiments and comparing with simulation results. To broaden the functionality of the 3D printed photopolymers, porous polymeric structures

are fabricated by using a customized digital light processing (DLP) 3D printer. The innovative functionalities of the porous structures are demonstrated by infiltrating the porous template with secondary materials and metallizing the polymeric foam through electroless nickel plating.

1.1.2   Light Activated Polymers

Smart materials are a class of active materials that respond to external stimuli. If light is used as the stimulus, the active polymers are referred as light activated polymers. Various molecular mechanisms have been developed to achieve photo-actuation. Probably the most well-known one is liquid crystal elastomer (LCE),[39-45] which contains ordered rod-like structures comprised of *trans*-azobenzene moieties. When LCEs are irradiated with the proper wavelength of light, the ordered nematic phase of *trans* form and the disordered isotropic phase of *cis* form can be transformed from one to another, causing a macroscopic contraction or expansion.[33, 46] Despite LCEs, other polymer systems have also been explored by researchers. Lendlein et al.[29] developed a covalently crosslinked polymer with photo-tunable molecular crosslinks that respond to light as shown in Figure 1(a). Secondary crosslinks can be formed and cleaved upon irradiation of light at wavelength longer and shorter than 260 nm, respectively. The group of these secondary crosslinks can be used to achieve shape memory effect when coupled with mechanical deformation. Scott *et al*.[47, 48] developed amorphous covalently adaptive networks (CANs) where bond exchange reactions (BERs) are initiated by free radicals generated by photo-cleavage of the embedded photoinitiators in the polymer formula. In one BER, a polymer chain end with free radical first adds into an existing bond forming a tertiary radical structure before fragmentation of an adjacent bond and transfer that radical to the new free

chain as shown in Figure 1(b). As the same reactions continue, the entire polymer network is rearranged until radical termination occurs. The polymer network rearrangement ends up with altering the network structure and restoring the network to its highest entropy configuration thus relaxes any preprogrammed stress macroscopically. In summary, LCEs are photo-activated to alter the internal molecular structures between *trans* and *cis* form thus achieve two-way reversible actuation. The system developed by Lendlein needs extra programming before photo-irradiation and such deformation can be mostly fixed by the secondary crosslinks upon UV irradiation. In this dissertation, the LAPs are developed by Scott that require external loads. Photoinitiator recharge is necessary if multiple activation is needed.

(a)   (b)
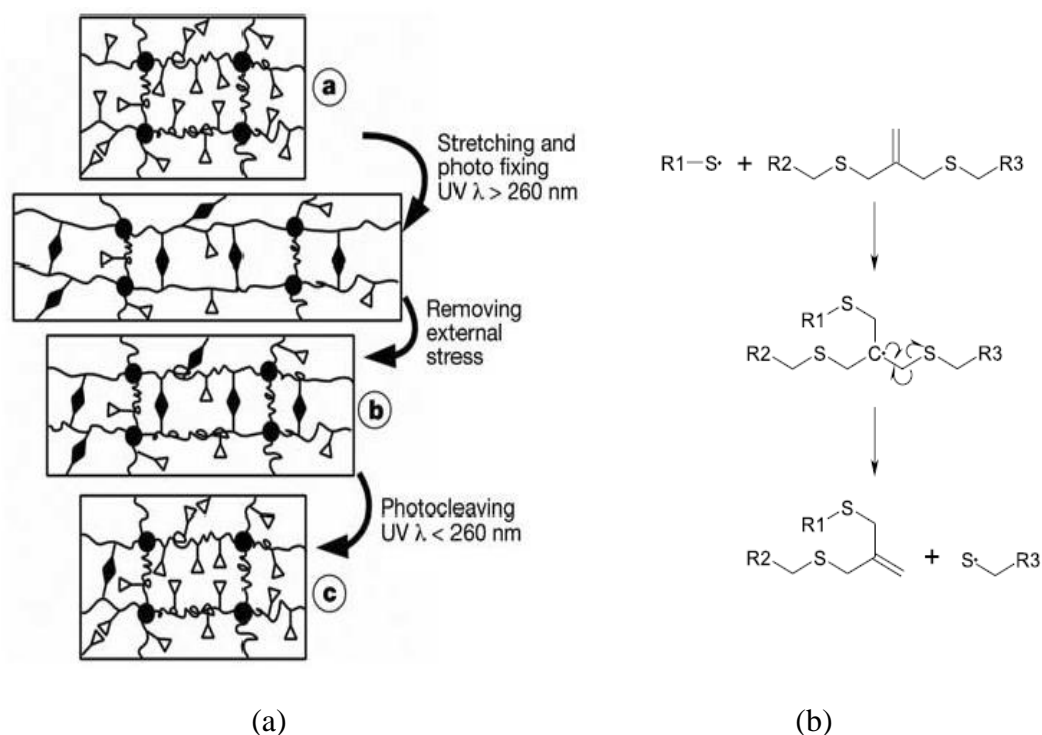
Figure 1. Two LAPs systems based on chain reactions.[29, 48]

1.1.3   Shape Memory Polymers

Shape memory polymers (SMPs) have the capability of remembering their shape after programming and recovering to its original shape upon certain stimulus. The most popular mechanism is thermal triggered shape change or thermal induced shape memory effect (SME). The polymers response to heat is referred as SMPs in this dissertation to distinguish with other active polymers such as LAPs. In general, two polymer chain systems including chemical and physical can be utilized to achieve SME triggered by heat.

(a)   (b)
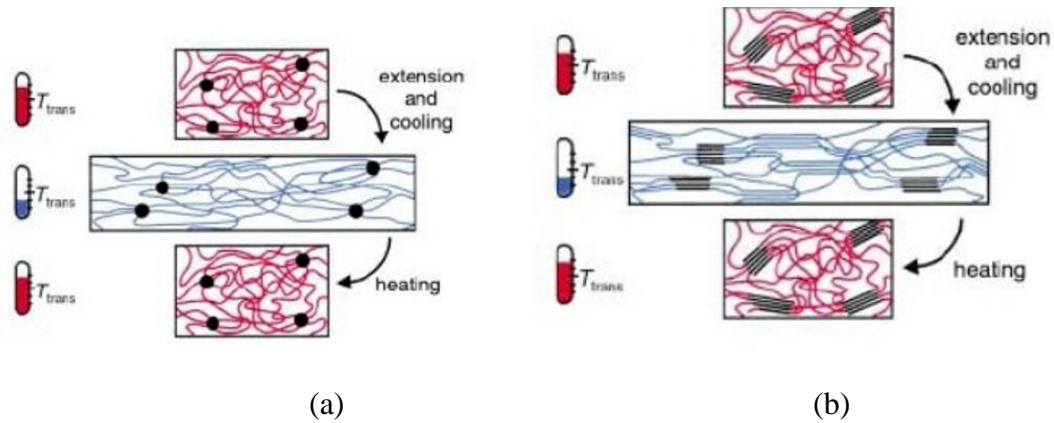
Figure 2. Two common mechanisms to achieve SME in SMPs.[1]

For chemical crosslinked covalent bond SMPs, external heat drives the so-called glass transition in amorphous polymer network from stiff glassy state to soft rubbery state due to the significantly changed chain mobility as shown in Figure 2(a). Two steps are commonly evolved in one SME cycle that are programming and free recovery. During programming, a load is first applied to SMPs in the rubbery state at temperature higher than glass transition temperature T_g. This load deforms SMPs into a temporary shape that can be fixed by cooling the temperature down while maintaining the shape. Mechanically, the applied stress is relaxed during the cooling process until reaching a deformed free-

standing SMPs. The free recovery step is simple to operate by elevating the temperature back to above T_g. On the other hand, physical crosslink is obtained in a semicrystalline polymer system where two domains, stiff crystalline domain and soft amorphous domain, are coexisting with a temperature-driven volume change with respect to each other as shown in Figure 2(b). The shape memory cycle for a semicrystalline polymer is similar to amorphous SMPs described above. As for the mechanism, the amorphous region in the network starts to crystallize as the temperature drops to below the crystalline temperature T_c. The elastic energy stored in the newly generated crystalline domain is frozen thus the external load is also relaxed under a constant strain. During the heating recovery step, the crystalline regions begin to melt when the temperature is above the melting temperature T_m, and the frozen elastic energy is restored. When a constant load is applied, SMPs with the ability given by chemical crosslink can only be activated and response once and it is named as one-way SMP. However, the physical crosslink crystalline driven SMP can be deformed and recovered multiple cycles and it is referred as two-way SMP.

1.1.4 Additive Manufacturing

Additive manufacturing (AM) or 3D printing (3DP) is a fast growing technology where a 3D object is created by laying down successive layers of material.[49-52] This revolutionary technology is believed to change product development and manufacturing industry. It is expected to be the next industrial revolution. Compared to the conventional manufacturing techniques, 3D printing has the advantages such as design freedom, less waste, rapid prototype, customization, *etc*. The generic AM process includes Computer Aided Design (CAD) model, conversion to STL file, upload to AM machine, machine setup, actual 3D printing, model removal, postprocessing and application. Based on the

materials and different requirements of the final product, various 3D printing methods have been developed. The most widely used polymer based AM methods are stereolithography (SLA), fused deposition modelling (FDM) and selective laser sintering (SLS). Other methods include powder bed jetting, material jetting, sheet lamination, direct ink write (DIW), *etc.* A schematic representation of a SLA 3D printer is shown in Figure 3. In the SLA approach, the z direction or depth resolution is determined by the photoinitiator and the irradiation conditions such as wavelength, laser power and exposure time. In addition, photoabsorbers such as dyes, pigments are used to control the xy plane resolution as well as z resolution. In a SLA printer, a tray is moving in the vertical direction inside a photopolymer reservoir. A laser or DLP projector, as shown in Figure 3(a), irradiates light onto the photocurable resin and solidifies a layer. Then the tray moves up or down depends on whether it is a bottom-up (the projector or laser is placed underneath the photopolymer resin and cures the resin though a transparent bottom substrate such like PDMS or Teflon) or top-down (light source is placed over the resin) 3D printing method. Recently, a DLP printer uses a technology called continuous liquid interface production (CLIP) that can speed up the printing process by two order of magnitude.[53] This bottom-up printer has a well-controlled called dead zone that prevents the cured new layer from attaching the substrate due to oxygen inhibition. This feature is attributed to the oxygen permeable substrate, an amorphous thin Teflon film with high chemical resistance and gas transport potential, very low refractive index and excellent optical clarity that extends into the UV range.[54] Since the cured layer has no physical contact with the substrate, the printed part can be pulled up directly and continuously without additional processing steps such like

6

peeling, sliding or separating. This feature greatly speeds up the whole printing process and the DLP projects a movie-like 3D slicing.
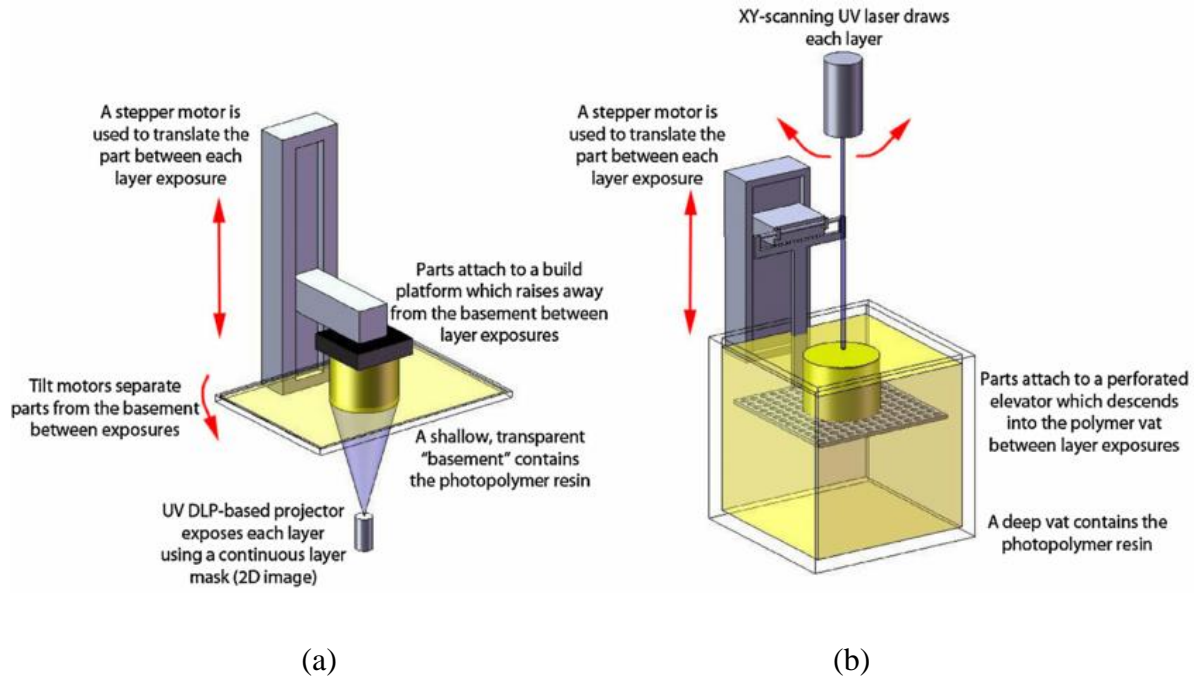
Figure 3. Two 3D printing methods that use photopolymerization in a bath of resin: (a) DLP and (b) SLA.[55]

A material jetting or polyjet 3D printer, as shown in Figure 4, consists of a print block and a build tray. The print block is assembled with multiple print heads that can inkjet numerous photocurable resin droplets as a pattern of the cross-section of the object. A roller is used to level the newly deposited layer and remove the excessive materials before photopolymerization. The UV lamp is moving together with the print block so that the pattern of the resin is subsequently cured by light. Using this printer, researchers have done many interesting applications such as 3D printed actuators and 4D printing where the shape of the printed parts may deform into other configurations triggered by heat.[49, 56] Photopolymers can also be used in other 3DP methods such as direct ink write (DIW). In

this dissertation, a new 3DP method is developed to 3DP porous materials that can have multi-functionalities as described in the following sections.
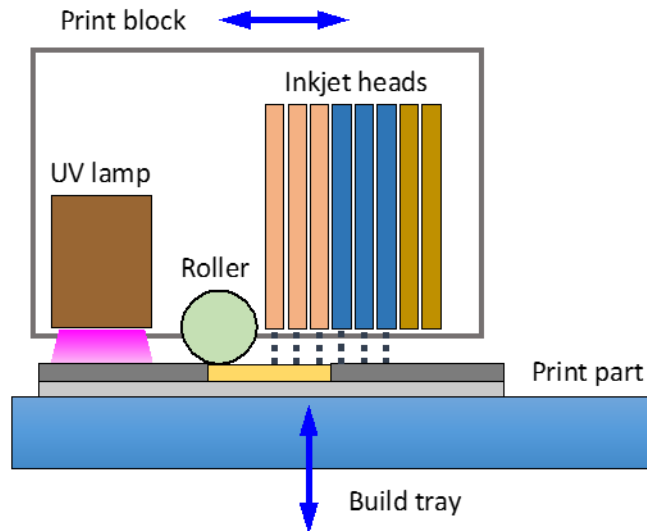
Figure 4. Schematic and printing process of a polyjet 3D printer.

1.2   Research Motivation and Goals

Although there are increasing attentions and researches on active polymers such as LAPs and SMPs, the applications of these active materials and their implementation into polymeric composite still require further investigation. For example, the BERs induced LAPs have been studied in areas including surface patterns, flaw retardation, origami and light-reforming.[32, 57-59] The 2D or 3D structures created by using this kind of LAPs are not suitable for self-actuation without assisted loading step. A method that can utilize BERs to initiate stress relaxation and create 3D structures out of 2D plane in a free-standing state is missing and necessary to be developed. For some applications, the polymeric material with a good initial flexibility is required to be deformed into a desired shape easily and then gets strengthened to hold the functional shape. Such requirement can be met by using two-stage

polymers that have two distinct sets of properties. Although some researches have been done in the past,[60-64] a photomechanical constitutive model is required to investigate the observed material property change. As for the additive manufacturing, polymers are still the most widely used 3DP material including thermoplastic polymers for FDM method and photocurable thermoset polymers for methods like SLA and material jetting. However, these methods are designed to create pure solid structures and treat pores as defects. Here we explore the functionality of porous structures fabricated by a combination of 3DP and salt leaching.

1.3   Thesis plan

This dissertation research is arranged as the following: the design of light activated polymeric composite and the theoretical modelling of photoinduced bending is investigated in Chapter 2. Photo-thermomechanical modelling and experimental results of two-stage reactive polymers are presented in Chapter 3. Chapter 4 introduces 3D printed porous materials by using photocurable resin. An overall conclusion is made in Chapter 5.

CHAPTER 2.   PHOTOINDUCED BENDING OF LIGHT-ACTIVATED POLYMERIC COMPOSITE

Light as an instant, remote, localized and precisely controllable stimulus, has been used to trigger a class of polymers that have unique properties or behaviors, namely light activated polymers. These smart photo-responsive polymers have attracted increasing attention since the magic source light can be relatively easily manipulated to perform non-contact control of the material shape and behavior through simple variation in light intensity, wavelength and exposed patterns. These specifications significantly distinguish LAPs from other active polymers triggered by other stimuli such as heat, electrical or magnetic field, and humidity. Previous examples have shown many interesting application and demonstrations such as surface patterning, photo-induced shape memory behavior, and photo-origami. Despite the interesting applications with various mechanics, some systems of LAPs have an undesirable limitation. Along with the progress of LAPs,[59, 65-67] the drawback is that the material has to be maintained in a stressed state to initiate stress relaxation thus create pattern change or shape deformation. Such drawback can also be discovered in the photoreversible material developed by Lendlein *et al*.[47, 48] Apparently, this necessity of external constant load is a hinder to achieve applications in a free-standing state such as photo-origami.[34] In this chapter, a laminated structure is designed to bear a pre-programmed stress field, and can be later on partially released to generate photo-induced deformation. The laminate is a three-layer structure consists of one stretched elastomer layer sandwiched by two LAP layers. The contraction of the middle elastomer layer causing the two LAP layers to be compressed even though the laminate itself is at a

static state as a result of internal force balance. The compressive stress in the LAP layers can be optically triggered and released, forcing the entire laminate to bend towards to the light source direction. A theoretical model is developed to quantitively describe and examine the laminated structure, serving as a tool for the exploration of the design space and optimum the laminate parameters.

2.1　Introduction

The smart materials studied in this chapter refer to a class of active polymers that respond to external stimuli such as heat, electric or magnetic field, humidity and light, *etc*. The exploration and research of smart materials have drawn great attention over decades. Light stands out among other stimuli as it provides special and unique advantages, such as spatially controlled activation, remote control, controllable exposed pattern using photo-mask, and the ease of stop, pause and resume. Various molecular mechanisms have been developed and improved based on photo-activation by other researchers in the past. Liquid crystal elastomers are the most well-known candidate, which contains ordered rod-like structures compromised of *trans*-azobenzene moieties.[39-45] This *trans* state is switchable under certain wavelength of light and transfers to the bent *cis* state under such circumstances. Upon the generation of the bent *cis* form in the azobenzene-doped LCEs, the polymer network changes from the ordered nematic phase to the disordered isotropic phase isothermally. This phase transition between *trans* and *cis* isomers are controlled by irradiation with distinct wavelength of light, which leads to macroscopic contraction or expansion in the LCE films.[46] Besides using LCEs as the light activated polymers, other polymeric system and molecular mechanism have been explored as well to achieve light actuation. Lendlein et al. developed a crosslinked polymer network that has photo-tunable

molecular crosslinks that can provide additional secondary crosslink upon irradiation of light at the wavelength longer than 260 nm and be cleaved under light with wavelength shorter than 260 nm.[29] The formation of the extra crosslinks and their cleavage are both two-way and recyclable, and can facilitate a reversible shape memory effect when a temporary deformed configuration is fixed by longer wavelength UV irradiation and a permanent shape is recovered by shorter wavelength UV exposion.[7] An amorphous crosslinked polymeric system developed by Bowman and his coworkers have covalently adaptive networks that can be photo activated.[47, 48] The light irradiation can cleave the embedded photoinitiators into free radicals that initiate bond exchange reactions, where a polymer chain with a free radical at one end forms an initial tertiary radical structure with the neighboring chain, followed by fragmentation of an adjacent bond to transfer the radical to a new free chain. The new free chain with the gained radical can continue this BERs that keep alternating bond formation and breaking process. This step rearranges the polymer backbone until radical termination occurs, where two radicals recombine and annihilate each other. Such BERs events permanently alter the polymer network structure and thus restore the polymer network to its highest entropy configuration When coupled with mechanical loadings, this network rearrangement can relax the pre-programmed stresses stored in the polymer network and achieve shape morphing through stress relaxation. The previous studies have shown potential applications using BERs in polymers, namely LAPs, including flaw retardation, surface patterns and light-reforming [32, 57-59]. Furthermore, constitutive models have been developed to describe BERs for such covalently adaptable polymer networks [59, 65-67]. The main argument for this chapter is the drawback of such polymer systems: the material has to be maintained in a stressed state during light

irradiation to trigger actuation. This necessity is usually fulfilled with application of an external load during irradiation. Obviously, this requirement imposes some limitations in practical implementation of these materials in applications such as photo-origami.[34]

Origami is an art of folding paper that has a long history in Asian countries especially in China and Japan. This traditional handicraft crease a flat sheet of paper into a 3D structure through steps of folding and shaping [68-70]. As a sequential folding art, origami inspires scientists in many fields such as mathematics, physics and materials, *etc*. Motivated by origami, material engineering researchers use smart materials as "paper" and stimulus as "hands" to generate 3D structures for potential engineering applications, such as airbag packaging, aerospace antenna deployment, photovoltaic, and biomedical devices.[69, 71-76] Shape memory polymers have recently been introduced as a platform for origami on the basis of their unique shape memory effect.[35, 77-79] The photo activation in photo-origami becomes more attractive for its non-contact, spatially resolved potential. However, the drawback that requires mechanical load during light exposure clearly compromises the advantage of remote actuation of photo-origami. Here in this chapter, we introduce a solution to overcome this hurdle by applying and storing some elastic energy into LAPs before activation by laminating a three-layer structure with built-in stress field and releasing the stress asymmetrically to curl the laminate. Under this circumstance, the external load is no longer necessary and is replaced by the stress field programmed through fabrication. As a result, the self-folding goal is achieved solely by light and is one step closer approaching the real photo-origami.

This chapter demonstrates the feasibility of applying such a laminate design for light-activated bending, which could then be used as a hinge for future origami designs.

We further developed a theoretical model and conducted a parametric study to explore the design space for optimizing the bending deformation. The majority of the work presented in this chapter has been published in *Soft Matter* in 2015.[80] Chapter 1 is organized as follows. Section 2.2 introduces materials and experiments, while photochemistry and the photomechanical constitutive model are presented in Section 2.3. Both simulation and experimental results are compared in Section 2.4. With the theoretical model, a parametric study is also presented in the same section to explore the design space and maximize the bending curvature. Section 2.5 presents supplemental materials and Section 2.6 concludes the work.

2.2   Materials and experiments

2.2.1   *Materials and Polymer Preparation*

The laminated composite consists of two LAP layers and one elastomeric layer. LAPs are synthesized by using three kinds of monomers, two kinds of photoinitiators, and additional photoabsorber as needed. Pentaerythritol tetra(3–mercaptopropionate) (PETMP) is a tetra-functional thiol monomer and is used as a crosslinker in this formula. Ethylene glycol di(3–mercaptopropionate) (EGDMP) is a di-thiol and the purpose of adding it to the system is to improve the flexibility and stretchability of the final sample. Both PETMP and EGDMP were donated by Bruno Bock Thiochemicals. 2-methylene-propane-1,3-di (thioethylvinylether) (MDTVE) was synthesized from 2-chloroethyl vinyl ether and 3–mercapto–2–(mercaptomethyl)–1–propene.[81] Two photoiniatiators Irgacure 184 (1–Hydroxy–cyclohexyl–phenyl–ketone—HCPK) and Irgacure 819 (Bis(2,4,6–trimethylbenzoyl)–phenylphosphineoxide—BPO), as well as the UV light absorber

Tinuvin 5060 were purchased from BASF. All the chemicals were used upon receipt without further treatment. LAPs were synthesized in a manner similar to previous work done by Bowman and his coworkers.[47, 48] A spot UV curing lamp (OmniCure S2000, Lumen Dynamics, Ontario, Canada) equipped with bandpass filters was used for all light irradiations. Light intensities were monitored by a radiometer (IL1400A, International Light Technologies, Peabody, MA).

The CANs were prepared by mixing the two photoinitiators Irgacure 184 (1.0 wt%) and Irgacure 819 (1.0 wt%) with a mixture of PETMP, MDTVE and EGDMP in a weight ratio 1:5:4. The formulation has no photoabsorber in it and is named as "optically thin" meaning that the light intensity is approximately uniform through the thickness.[82] The final mixture was stirred for 5 min at 45 °C to achieve homogeneity and sandwiched between two glass slides coated with Rain-X (SOPUS Products, Houston, TX). This Rain-X chemical is a commercial product used for glass surface treatment on automotive and houses for its function to convert the glass surface from hydrophilic to hydrophobic. Here we used it for every glass mold in polymer preparation so that the final cured thin film can be easily peeled off without damage. The polymer thickness is controlled by the dimensions of the spacers separating the two glass slides, for example, here we use two 0.13 mm thick polyester shims at the two ends. The sandwiched uncured resin was irradiated by light of 400-500 nm wavelength at 40 mWcm^{-2}, which photocleaves Irgacure 819 into radicals and initiates the polymerization via a radical-mediated thiol-ene reaction. Irgacure 184 is most reactive when exposed to UV light. Thus, the first irradiation of visible light in the photopolymerization step does not consume too much Irgacure 184 which was survived and can response to UV light at the activation step. The other "optically thick"

network was fabricated using the same formula and procedure with an additional 3 wt% Tinuvin 5060, a UV photoabsorber, before polymerization. This second network formula was designed to work as a thin adhesion for laminating the three layers as will be introduced in the following section. Since the photoabsorber may greatly attenuate the light intensity, another function of this "optically thick" adhesion is to confine the irradiated regions in case of the situation that the light penetrating through the entire three layers which is not in favor.

A commercially available photo adhesive, NOA65 (Norland Products Incorporated Company, Cranbury, NJ), was used as the intermediate layer in the laminated composite. NOA65 is a photopolymer that gels by UV light at 350-380 nm wavelength range. Its T_g is below room temperature so it is at its rubbery state at ambient temperature, thus fucntions as an elastomer in use. We injected the uncured liquid resin into glass slides with 0.17 mm spacing shims and cured it under 365 nm UV light at 20 mWcm^{-2} for 10 min. Glass slides were flipped over during the photopolymerization to ensure the resin was fully cured.

2.2.2   Mechanical and Photomechanical Characterization

The optically thin LAP film was cut into strips (15 mm (L) ×4 mm (W) ×0.13 mm (T)) for photomechanical testing and laminate fabrication. Stress relaxation tests were conducted using a dynamic mechanical analyzer (DMA Q800, TA Instruments, New Castle, DE). The LAP strip was mounted between film tension clamps with a static preload force of 0.001 N for straightness. The specimen was stretched to 10% strain at a strain rate of 5%/min. After being held in that strained state for 2 min, the sample was irradiated by a 365 nm UV light for 15 min and the holding force was measured during this time. Light

intensity used for this photomechanical stress relaxation test was varied to 5 mWcm^{-2}, 10 mWcm^{-2}, 20 mWcm^{-2} and 40 mWcm^{-2}.

2.2.3 *Laminate Fabrication*

The fabrication procedure of the laminated composite is schematically shown in Figure 5. The elastomeric middle layer, NOA65 strip, was firstly stretched by uniaxial fixer and maintained at this deformed state during the next adhesion step. Two fully cured optically thin LAP strips with the same width as the stretched NOA65 strip, however shorter in length, were glued to the stretched intermediate layer by using the optically thick LAP solution as adhesive and gelled upon irradiation with 400-500 nm light at 40 mWcm^{-2}. The same adhesion step was repeated once more time on the other side of the laminated composite. After taking the laminated structure out of the fixer, it shrank due to the release and contraction of the middle, elastomeric NOA65 layer. The gripped two ends were carefully cut off, yielding a laminated composite consisting of three layers with each layer sharing the same length and width. Failure to achieve the uniform dimensions leads to a curling configuration before activation. A well-fabricated laminate is flat with the central, elastomeric layer under tension and the outer LAP layers in a state of compression. The laminated composite can be stored in dark environment for weeks before irradiation by light. In this chapter, the UV light is mainly applied from one side with an expectation of actuation as light relaxes the compressive stress of the layer facing the light source. Photos of the experimental setup and procedure can be found in supplemental information section.
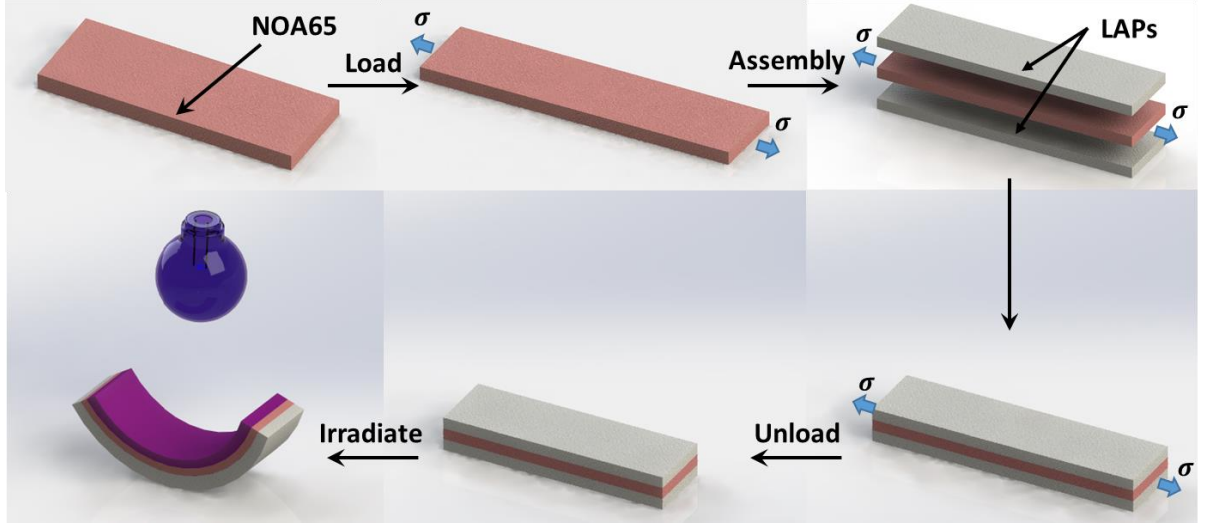
Figure 5. Fabrication and activation process of a laminated structure.

2.3   Modeling of Photomechanics and Actuation

Here in this section, we introduce a theoretical model to predict the nature and magnitude of light-induced laminate bending curvature. As light travels through the top LAP layer of the laminated composite, photons start to react with the embedded photoinitiators, generating free radicals that subsequently initiate BERs, leading to macroscopic relaxation of the compressive stress pre-applied by the contraction of the elastomeric central layer to which it is bonded. Since the LAP layers are on the outer layer of the laminate, this mismatch of the stress relaxation among each layer causes the laminate to bend towards to the light source direction. Therefore, the laminate bending curvature is controlled by light propagation, radical generation, BER rate, laminate dimensions, mechanical properties of each layer in the laminate, and the stress field in each layer as programmed. In order to study the complicated interrelationship among these factors and parameters, we start with the physics of light propagation and then describe briefly a photomechanical model for LAPs using phase evolution theory, which is eventually

substituted into the laminated structure, incorporating the geometric attributes and the mechanical properties, to predict the bending curvature of the laminated composite.

2.3.1 *Light Propagation*

To capture the physics of light and describe the constitutive behavior of the LAPs, we follow the previous work where the system modeled is composed of LAPs network, photoinitiators, radicals and photoabsorbers.[82] As mentioned, phase evolution theory is used to describe stress relaxation caused by BERs.[65] Since we are interested in the laminated structure described above with the same width for each layer, the system can be simplified as a two-dimensional (2D) problem, depth and length. Therefore, all the equations will be written in their 2D form. Here, we assume that light path direction is the z-direction which is also the thickness direction, and is measured with *z*=0 at the light entering surface. Light propagation through a continuous media is described by the Beer-Lambert law,

$$\frac{\mathrm{d}I(z,t)}{dz} = -A(z,t)I(z,t), \tag{1}$$

where $I(z,t)$ is the light intensity and is a function of spatial coordinate and time; $A(z,t)$ is the extinction field that describes the variation of light intensity due to absorption. The extinction field is expressed as,

$$A(z,t) = \alpha_I C_I(z,t) + A_{matrix}, \tag{2}$$

where α_I is the absorptivity of photoinitiators; $C_I(z,t)$ is the concentration of photoinitiators; A_{matrix} is the absorption from other species in the polymer system, such as Tinuvin 5060. Since we are only concerned with the optically thin layer, A_{matrix} is set to zero. Based on Fresnel's equations, Snell's law and the Beer-Lambert law, the light intensity field in a curled shape optically thin LAP sample was computed using MATLAB and the results are shown in the supporting information in Section 2.5. To simplify this simulation, we neglect the possibility that the light can be reflected inside of the polymer media and continue irradiating other internal areas in the laminate. Moreover, the final curled shape with initial concentrations of photoinitiators is studied (instead of the initial flat configuration with decaying photoinitiator concentration) so that the curled configuration of the laminate can also be incorporated into the light intensity calculation. As the results show in Figure 14, the lowest light intensity for this extreme scenario is located at the two ends and is still 82% of the incident light. The majority part of the LAP thin film has little light intensity decay compared to its initial value. Thus, we assume hereafter that light intensity is uniform in the LAPs during irradiation and is not affected by the bending deformation of the laminate. For larger bending angles, a nonlinear approach where the incident angle varies and the reflection and deflection of light due to the surface should be taken into consideration.

2.3.2 *Photochemistry*

During UV irradiation, light propagates through LAPs and induces photochemical reactions on photoinitiator molecules, generating free radicals, cleaving and reforming polymer backbone through BERs. The photoinitiator consumption and free radical generation are governed by,

$$\frac{\partial C_I(z,t)}{\partial t} = -\beta C_I(z,t)I(z,t) + D_I \nabla^2 C_I(z,t), \tag{3}$$

$$\frac{\partial C_R(z,t)}{\partial t} = m\beta C_I(t)I(z,t) - k_{term}C_R(z,t), \tag{4}$$

where $C_R(z,t)$ is the concentration of free radicals; β is a lumped constant parameter representing absorption and quantum efficiency; m is the number of free radicals created from each photoinitiator reaction and is precisely 2 in this study. The second term on the right hand side (RHS) of Eq. 3 describes the diffusion of photoinitiator with D_I as diffusivity. The second term on the RHS of Eq. 4 describes the termination of free radicals where prefactor k_{term} is a fitting parameter and the exponent n defines the number of radical molecules for each termination reaction. Although bimolecular termination was expected, the value of n is estimated as unity experimentally.[48, 82] Since the free radicals diffuse much slower than photoinitiators, the diffusion of the free radicals is not considered here.

2.3.3   Photo-induced Stress Relaxation

Light irradiation initiates BERs that rearrange the polymer network and relax the internal stress. Here, we use the well-developed phase evolution rule to describe the network rearrangement and its mechanical consequences,[65]

$$\frac{\partial f_O(z,t)}{\partial t} = -k_1 C_R(z,t)f_O(z,t)^p, \tag{5}$$

21

$$f_O(z,t) + f_R(z,t) = 1 \tag{6}$$

where f_O and f_R are the volume fraction of the original network and reformed network, respectively; k_1 is a fitting parameter and the negative sign indicates the decrease of the original network fraction due to reformation; the power p is another fitting parameter that captures the dependency of the rate on the volume fraction of the original network. Mathematically, the rate is much higher at the beginning of the irradiation and slows down due to the consumption of the free radicals and the reformation of the original networks.

We assume that $t = 0$ is the time before which there is no irradiation and at which point irradiation begins. The stress in the LAPs is,

$$\sigma_0 = E_L \varepsilon_L^0, \tag{7}$$

where ε_L^0 is the initial strain introduced in the polymer network, and E_L is the modulus of the LAP. Here, the subscript L indicates reference to the LAP layers. In addition, we use the Hencky strain $\varepsilon = \ln\lambda$ as it conveniently converts the multiplication of stretches into additive strains and thus simplifies the numerical calculations.[83]

After $t = 0$, light irradiation starts and triggers BERs. The mechanical stress in the LAPs during light irradiation can be described generally as,[67, 84]

$$\sigma(z,t) = E_L\big(1 - f_R(z,t)\big)\big(\varepsilon_L^0 + \Delta\varepsilon(z,0,t)\big) + E_L \int_0^t \frac{\partial f_R(z,\tau)}{\partial \tau} \Delta\varepsilon(z,\tau,t)d\tau, \qquad (8)$$

where $\Delta\varepsilon(z,0,t)$ is the strain increment during light irradiation; $\Delta\varepsilon(z,\tau,t)$ is the strain increment measured from time τ to time t. The first term on the RHS is the stress in the original network while the second term is the stress in the reformed network. The modulus E_L stays the same for both networks since BERs do not form additional crosslinks but keep breaking and reforming them instead.

2.3.4   *Model for the Laminated Structure*

As illustrated in Figure 5, the intermediate layer is loaded to a pre-determined strain and is maintained at that strain while the two LAP layers are attached. After releasing the external load on the intermediate elastomeric layer, the laminate shrinks due to the contraction of the intermediate layer and compressive strain is thus introduced in the LAP layers. The thickness of the LAP layer is re-measured after the fabrication of laminated composite to take the thickness of each bonding layer into account. In this section, we develop a model to describe the photo-induced laminate bending.

2.3.4.1   Laminate Contraction

The first step is to calculate the compressive strain in the LAP layers introduced by unloading the intermediate layer. This can be obtained simply by using the equilibrium equation,

$$E_N(\varepsilon_0 + \varepsilon_N)h_N + 2E_L\varepsilon_L h_L = 0, \tag{9}$$

where E_N is the modulus of the intermediate NOA65 layer; ε_0 is the initial strain in the intermediate layer; h_N and h_L are the thicknesses of intermediate and the LAP layers, respectively; ε_N and ε_L are the strain increments in intermediate and LAP layers, respectively. Assuming no slip on the interfaces, the strain increments in each layer should be $\varepsilon_N = \varepsilon_L$. Note that it is the initial mechanical strain in the LAP layers, thus

$$\varepsilon_L^0 = \varepsilon_L = -\varepsilon_0/[1 + (2E_L h_L)/(E_N h_N)]. \tag{10}$$

The negative sign here indicates that the LAP layers are under compression. As expected, a larger initial tensile strain in the intermediate layer, ε_o, creates a larger compressive strain in the LAP layers. The final compressive strain in the LAP layers also depends on material properties and geometric parameters. Generally, a thicker and stiffer intermediate layer is able to introduce more compressive strain in the LAP layers. The initial strain in the intermediate layer can greatly affect the final bending curvature, as will be presented and discussed in the following sections.

2.3.4.2   Laminate Bending

The laminate is composed of three layers, whose cross-section dimensions are shown in Figure 6a, where x-y is in the plane of the surface of the top LAP layer that is irradiated and the z coordinate defines the thickness. The bending angle is defined as θ in Figure 6b with an initial value $0°$ when the laminate is flat. Based on Euler-Bernoulli beam

theory, taking the strain at $z=0$ as ε_0 ($\varepsilon(0) = \varepsilon_0$), strains along z axis due to bending are as follows,

$$\varepsilon_b(z,t) = \varepsilon_0(t) + \kappa(t)z, \tag{11}$$

where κ is the bending curvature of the beam. It should be noted that x-y plan is the reference plane and is not the neutral plane, and therefore ε_0 is not necessarily zero. Since the bending is caused by light irradiation, the bending strain is equal to the strain increment. Thus

$$\Delta\varepsilon(z,0,t) = \varepsilon_b(z,t) = \varepsilon_0(t) + \kappa(t)z, \tag{12}$$

$$\Delta\varepsilon(z,\tau,t) = \varepsilon_b(z,t) - \varepsilon_b(z,\tau) = \varepsilon_0(t) - \varepsilon_0(\tau) + [\kappa(t) - \kappa(\tau)]z. \tag{13}$$

The above two equations calculate the stress in the irradiated LAP layer by using Eq. 8. For the unirradiated LAP layer and the intermediate layer, the strains are

$$\varepsilon_U(z,t) = \varepsilon_L^0 + \Delta\varepsilon(z,0,t) = \varepsilon_L^0 + \varepsilon_0(t) + \kappa(t)z, \tag{14}$$

$$\varepsilon_N(z,t) = \varepsilon_0 + \varepsilon_L^0 + \Delta\varepsilon(z,0,t) = \varepsilon_0 + \varepsilon_L^0 + \varepsilon_0(t) + \kappa(t)z, \tag{15}$$

where the subscript U represents the unirradiated LAP layer and the subscript L in the following equations notes the irradiated LAP layer.
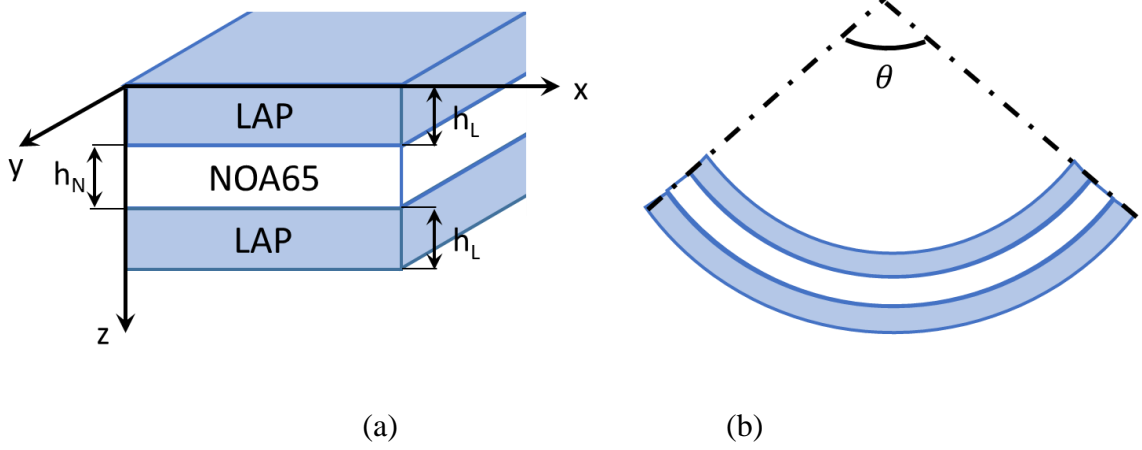
Figure 6. Geometry: (a) Cross-section, and (b) Bending angle θ of the laminate.

The stresses in the unirradiated LAP layer and the intermediate layer can be calculated as,

$$\sigma_U(z, t) = E_L \varepsilon_U(z, t), \tag{16}$$

$$\sigma_N(z, t) = E_N \varepsilon_N(z, t). \tag{17}$$

In the above equations, $\varepsilon_0(t)$ and $\kappa(t)$ are the only two unknowns and are solved by checking force and moment equilibrium along the beam cross-section. During irradiation, there are no external forces or moments acting on the laminate which is desirable. In order to meet force and moment equilibrium, we have,

$$F_{total} = F_U + F_N + F_I = 0, \tag{18}$$

$$M_{total} = M_U + M_N + M_I = 0, \tag{19}$$

where F_N, F_U and F_I are the forces acting on the cross-section of intermediate layer, unirradiated and irradiated layers, respectively. Substituting Eq. 8, Eq. 16 and Eq. 17 into the above equilibrium equations, we obtain,

$$\int_0^{h_L} \sigma_I(z)dz + \int_{h_L}^{h_L+h_N} \sigma_N(z)dz + \int_{h_L+h_N}^{2h_L+h_N} \sigma_U(z)dz = 0, \tag{20}$$

$$\int_0^{h_L} \sigma_I(z)zdz + \int_{h_L}^{h_L+h_N} \sigma_N(z)zdz + \int_{h_L+h_N}^{2h_L+h_N} \sigma_U(z)zdz = 0. \tag{21}$$

The above two equations are solved incrementally for $\varepsilon_0(t)$ and $\kappa(t)$. Once the curvature has been determined at each time-point, the bending angle can be simply solved for using the expression,

$$\theta(t) = \kappa(t)l \tag{22}$$

where l is the length of the irradiated region. l is set to be 1 mm to calculate the bending angle of a unity long laminated composite ($^\circ$ mm^{-1}) in the next section. This facilitates comparison with experiments for any value of l.

2.4 Results

The above theoretical model is implemented into a MATLAB program. Three fitting parameters are first determined based on the stress relaxation tests of the LAPs. Then the theoretical model is used to simulate laminate bending and compare with experimental results. Finally, a parametric study is conducted to explore the optimum bending curvature.

2.4.1 *Photo-induced Stress Relaxation and LAP Material Parameters*

Photo-induced stress relaxation tests were conducted by using the DMA apparatus at various light intensities: 5, 10, 20, and 40 mWcm^{-2} as described in Section 2.2. The normalized stress relaxation curve at 10 mWcm^{-2} was used to determine the three fitting parameters; namely, the radical termination rate k_{term}, the phase evolution prefactor k_1 and the power p. The rest of the parameters in the model for the LAP were obtained from the literature.[82] Having established all of the necessary parameters, the other three curves were predicted for comparison with experiment using the same parameter set, as shown in Figure 7. The fitting parameters are shown in Table 1 with other parameters and their references. These parameters were then used in the laminate bending simulations as will be shown in the following subsection.
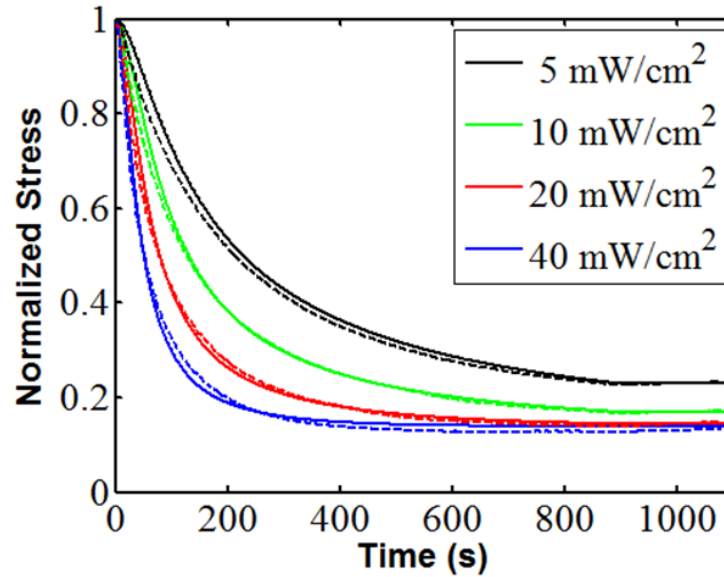
Figure 7. Phase evolution theory is used to predict photo-induced stress relaxation at various light intensity: solid lines are simulation results and dash lines are experimental results.

Figure 7 shows a good agreement between the model simulations and the experimental results. In general, a higher light intensity leads a faster stress relaxation rate and, overall, stress relaxation occurs slowly, on the order of minutes during illumination. We chose 10 mWcm^{-2} as the light intensity in the laminate bending experiment as it is large enough to relax most of the stress in the irradiated LAP layer.

Table 1. Parameters used in the theoretical model are listed along with reference from which the value was obtained ("Calculated" means that it is calculated from the information provided by the vendor).

Parameter	Value	Units	Description	Reference
α_I	118	L mol^{-1} cm^{-1}	Photoinitiator molar absorptivity	[82]
$C_I(0)$	0.047	mol L^{-1}	Initial photoinitiator concentration	Calculated
A_{matrix}	0	cm^{-1}	Photoabsorber coefficient	[82]
$C_R(0)$	0	mol L^{-1}	Initial radical concentration	Calculated
m	2	Dimensionless	Number of radicals per reaction	[82]
β	1.8e-5	s^{2}kg^{-1}	Photoinitiation coefficient	Calculated
k_{term}	0.03	s^{-1}	Radical termination prefactor	Fitted
n	1	Dimensionless	Radical termination exponent	[82]
k_1	2.0	Dimensionless	Phase evolution prefactor	Fitted
p	2.0	Dimensionless	Phase evolution exponent	Fitted
E_L	4.1	MPa	LAPs modulus	Measured
E_N	6.7	MPa	NOA65 modulus	Measured

2.4.2   *Experimental and Theoretical Results*

A 0.17 mm thick NOA65 strip with an initial length approximately 9.10 mm was stretched to 10.47 mm (15% strain) and held at that deformation during the adhesion step. After assembly, the laminated composite was released, contracting to a length of 9.73 mm and remaining flat, as expected due to the symmetric assembly. The thickness of the laminated composite was then measured as 0.51 mm, revealing a final thickness of the LAP layer (including bonding part) was 0.17 mm. The laminated composite was then irradiated on one side by 365 nm, 10 mWcm^{-2} light. Figure 8 shows the bending of the laminated composite during light irradiation. A digital camera was set up to take photos every 15 seconds during irradiation. Selected photos with a time interval of 2 minutes are presented in Figure 8 and the video can be found in the supporting information online. As the figure shows, the initially flat laminate exhibited noticeable bending curvature after 2 min irradiation. Curvatures and bending angle per unit length at different times were measured by ImageJ and are shown in Figure 9a and 9b. The bending curvature of the laminated composite gradually increased to 0.163 mm^{-1} at 10 min and then slowly approached 0.175 mm^{-1} by 15 min when the whole laminate bent 90°. In addition, due to the uniform irradiation on the top surface, the laminate shows an almost uniform bending curvature.
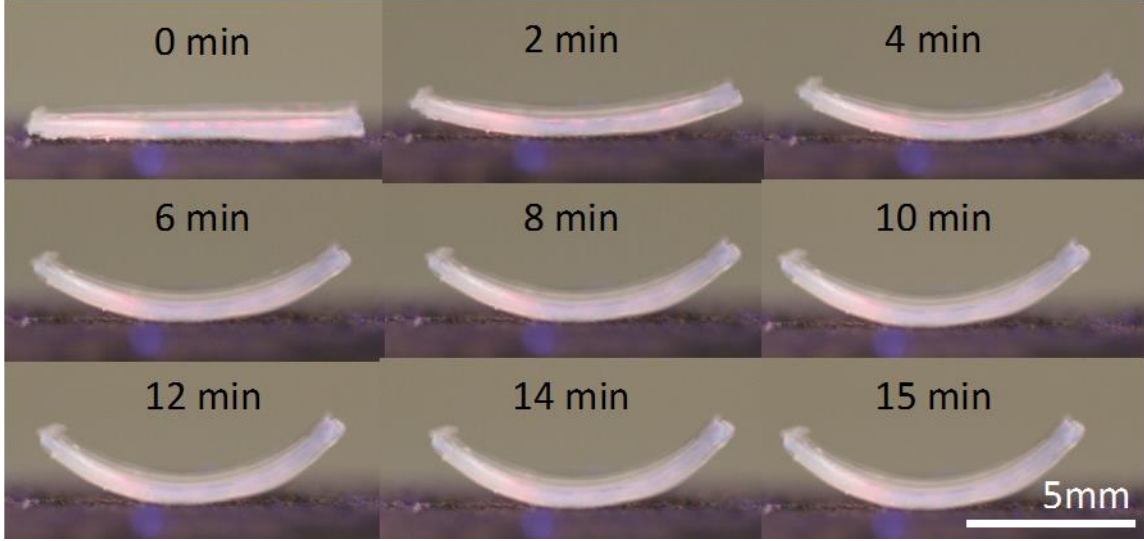
Figure 8. Laminate bending behavior upon 10 mWcm^{-2}, 15 minutes UV irradiation.

Figure 9a shows that the curvature has a nonlinear relationship with the irradiation time and approaches a plateau at the end of the irradiation, attributed to the nonlinear stress relaxation of the LAPs as shown in Figure 7. The bending angle in the current laminate asymptotes at $10^{o}\,mm^{-1}$, as shown in Figure 9b. We observed further that the theoretical predictions match well the experimental results.

Based on our experimental observations, the laminated composite design can be activated successfully in a free-standing state. However, the bending curvature at this point is not large enough to be used for the general design of photo-origami, where creases approaching those of paper-based origami are desired. Therefore, a parametric study examining the effects of the geometric and material properties is conducted to explore the design space that can be used in photo-origami.
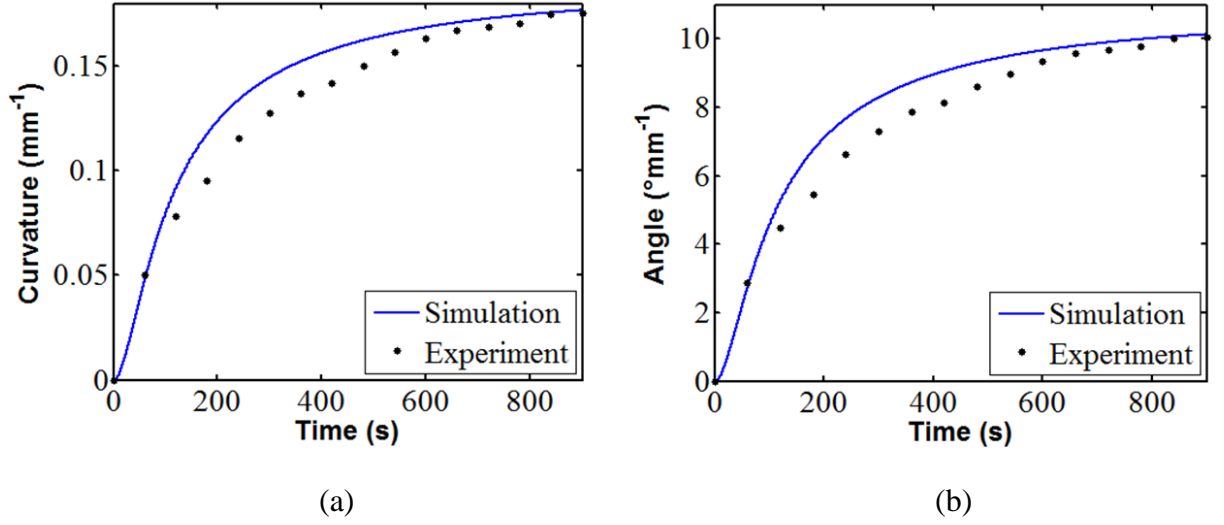
Figure 9. Results comparison for (a) bending curvature; (b) bending angle.

2.4.3 *Parametric Study and Demonstrations*

The theoretical model for laminate design provides a tool to explore the design space, which is prescribed by the laminate geometric parameters and the material properties. Based on the parametric study and the current laminated composite properties, the bending angle can indeed be improved.

To show the interrelationship between the laminate geometry, the material property and the bending angle in detail, we set the modulus ratio and the thickness ratio between the intermediate NOA65 layer and the LAP layer as *x*- and *y*- axes, respectively, while on the *z*- axis we plot the bending angle as shown in the 3D plots on the left of Figure 10. In the 2D plots, on the RHS of Figure 10, four curves with the specific thickness ratios (0.5, 1.0, 1.5, and 2.0) are compared to provide a better visual picture.

(a)

(b)

(c)
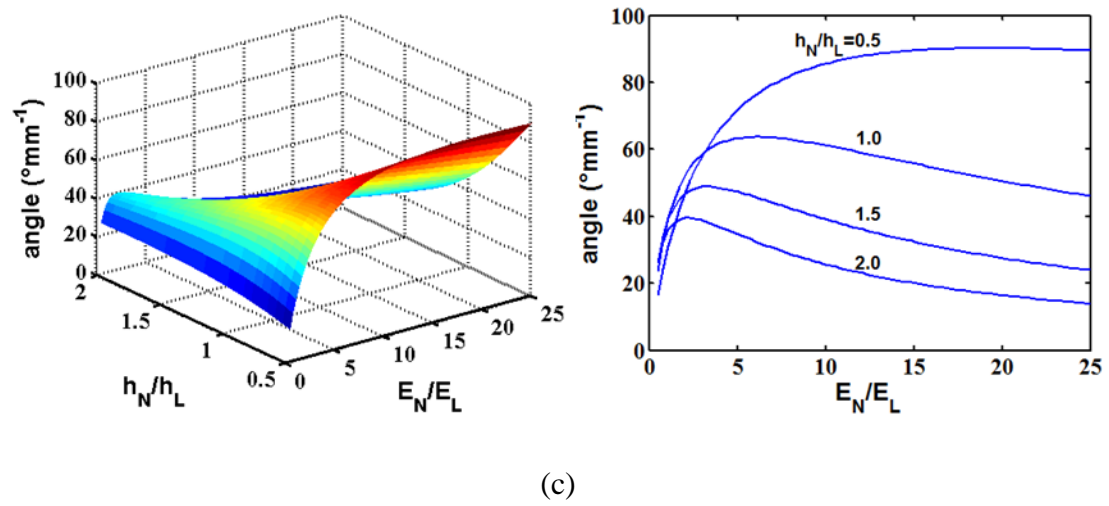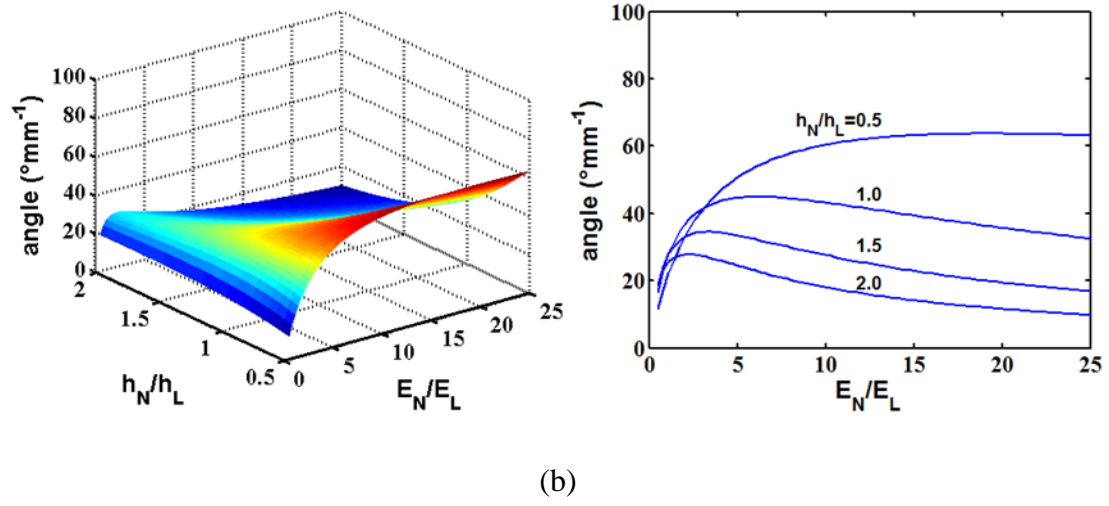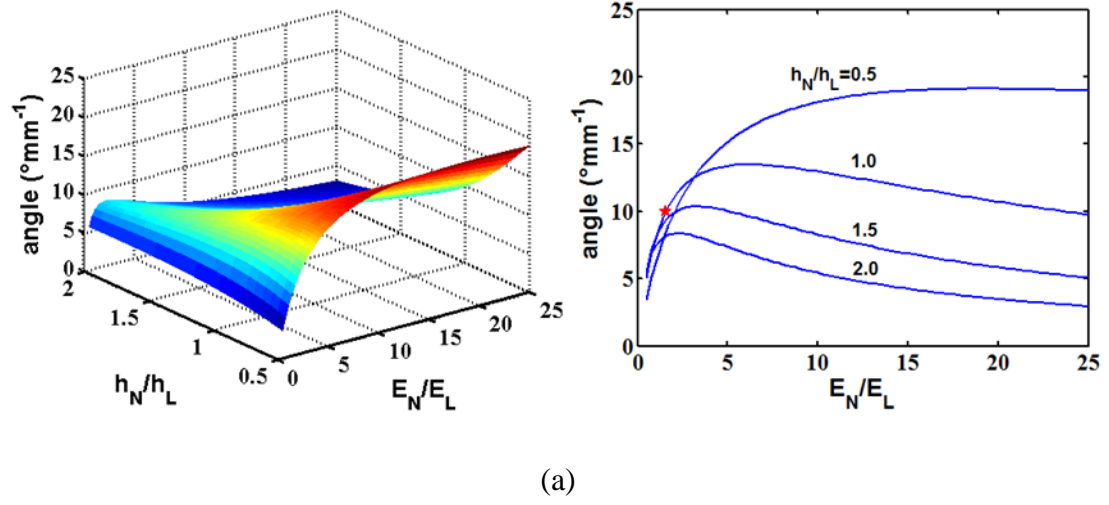
Figure 10. 3D and 2D plots showing the bending angle varying with thickness ratios and modulus ratios, using different initial strains in the intermediate NOA65 layer

and different thickness of the LAP layer: (a) $\varepsilon_0 = 15\%, h_L = 0.17$ mm. The red star shows the current design; (b) ε_0=50%, h_L=0.17 mm; (c) ε_0=50%, h_L=0.12 mm.

In Figure 10a, the thickness of the LAP layer is 0.17 mm and the initial strain in the intermediate layer is 15%. The current laminate bending experiment shown in Figure 8 used the same strain and thickness with the thickness ratio $E_N/E_L = 1.0$ and is shown as a reference point (star) on the 2D plot. It is interesting to note that there is a nonlinear relationship between the modulus of the intermediate layer and the bending angle. Increasing the intermediate layer elastic modulus initially increases the bending angle because that leads to increasing compression of the LAP layer more (for a given strain), in turn leading to more bending during light activation. However, since the intermediate layer also provides resistance to bending (even though it crosses the mid-plane for bending), too high of an elastic modulus for the intermediate layer will eventually reduce the bending angle. It is also important to note that the bending angle decays dramatically with the increase of the thickness ratio in the selected range because the thicker the intermediate layer is, the larger its cross-section area will be and the more resistant to bending it will become. In this case, for the thickness ratio above 2.0, the bending angle keeps decreasing until approaches to zero since LAPs play a negligible role, mechanically, when the thickness ratio is enormously large. However, for thickness ratios below 0.5 as shown in Figure 15, the bending angle decreases after reaching a critical value as a thinner intermediate layer provides a smaller compressive strain in the LAP layer and sacrifices the bending angle during irradiation.

The reason we chose this range of thickness ratios to study is for the sake of feasibility in the experiment. The lower bound of the thickness ratio 0.5 corresponds to a

thickness for the intermediate layer of only about 0.08 mm. In practice, an intermediate layer as thin as 0.1 mm is already very difficult to handle during the laminate fabrication due to the fragility. The upper bound of the thickness ratio 2.0 was chosen upon observing that it was already large enough to show an obvious decay effect of the thickness ratio. Compared with the geometric and material properties of the current laminate, we conclude that a stiff and thin intermediate layer is favorable. Noting that NOA65's elastic modulus is 6.7 MPa, there is room for improvement.

The initial strain in the intermediate layer has a major effect on the bending angle as shown in Figure 10b. With an initial strain 50% in the intermediate layer, it is able to create a bending angle as large as $65^{o}\,mm^{-1}$ in the laminated composite. This is because a larger initial strain in the intermediate layer helps compress the LAP layer, introducing a larger compressive stress by its contraction. Therefore, the stress relaxed in the irradiated LAP layer is predicted to increase, generating a larger stress mismatch thus creating a larger bending angle in the laminated composite.

Based on the theoretical model, the individual modulus of each layer does not affect the final bending angle results as long as the modulus ratio is fixed. However, unlike the modulus ratio, a fixed thickness ratio does not guarantee the same bending angle. If the thicknesses of individual layers change at the same scale that have the same thickness ratio as before, the bending angle will change correspondingly. As shown in Figure 10c, a slightly thinner (0.12mm) LAP layer can create a bending angle as large as $90^{o}\,mm^{-1}$, which can be utilized to fold a hinge in photo-origami. Therefore, a larger bending angle can also

be achieved by isotropically scaling down the size of the laminated composite, establishing our principle challenge to be one of manufacturing.

A laminate design has been demonstrated to be feasible for photo-bending without external loading and our parametric studies provide the theoretical foundation for enhancing the bending curvature. However, there are some challenges to achieve a large bending curvature. One is the limited adhesion between the intermediate layer and the LAP layer: delamination was found to occur for the cases with an initial strain larger than 15%. Indeed in earlier experiments, we used PDMS as the intermediate layer and achieved photo-induced bending in the laminate. However, the adhesion between PDMS and LAPs was so weak that the laminate usually delaminated after unloading; i.e., before photo-actuation could be attempted. NOA65 was selected as a better choice for the intermediate layer due to its thiol-ene reaction that provides a stronger adhesion. Moreover, attributed to its large modulus, NOA65 yielded a larger bending curvature than PDMS. Another potential challenge is the oxygen inhibition near the surface of a film.[85-87] This inhibitory effect of molecular oxygen inactivates radicals during photopolymerization and may also decay the rate of BERs, preventing LAPs from relaxing more stress, and diminishing the bending curvature of the laminated composite. To solve these problems, we are searching for other substitute elastomers as the intermediate layer and testing the oxygen effect on BERs in LAPs.[86]
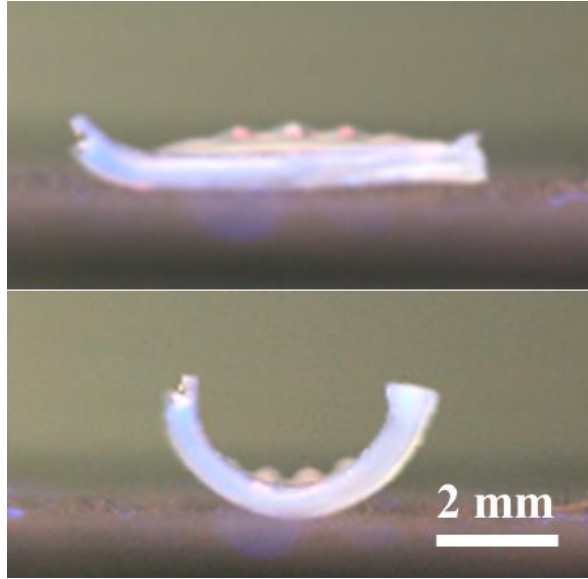
Figure 11. Photo-induced actuation of the laminated composite with the middle layer being stretched to 40%.

To test and demonstrate the parametric study and the developed strategies, a series of experiments were conducted using the same fabrication methods but various programming degrees. Figure 11 presents the straight forward method by applying a larger strain 40% to the middle layer during fabrication. It is very obvious that the bending curvature is significantly increased when the initial strain is increased from 15% to 40%. However, it is also important to note that the laminate fabrication may run into some issues under such large strain, for example, buckling after contraction as shown in Figure 11, and delamination.

Besides trying a larger initial strain in the intermediate NOA65 layer, the LAPs were also used as patches and attached on the middle layer as shown in Figure 12. In this case, the LAP patches act as potential hinges upon UV irradiation. Only the patched region has LAP thus greatly lighten the weight and increase the deformation. One thing need to note that the patched region still needs to be a tri-layer structure to ensure a flat sheet. The

37

patched LAP composite gives a final configuration as shown in Figure 12(b). However, the largest configuration for this design should always be the ones without the top LAP patches as shown in Figure 12(c). It means that the photo-induced stress relaxation cannot relax the entire compressive stress in the system.
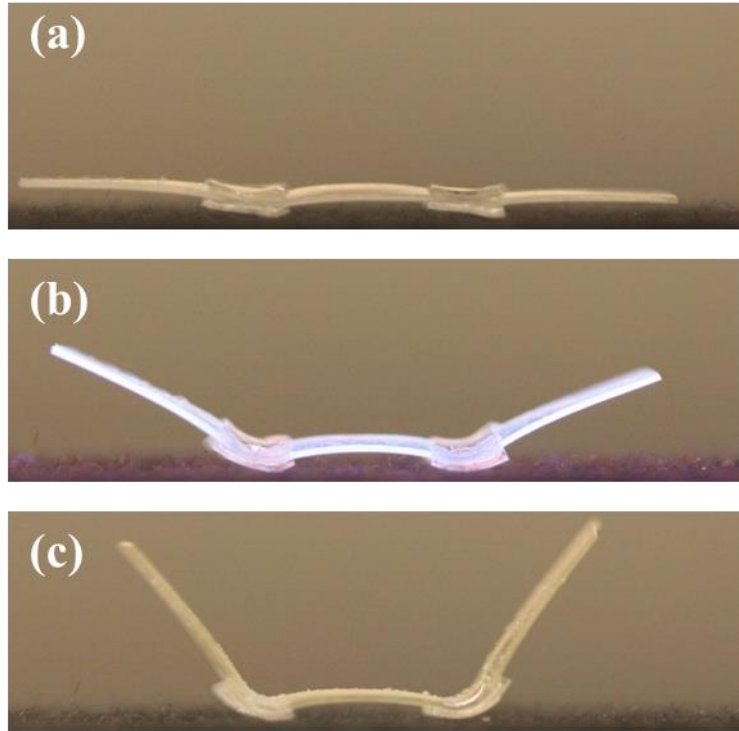
Figure 12. Photo-induced actuation of a patched composite: (a) initial state; (b) after UV irradiation; (c) after peeling off the top LAP patches.

2.5 Supplemental Materials
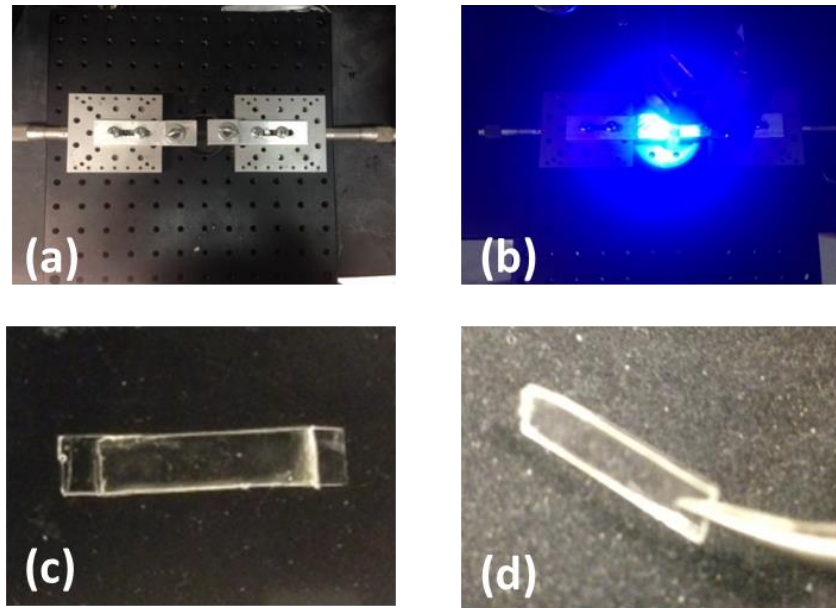
Figure 13. Photos showing procedures during fabrication: (a) intermediate layer was uniaxially stretched by the tensile clamps; (b) visible irradiation was used to photocure the glue resin (LAP solution) and bond the three layers together; (c) intermediate layer was unloaded; (d) two ends of the intermediate layer were cut off and a flat laminate composite was finally obtained.
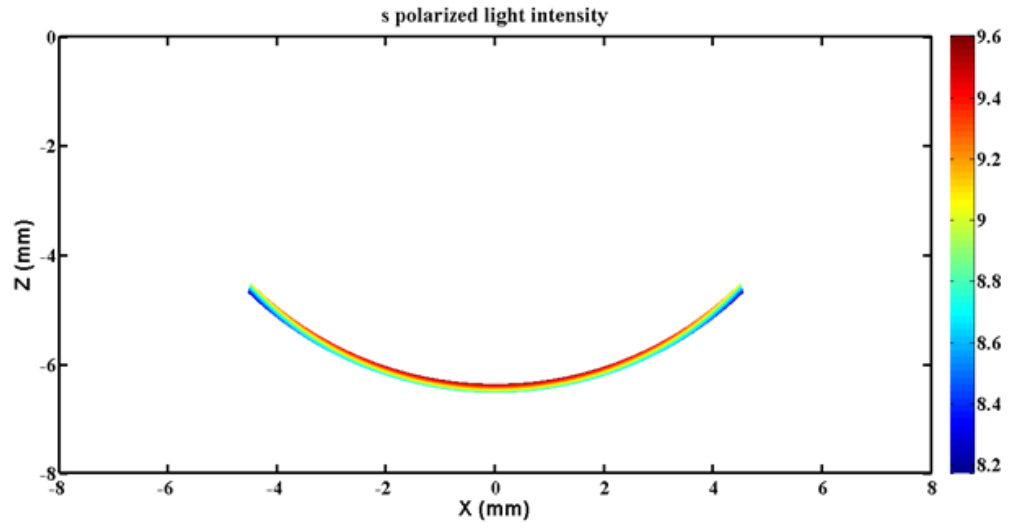
(a)
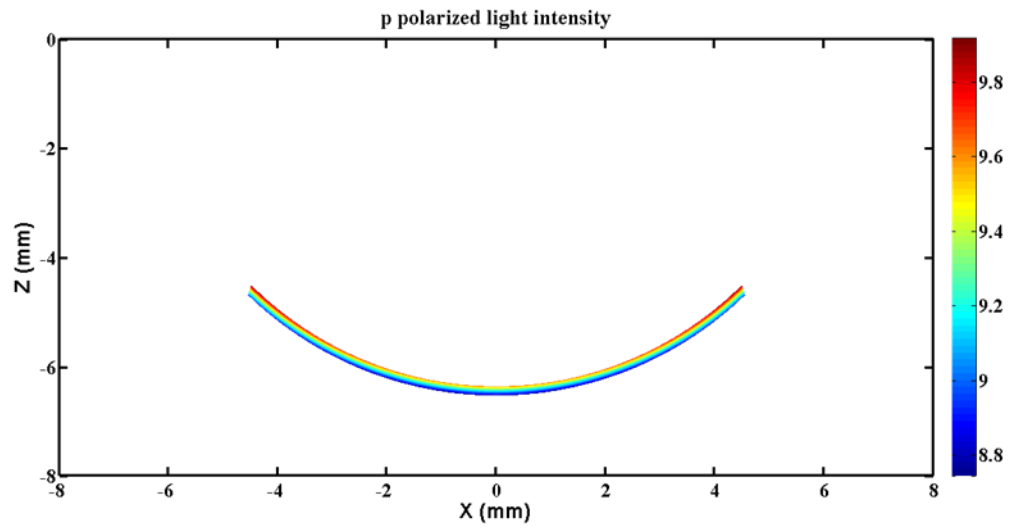
(b)

Figure 14. Light intensity fields: (a) s polarized light; (b) p polarized light of a 0.17 mm thick optically thin LAP layer at 10 mWcm⁻².

(a)   (b)
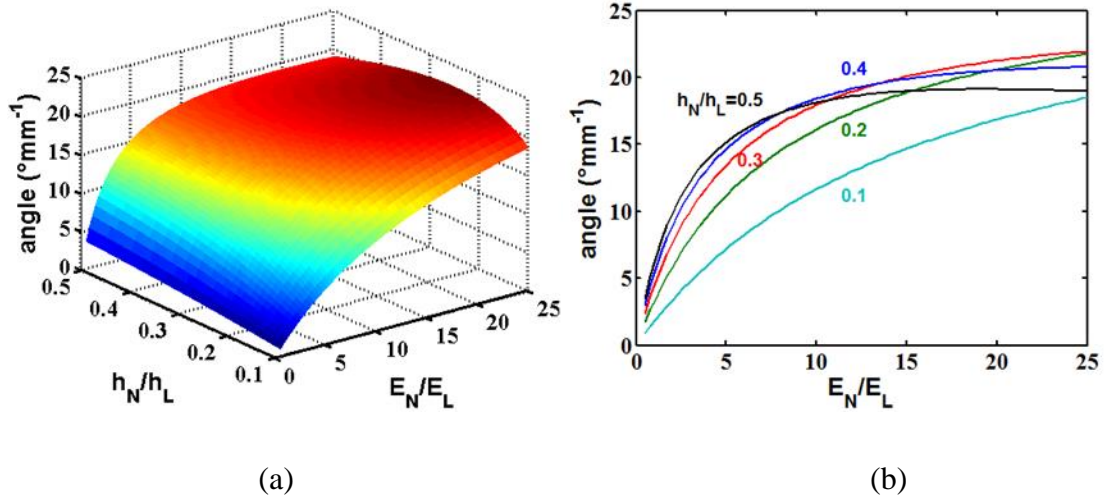
Figure 15. 3D and 2D plots for thickness ratio between 0.1 and 0.5. Other parameters are same as plots in Figure 6(a), ε_0=15%, h_L=0.17 mm.

2.6 Conclusions

A light-activated polymer laminated composite was designed to overcome the drawback of prior approaches that required mechanical loading during irradiation. A theoretical model was also developed to assist the design. Experimentally, we observed that illumination of one side of the laminate gradually curled the samples toward the light to a limiting value. The theoretical model developed was successful in predicting the features of the observed bending angle and fits the experimental observations well. A parametric study explored the laminate design space in geometric and material properties. The results of this study indicated that a thin intermediate layer with a large modulus compared to that of the LAP layer produces a large bending curvature. Other effective methods to gain a significantly enhanced bending curvature include increasing the initial strain in the intermediate layer, isotropic scaling down the size of the laminated composite. Some of the potential improvement methods have been demonstrated such as a larger initial strain in the intermediate layer and a patched LAP composite design.

CHAPTER 3.   PHOTO-VISCOELASTIC MODELING OF TWO-STAGE REACTIVE PHOLYMERS

3.1   Introduction

Two-stage reactive polymer system consists of two reactions creating distinct first and second stage polymers. The 1st stage is formed by the thiol-acrylate "click" Michael addition reaction within a mixture of multifunctional thiol and excess multifunctional acrylate, resulting in a dilute thiol-acrylate polymer network with excess unreacted acrylic functional groups. The 2nd stage is achieved by shining light to active the embedded photoinitiators and polymerizing the remaining acrylic moieties. The 1st stage polymer is soft and flexible to handle/process for desired configurations that can be retained after the 2nd stage reaction where a highly crosslinked, high modulus polymer network is generated through photo-hardening. Therefore, the two-stage polymers have a broad controllable range of material properties providing a promising approach to creating multifunctional polymeric structures. This dual material property feature of the two-stage reactive polymers allows potential applications such as shape memory actuators, biomedical devices, lithographic impression materials, and optical materials.[7, 60, 61] Nair and her co-workers developed and modified this thiol-acrylate two-stage polymer system by using different acrylate monomers and catalysts.[60, 61, 88] This non-stoichiometric thiol-acrylate system exhibits two distinguished sets of material properties between two stages, where the 1st stage network is formed via a base catalyzed Michael addition reaction, and the 2nd stage network is achieved by free radical polymerization through photo-crosslinking the excess acrylate functional groups into a highly crosslinked system. This thiol-acrylate two-

42

stage polymer system was also studied by other researchers to explore more applications in the related research fields. Ma et al. presented an effective approach using a similar acrylate-rich 1st stage elastomer with both photoinitiator and photoabsorber. The soft two-stage elastomer was then strained and irradiated by UV light to form a stiff skin, leading to surface wrinkling after release.[89] Podgorski et al. developed a nonuniformly crosslinked 2nd stage shape memory polymers that perform out-of-plane deformation upon programming.[90] Alzahrani et al. combined two-stage polymerization with photo-copper(I) -catalyzed azide alkyne cycloaddition to generate spatiotemporally controlled persistent wrinkles on the elastomeric surface.[91] Peng et al. modified the system with additional high refractive index monomers to achieve novel polymeric substrates with the ability to record holographic data.[63] Recently, Yakacki et al. developed a similar two-stage polymer system by using a diacrylate mesogen as acrylate functional group to fabricate liquid-crystalline elastomers (LCEs).[92] The 2nd stage photopolymerization reaction is coupled with uniaxial stretching to program a monodomain in LCEs sample achieving free standing two-way actuation. Glugla et al. demonstrated a rigid origami design by utilizing the photoinduced nonuniform swelling ratios across the two-stage polymer system.[64] The origami structure is fold in soft state and permanently fixed in rigid state to overcome the material property constrains in traditional self-actuated materials. Two-stage polymer systems can also be used to sequential cure thermosets and achieve flexible processing scenarios where a stable intermediate 1st stage polymer can be later fully cured to fulfill its final application requirements.[93]

Since two-stage reactive polymers have distinct material properties in each stage that can be used for achieving a variety of applications, it is important to develop a

photochemical and thermomechanical model to help understand the materials and guide their applications. To our best knowledge, no previous work has been done specifically on describing the behaviors of two-stage reactive polymers. Lendlein et al. developed a light activated polymer system with a second set of network that can be bonded or cleaved by applying specific wavelengths of light.[29] Rao et al. presented a model for this type of photo-induced shape memory polymers using the notion of multiple natural configurations, where each of the numerous networks has its unique stress-free configuration through photo-induced network transition.[94] This generalized model can help describe the stress field in the photo responsive system under deformation and irradiation at the same time. For the multiple natural configurations in photopolymer system, Long et al. also developed a phase evolution theory decomposing the entire polymer network into an original network and a photochemically altered network to describe the stress field in light activated polymers during UV radiation.[65, 80, 82] The programmed stress in a small volume fraction of the original network is released as it transforms into the reformed network during light irradiation. Ma et al. developed a photoviscoplastic model considering this permanent photoinduced elongation as a plastic-like deformation.[59] In this paper, we present a photo-thermomechanical viscoelastic model studying the significant property change and photoinduced viscoelasticity in the two-stage polymer system and validate the model by comparing with thermomechanical tests and shape fixing test. After introducing materials and experiments in Section 2, the photochemical and thermomechanical viscoelastic model is presented in Section 3. The modeling results are compared with the experimental results in Section 4 as well as discussion. Finally, the work is concluded in Section 5.

Two-stage reactive polymers[60, 61, 63] are able to further crosslink after gelation and this chapter describes their photochemical and thermomechanical behaviors. Experiments of the 2nd stage transition are conducted on two-stage reactive polymers with varied stoichiometric ratios of functional groups at elevated temperature while photocuring. Thermomechanical experiments show an obvious increase of glass transition temperature for polymeric specimen with excess acrylate functional groups and no change for the ones without left over acrylates. Further uniaxial tension tests reveal viscoelastic behaviors of the 2nd stage polymers.

3.2   Materials and Experiments

3.2.1   Materials

Pentaerythritol   tetra(3-mercaptopropionate)   (PETMP),   trimethylolpropane triacrylate (TMPTA), photoinitiator 2,2-dimethoxy-2-phenylacetophenone (Irgacure 651), and triethylamine (TEA) were purchased from Sigma-Aldrich (St. Louis, MO, USA). PETMP and TMPTA were mixed together in an amber color vial at stoichiometric ratios of 1:1, 1:1.5 and 1:2 between thiol and acrylate functional groups. Irgacure 651 (1 wt%) was added to the thiol-acrylate mixture and mixed thoroughly at 80 °C on a magnetic hotplate. TEA (0.8 wt%) was then added to the mixture and mixed vigorously on a vortex mixer. The final resin was then immediately sandwiched between two glass slides coated with Rain-X (SOPUS Products, Houston, TX) and separated by polyester shims. The glass slides with resin in between were then covered by tinfoil paper and placed in oven for 12 h at 70 °C. After thermal curing, the 1st stage polymer thin sheet was cut into 3 mm wide strips   with   various   lengths   needed.   PETMP   was   used   as   thiol   monomer   and

trimethylolpropane triacrylate (TMPTA) was purchased from Sigma-Aldrich together with the photoinitiator Irgacure 651 (2,2-dimethoxy- 2-phenylacetophenone). All samples contained triethylamine (0.8 wt%) as a catalyst for the first stage reaction and Irgacure 651(1 wt%) to initiate the second reaction. Thiol, acrylates and Irgacure 651 were mixed thoroughly first and then trimethylamine was added. The mixture was sandwiched between glass slides as mentioned in Chapter 2 shortly after mixing. Three kinds of samples were synthesized with various stoichiometric functional group ratios between thiol and acrylate (1:1, 1:1.5 and 1:2). To be more specific, 1:1 ratio sample has no excess acrylate functional groups and both of the other two samples have excess acrylate groups that can further crosslink upon irradiation. For the photocuring in the second stage of the reaction, samples were cured with 365 nm wavelength of light at 50 mW cm^{-2} by a UV lamp (OmniCure S2000).

3.2.2   *Thermomechanical Test, 2nd Stage Transition Test and Tension Test*

Three different sets of experiments were designed to measure photochemical reactions, thermomechanical properties and viscoelastic behaviors. All of these tests were conducted by using a dynamic mechanical analyzer (DMA, Model Q800, TA Instruments Inc., New Castle, DE, USA). A spot UV curing lamp (OmniCure S2000, Lumen Dynamics, Ontario, Canada) equipped with a 365 nm wavelength filter was used for all light exposures. Light intensity was fixed at 50 mWcm^{-2} by a radiometer (IL1400A, International Light Technologies, Peabody, MA) for all the tests. For the photochemical tests, specimens with dimensions approximately 4 mm $\times$ 5 mm $\times$ 0.15 mm were clamped between film tension fixtures under multi-strain mode of Q800 tester and preloaded by 1×10^{-3} N force to maintain straightness. A homemade mirror device was used to deliver

UV light from the top of the furnace, where the UV lamp fiber is located, to the mounted specimen inside the furnace. The sample was first heated to 100°C and held isothermal for 5 min to reach thermal equilibrium. During the experiment, the strain was oscillated at a frequency of 1 Hz with a peak-to-peak amplitude of 0.15% while the UV light was irradiated for 10 min before it was turned off for the last 5 min of the test. The storage modulus was measured and recorded through the entire test.

For the other two tests that are the thermomechanical tests and the tension tests, the 2nd stage samples were prepared by shining UV light at the 1st stage samples for 10 min on each side to ensure a fully cured condition. The experimental procedure of thermomechanical tests is similar to the photochemical tests but with a temperature sweep from -50 °C to 100 °C at a rate of 3 °C min^{-1} for measuring T_g of the samples with dimensions about 10 mm × 3.5 mm × 1 mm. As for the tension tests for studying the viscoelastic behaviors, specimens about 10 mm × 3 mm × 0.15 mm were stretched at a strain rate of 5% min^{-1} until fracture.

The same DMA Q800 is used to measure the T_g of the 1st stage polymers and the 2nd stage polymers in each thiol-acrylate ratio. Corresponding to the peak of the tan δ curve is defined as the glass transition temperature. The same preload and multi-strain module is used as described above. The temperature is first cooled down to -50°C and is then elevated to 100°C at a rate of 3°C/min. For 2nd stage transition test, a 1st stage specimen is mounted, heated to 100 °C and held isothermal while UV irradiation. The storage modulus is recorded at this rubbery state of the polymers. For tension tests, both the 1st stage polymers and the 2nd stage polymers are loaded at a rate of 5% min^{-1} until the sample breaks. The same tests are done at room temperature 23°C and at 100°C.

The experiments described above have been conducted and the preliminary experimental results are shown in this section. The results have shown obvious modulus increase as well as T_g increment as the two-stage reactive polymers have been photocured to the 2nd stage. As expected, this property change is not noticeable for ratio 1:1 case and ratio 1:2 case has much more significant property improvement compared to ratio 1:1.5 case since the 2nd stage provides denser crosslinking.

3.3   Model Description

To develop a photochemical and thermomechanical viscoelastic constitutive model for two-stage reactive polymers, we consider a general framework by coupling photomechanics with a viscoelastic multi-branch model. As light penetrates and propagates through the 1st stage polymers, the photons activate the embedded photoinitiators, generating free radicals and starting the growth of polymer chains by rapid sequential addition of the excess acrylate monomers to the active species. These photo-crosslinked polymer chains significantly increase the crosslink density in the polymer network resulting in a much higher elastic modulus macroscopically. The consequences of the photochemical reactions include thermomechanical property change and photo-induced viscoelasticity as will be discussed in the following sections.

Here, we assume the 1st stage polymer system has a full thiol conversion thus only the excess acrylate groups are evolved during the 2nd stage polymerization.[60] We also assume that the mechanics state in the first stage has no influence on the chemical reactions. Therefore, the following model is developed to start capturing the photochemical reactions during the 2nd stage evolution. A photopolymerization model is developed to describe the

48

free radical polymerization, and is then incorporated into a constitutive model to capture the photo-thermosviscoelastic behaviors of the two-stage polymer network.

3.3.1 Two-Stage Reactions

3.3.1.1 Overall Model

The total crosslink density, $v(t)$, is the summation of the 1st stage network, v_1, and the 2nd stage network crosslink density, $v_2(t)$, and is expressed in the following section. Hill's model is modified for calculating the crosslink density of the 1st stage network as shown in Eq. 23b.[95]

$$v(t) = v_1 + v_2(t), \tag{23a}$$

$$v_1 = \alpha \varphi_1 \left\{ \begin{array}{l} \dfrac{1}{2}(2p_1 - 1)[SH] \\ + \dfrac{1}{2}(3p_2 - 2)[C = C]_1 \end{array} \right\}, \tag{23b}$$

$$C_U(0) = [C = C]_0 - [C = C]_1, \tag{23c}$$

where p_1 and p_2 are the conversion of thiol and acrylate functional groups at the 1st stage, respectively. $[C = C]_0$ is the concentration of the initial double bond in the polymer resin system; $[C = C]_1$ is the concentration of the double bond consumed at the 1st stage and it equals to the thiol functional group concentration $[SH]$. φ_1 is a constant prefactor fitted by comparison with experimental results. As mentioned previously, we narrow our focus to the rapid photochemical and thermomechanical property change during the 2nd stage

evolution. Thus, the crosslink density at the 1st stage v_1 is time independent in the current model thus it is the crosslink density after thiol functional groups are fully reacted.

3.3.1.2 Photophysics and Photochemistry

The first physics to describe during the 2nd stage photo-crosslinking is light propagation through the material and the corresponding light induced chemistry. As mentioned, the polymer sample is gelled before this step and it is assumed to be a structurally and chemically homogeneous solid without internal boundaries. The scattering and the emission of light irradiation are also neglected. Therefore, light propagation through a chemically homogeneous media is described by the Beer-Lambert law, which states that the absorbance of a material sample is directly proportional to both its thickness and concentrations of the attenuating species,

$$\frac{dI(x,t)}{dx} = -A(x,t)I(x,t), \tag{24}$$

where $I(x,t)$ is the light intensity that is dependent on both the spatial coordinate which is along the thickness direction x, and time t, thus the light intensity at the entering surface I_0 is $I(0,t)$. $A(x,t)$ is the extinction field that describes the spatial variation of light due to absorption. The extinction field in the current study is characterized as

$$A(x,t) = \alpha_I C_I(x,t) + A_{matrix}, \tag{25}$$

where α_I is the absorptivity of photoinitiators; $C_I(x,t)$ is the concentration field of photoinitiators; A_{matrix} is the absorption from other species in the matrix such as

photoabsorber. Since no other attenuating species are added to the polymer system and we also ignore the absorption due to curing of the resin, A_{matrix} is set to zero.

During irradiation, light propagates through the 1st stage polymer inducing photochemical reactions of photoinitiators, generating free radicals and initiating photo-crosslinking of the excess acrylate functional groups. The free radical generation is governed by

$$\frac{\partial C_R(x,t)}{\partial t} = m\beta C_I(t)I(x,t) - k_t\big(C_R(x,t)\big)^n, \tag{26}$$

where $C_R(x,t)$ is the concentration of free radicals; β is a lumped constant parameter representing the molar absorptivity, the quantum efficiency and the monochromatic frequency of light; m is the number of free radicals formed upon the breakdown of one molecule of the photoinitiator and is precisely 2 in the current study. The second term on the right-hand side (RHS) of Eq. 26 describes the radical termination where k_t is the rate of termination and will be discussed later in this section. The exponent n defines the number of radical molecules for each termination reaction and is estimated as 2 in a bimolecular termination. Since free radicals diffuse much more slowly than photoinitiators, the diffusion of free radicals is not considered.

The photoinitiators are reacted with photons and generate free radicals. The evolution of the photoinitiator consumption is described by

$$\frac{\partial C_I(x,t)}{\partial t} = -\beta C_I(x,t)I(x,t) + D_I \nabla^2 C_I(x,t), \tag{27}$$

where the second term on the RHS of Eq. 27 captures the diffusion of photoinitiator with diffusivity D_I. The negative sign in the first term indicates the decay of photoinitiator concentration by the reaction.

The step following initiation is propagation where the newly generated radicals react with the excess acrylate functional groups. Assuming the concentration of the available unreacted double bond in excess acrylate functional group is $C_U(x,t)$, so the propagation is defined as

$$\frac{\partial C_U(x,t)}{\partial t} = -k_p(t)C_U(x,t)C_R(x,t), \tag{28}$$

where $k_p(t)$ is the rate coefficient of propagation and is time-dependent as shown in Eq. 28.

Propagation and termination reactions are dependent on the mobility of the reacting species including radicals and monomers. The fractional free volume model is used to describe the deceleration of propagation as well as termination during polymerization. As the 2nd stage network continues to crosslink, it significantly decreases the fractional free volume, decreasing the mobility of the unreacted species and slowing down the rate for both propagation and termination. Anseth et al. developed a model using one equation to describe the chain length independent propagation and termination.[96, 97] In this model, the

propagation rate coefficient, $k_p(t)$, and the termination rate coefficient, $k_t(t)$, are expressed by the following

$$k_p(t) = k_{p0} \left\{ 1 + \exp\left(A_p \left(\frac{1}{f(t)} - \frac{1}{f_{cp}} \right) \right) \right\}^{-1}, \tag{29}$$

$$k_t(t) = k_{t0} \left\{ 1 + \left[\exp\left(-A_t \left(\frac{1}{f(t)} - \frac{1}{f_{ct}} \right) \right) + \frac{R_{rd} k_p(t) C_U(t)}{k_{t0}} \right]^{-1} \right\}^{-1}, \tag{30}$$

where k_{p0} and k_{t0} are kinetic constants of propagation and termination at infinite free volume, respectively. A_p and A_t are fitting parameters that control the onset and rate of autodeceleration and autoacceleration, respectively. f_{cp} and f_{ct} are the critical fractional free volume at which the propagation and termination start to be controlled by the mobility of species. R_{rd} is the reaction diffusion parameter, or the ratio of kinetic constant at which termination is dominated by species' segmental motion. $C_U(t)$ is the available unreacted double bond concentration and is assumed to be isotropic in a thin polymer film. The fractional free volume $f(t)$ is determined from the following equations

$$f_m = 0.025 + \alpha_m (T - T_{gm}), \tag{31a}$$

$$f_p = 0.025 + \alpha_p (T - T_{gp}), \tag{31b}$$

$$\varphi_m(t) = \frac{1 - X(t)}{1 - X(t) + \frac{\rho_m}{\rho_p} X(t)}, \tag{31c}$$

$$f(t) = f_m \varphi_m(t) + f_p(1 - \varphi_m(t)), \tag{31d}$$

where the fractional free volume at the glass transition temperature is assumed to be 0.025,[98] α_m and α_p are the volume expansion coefficient, T is the temperature, T_g is the glass transition temperature, ρ is the density, φ_m is the volume fraction of monomer and $X(t)$ is the double bond conversion at the 2nd stage. The subscript m and p represent for monomer and polymer, respectively.

Equation (24) ~ (31) are coupled and can be numerically integrated for solving the evolution of unreacted double bond concentration, $C_U(t)$, during the 2nd stage photopolymerization. Owing to the balance of double bond concentration through the entire polymerization, reacted or bonded double bond concentration, $C_B(t)$, can be derived accordingly. Here we assume the crosslink density due to the 2nd stage photocuring, $v_2(t)$, is described as

$$v_2(t) = \alpha^{-\varphi_2} C_B(t), \tag{32}$$

where α equals to 1, 1/1.5, 1/2, is the initial stoichiometric ratio of thiol-acrylate functional groups in the polymer system, the exponent φ_2 is a fitting parameter that simplifies the complex relationship between bonded chains and crosslink density.

3.3.2 Constitutive Model

3.3.2.1   Overall Model Description

A 1D rheological representation of the proposed multi-branch model is shown in Figure 16. The mechanical elements consist of an equilibrium branch and several non-equilibrium branches placed in parallel. The equilibrium branch is a hyperelastic spring with a Young's modulus of E_{eq} to represent the equilibrium behavior, and each non-equilibrium branch is a nonlinear Maxwell element with an elastic spring and a dashpot placed in series. In the set of nonequilibrium branches, m branches are used to represent the relaxation behavior of the glassy mode and n branches are used to represent the relaxation processes of the rubbery state. It is necessary to note that the difference between glassy branches and rubbery branches is that the former ones possess yielding behavior while the latter ones do not. Detailed discussions on these nonequilibrium branches will be discussed later. The total Cauchy stress σ is

$$\sigma = \sigma_{eq} + \sum_{i=1}^{m+n} \sigma_{neq,i}, \tag{33}$$

where σ_{eq} is the Cauchy stress in the equilibrium branch that has a contribution due to the 1st and 2nd stage, and can be decomposed as follows

$$\sigma_{eq} = \sigma_{eq,1} + \sigma_{eq,2}, \tag{34}$$

with $\sigma_{eq,1}$ being the 1st stage contribution to the elastic stress and $\sigma_{eq,2}$ the 2nd stage contribution to the elastic stress. $\sigma_{neq,i}$ are the Cauchy stress in the i th glassy

nonequilibrium branches ($1 \leq i \leq m$), or in the ith rubbery nonequilibrium branches ($m + 1 \leq i \leq m + n$), respectively.
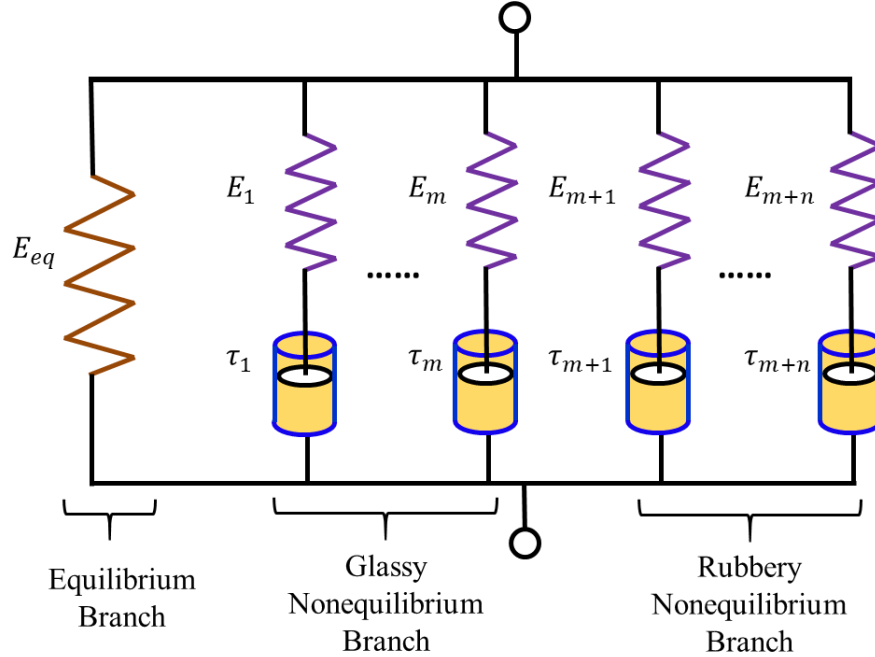
Figure 16. 1D rheological representation of the model.

3.3.2.2 <u>Kinematics</u>

To capture the physics as best as possible, we now give a discussion upon the kinematics throughout fabrication from liquid resin to the 2nd stage fully cured polymer. Initially the material consists of a liquid resin of two kinds of monomers and other chemical constituents such as photoinitiators and photoabsorbers where a network has yet to form, as shown in Figure 17. A loosely crosslinked network is formed upon thermally induced gelation after the 1st stage reaction. The associated volume shrinkage due to polymerization is difficult to measure accurately throughout the process for complex 3D geometries. Furthermore, the 1st stage polymer is sufficiently soft so its contribution to the viscoelastic response of the overall system is relatively trivial later on in the process after 2nd stage

curing due to significant modulus changes. Due to this added complexity we neglect this thermal shrinkage in the 1st stage cure in our model and use the loosely crosslinked post-thermally cured 1st stage as our reference configuration which will be denoted by $\mathcal{B}_0$. At this point the material is a gelled polymer and may deform as an elastomeric solid. Upon deformation into a new configuration, which will be denoted by $\mathcal{B}_1$, there is an associated deformation gradient $\mathbf{F}_1$ which maps infinitesimal neighborhoods of $\mathcal{B}_0$ to $\mathcal{B}_1$. At this point the material in configuration $\mathcal{B}_1$ may be subjected to light irradiation to cure the 2nd stage. During this 2nd curing process there may be an associated volume shrinkage due to the crosslinking of chains with finite extensibility. This volume shrinkage causes the material to occupy a new configuration $\mathcal{B}_2$ which has an associated deformation gradient $\mathbf{F}_2$ that maps infinitesimal neighborhoods in $\mathcal{B}_1$ to infinitesimal neighborhoods in $\mathcal{B}_2$. At this point if the loads used to deform the material into configuration $\mathcal{B}_1$ are released then the material will further deform into an elastically unloaded configuration due to the release of mechanical energy in the original 1st stage network. From this configuration, denoted by $\mathcal{B}_3$, the material may be deformed as a usual polymer assuming no other chemically induced microstructural changes occur within the material system after 2nd stage curing.
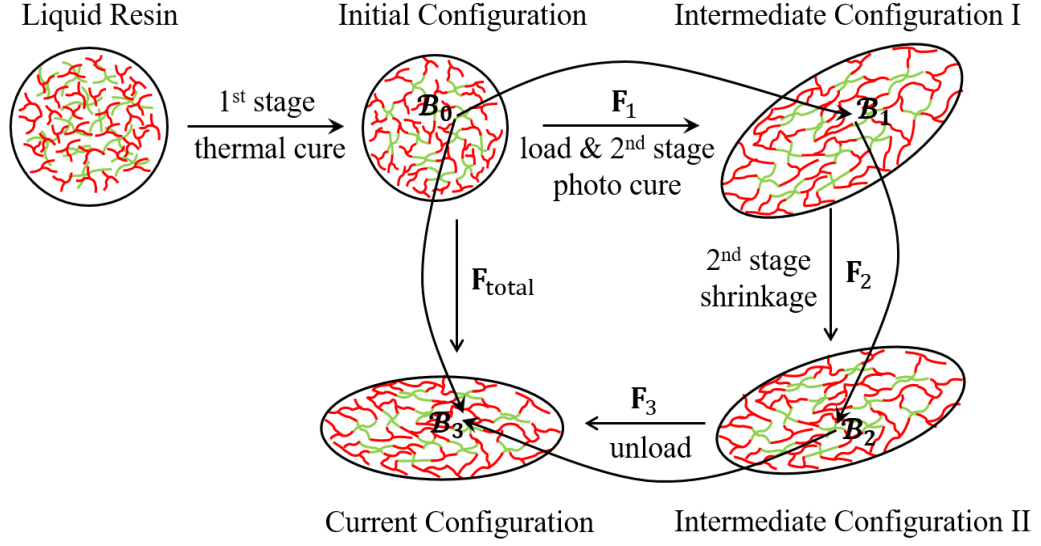
Figure 17. Kinematics of the liquid resin, initial, intermediate and current configurations.

To summarize the kinematics, consider a point in the "reference configuration" $\mathbf{X} \in \mathcal{B}_0$, a point in the initially deformed configuration $\mathbf{p}_1 \in \mathcal{B}_1$, a point in the configuration used to capture 2nd photoinduced shrinkage $\mathbf{p}_2 \in \mathcal{B}_2$ and finally a point in the elastically unloaded configuration. Using the above we can define deformation gradients $\mathbf{F}_1$ and $\mathbf{F}_2$ as follows

$$\mathbf{F}_1 = \frac{\partial \mathbf{p}_1}{\partial \mathbf{X}}, \tag{35a}$$

$$\mathbf{F}_2 = \frac{\partial \mathbf{p}_2}{\partial \mathbf{p}_1}, \tag{35b}$$

$$\mathbf{F}_3 = \frac{\partial \mathbf{x}}{\partial \mathbf{p}_2}. \tag{35c}$$

58

We further summarize the kinematics in terms of the particular physics at each step in the process below. Since the reference configuration being utilized is $\mathcal{B}_0$, the deformation gradient $\mathbf{F}_1$ is only due to the mechanical deformation. We may write this as follows

$$\mathbf{F}_1 = \mathbf{F}_{\mathbf{M},1}. \tag{36}$$

Similarly, the deformation gradient $\mathbf{F}_2$ as defined above is due only to photo-curing induced volume shrinkage and may be expressed as an isotropic tensor as follows

$$\mathbf{F}_2 = \mathbf{F}_{\mathbf{S},2} = J_2^{1/3}\mathbf{I}. \tag{37}$$

Finally, the deformation gradient $\mathbf{F}_3$ is due solely to mechanical response as it is defined above which can be multiplicatively decomposed into elastic and viscous parts due to the viscoelastic response of the polymer after the 2nd stage cure. Furthermore, due to parallel arrangement of the multibranch model the deformation gradients in each of the rubbery and glassy branches should be equal at all times. This can be expressed as

$$\mathbf{F}_3 = \mathbf{F}_{\mathbf{M},3}^1 = \mathbf{F}_{\mathbf{M},3}^2 = \cdots = \mathbf{F}_{\mathbf{M},3}^m = \mathbf{F}_{\mathbf{M},3}^{m+1} = \cdots = \mathbf{F}_{\mathbf{M},3}^{m+n}, \tag{38}$$

$$\mathbf{F}_{\mathbf{M},3}^i = \mathbf{F}_{\mathbf{M},3}^{i,e}\mathbf{F}_{\mathbf{M},3}^{i,v}, \tag{39}$$

where $\mathbf{F}_{\mathbf{M},3}^{i,e}$ is the elastic deformation gradient of the ith branch and $\mathbf{F}_{\mathbf{M},3}^{i,v}$ is the viscous deformation gradient of the ith branch. To ensure the deformations in our model remain physical, we put the following restrictions upon the deformation gradients

$$J_1 = det\mathbf{F}_1 > 0, \tag{40a}$$

$$J_2 = det\mathbf{F}_2 > 0, \tag{40b}$$

$$J_3 = det\mathbf{F}_3 > 0. \tag{40c}$$

For completeness, we introduce a relation for the total deformation gradient from the reference configuration after the thermal cure for the 1st stage to the deformed 2nd stage cured polymer as follows

$$\boldsymbol{F}_{total} = \mathbf{F}_{\mathbf{M},3}^{i}\mathbf{F}_{\mathbf{S},2}\mathbf{F}_{\mathbf{M},1} = J_2^{1/3}\mathbf{F}_{\mathbf{M},3}^{i,e}\mathbf{F}_{\mathbf{M},3}^{i,v}\mathbf{F}_{\mathbf{M},1}. \tag{41}$$

3.3.2.3 Constitutive Model for the First Stage Network

For the 1st stage network due to its elastomeric nature we choose to model this with a single equilibrium branch which will utilized the Arruda-Boyce eight chain model to account for the finite extensibility of the polymer chains within the network. The relation for $\sigma_{eq,1}$ is defined using the mechanical deformation gradient $\mathbf{F}_{\mathbf{M},1}$ as follows.

$$\boldsymbol{\sigma}_{eq,1} = \frac{v_1 k_B T}{3 J_{M,1}} \frac{\sqrt{N}}{\lambda_{\text{chain},1}} \mathcal{L}^{-1}\left(\frac{\lambda_{\text{chain},1}}{\sqrt{N}}\right) \bar{\mathbf{B}}_t{}' + K_1 (J_t - 1)\mathbf{I}, \tag{42a}$$

$$\bar{\mathbf{B}}'_t = \bar{\mathbf{B}}_t - \frac{1}{3\mathrm{tr}(\bar{\mathbf{B}}_t)\mathbf{I}}, \qquad \bar{\mathbf{B}}_t = \bar{\mathbf{F}}_t \bar{\mathbf{F}}_t{}^{\mathbf{T}}, \qquad \bar{\mathbf{F}}_t = J_t{}^{-1/3} \mathbf{F}_t \tag{42b}$$

$$\lambda_{\text{chain},1} = \sqrt{\mathrm{tr}(\bar{\mathbf{B}}_t)/3}, \qquad \mathcal{L}(\beta) = \coth \beta - 1/\beta. \tag{42c}$$

It should be noted that due to the choice of reference configuration and the assumption made above in the initial conditions of the photochemical equations v_1 is a constant throughout the process and therefore the modulus of the 1st stage networks does not change. The change in the overall material modulus is solely due to the evolution of the 2nd stage network. The shear modulus of this network is simply defined by $\mu_1 = v_1 k_B T$ and K_1 is the related bulk modulus which should be several orders of magnitude larger to ensure nearly incompressible behavior.

3.3.2.4 Constitutive Model for the Second Stage Network

3.3.2.4.1   Hyperelastic Equilibrium Branch

At the temperatures above T_g, the polymers are in the rubbery state and the Cauchy stress tensor in the equilibrium branch uses the Arruda-Boyce eight chain model,[99] i.e.,

$$\boldsymbol{\sigma}_{eq,2}(t) = \frac{v_2(t) k_B T}{3 J_{M,3}} \frac{\sqrt{N}}{\lambda_{\text{chain},2}} \mathcal{L}^{-1}\left(\frac{\lambda_{\text{chain},2}}{\sqrt{N}}\right) \bar{\mathbf{B}}_{M,3}{}' + K_2 (J_{M,3} - 1)\mathbf{I}, \tag{43a}$$

$$\overline{\mathbf{B}}'_{M,3} = \overline{\mathbf{B}}_{M,3} - \frac{1}{3\text{tr}(\overline{\mathbf{B}}_{M,3})\mathbf{I}}, \qquad \overline{\mathbf{B}}_{M,3} = \overline{\mathbf{F}}_{M,3}\overline{\mathbf{F}}_{M,3}{}^{\text{T}}, \qquad (43b)$$

$$\overline{\mathbf{F}}_{M,3} = J_{M,3}{}^{-1/3}\mathbf{F}_{M,3},$$

$$\lambda_{\text{chain},2} = \sqrt{\text{tr}(\overline{\mathbf{B}}_{M,3})/3}. \qquad (43c)$$

where $v_2(t)$ is the crosslink density of the 2$^{\text{nd}}$ stage polymer network as discussed in the previous section, k_B is Boltzmann's constant, T is the temperature, N is the number of Kuhn segments between two crosslink sites (and/or strong physical entanglements). The temperature dependent shear modulus $\mu_r(T)$ of the elastomer is derived by the kinetic theory of rubber elasticity and is given by vk_BT. K is the bulk modulus and is typically orders of magnitude larger than μ_r to ensure materials incompressibility ($J_M = 1$).

3.3.2.4.2   Viscoelastic Nonequilibrium Branches

For the viscoelastic behaviors in the nonequilibrium branches, it is assumed that all branches follow the same viscous flow rules but with variation of relaxation times among each other and difference of stress independency between glassy and rubbery branches as will be discussed in the following section. For the ith nonequilibrium branches, the deformation gradient can be further decomposed into an elastic part and a viscous part

$$\mathbf{F}_{M,3}^{i} = \mathbf{F}_{M,3}^{i,e}\mathbf{F}_{M,3}^{i,v}, \qquad (44)$$

where $\mathbf{F}_{M,3}^{i,v}$ is a relaxed configuration obtained by elastically unloading by $\mathbf{F}_{M,3}^{i,e}$. The Cauchy stress can be calculated using $\mathbf{F}_{M,3}^{i,e}$,

$$\sigma_{neq,i} = \frac{1}{J_{M,3}^{i,e}} \left[\mathbf{L}_{M,3}^{i,e}(T) : \mathbf{E}_{M,3}^{i,e} \right], \tag{45a}$$

$$J_{M,3}^{i,e} = \det\left(\mathbf{F}_{M,3}^{i,e}\right), \qquad \mathbf{E}_{M,3}^{i,e} = \ln \mathbf{V}_{M,3}^{i,e}, \qquad \mathbf{V}_{M,3}^{i,e} = \mathbf{F}_{M,3}^{i,e} \mathbf{R}_{M,3}^{i,eT}, \tag{45b}$$

where $\mathbf{L}_{M,3}^{i,e}(T)$ is the fourth order isotropic elasticity tensor in the ith nonequilibrium branch which is taken to be temperature dependent, in general, i.e.,

$$\mathbf{L}_{M,3}^{i,e}(T) = 2G^i(T)\left(\mathbf{I} - \frac{1}{3}\mathbf{I}\otimes\mathbf{I}\right) + K^i(T)\mathbf{I}\otimes\mathbf{I}, \tag{46}$$

where $\mathbf{I}$ is the fourth order identity tensor, G^i and K^i are shear and bulk moduli for each nonequilibrium branch, respectively. For the rubbery nonequilibrium branches ($m + 1 \le i \le m + n$), it is assumed that all the rubbery branches have the same shear modulus, i.e.

$$G^i(T) = v_t k_B T, \quad \text{for } m + 1 \le i \le m + n, \tag{47}$$

It is necessary to note that the shear modulus $G^i(T)$ in each rubbery nonequilibrium branch are equal to the shear modulus $\mu_r(T)$ in the equilibrium branch. Since the bulk modulus is used to enforce a nearly incompressible condition, $K^i(T)$ is chosen to be independent of temperatures and is set to be equal to K in the equilibrium branch (Eqs (12a) ~ (12c)). For the glassy nonequilibrium branches ($1 \le i \le m$), the shear modulus is taken to be independent of temperatures, i.e.

$$G^i(T) = \mu_g, \quad \text{for } 1 \le i \le m, \tag{48}$$

and $K^i(T)$ is calculated according to $G^i(T)$ using the Poisson ratio $v^i = v_g$,

$$K^i(T) = \frac{2(1 + v_g)}{3(1 - 2v_g)} \mu_g, \quad \text{for } 1 \le i \le m, \tag{49}$$

and the elastic modulus in each nonequilibrium branch is calculated as

$$E^i(T) = \frac{G^i(T)}{2(1 + v^i)}, \quad \text{for } 1 \le i \le m + n. \tag{50}$$

In each nonequilibrium branch ($1 \le i \le m + n$), the second Piola-Kirchoff stress in the intermediate configuration (or elastically unloaded configuration) and the Mandel stress are

$$\boldsymbol{S}_{neq,i} = J_{M,3}^{i,e}(\mathbf{F}_{M,3}^{i,e})^{-1}\sigma_{neq,i}(\mathbf{F}_{M,3}^{i,e})^{-T} \text{ and } \mathbf{M}_{neq,i} = \mathbf{C}_{M,3}^{i,e}\boldsymbol{S}_{neq,i}, \tag{51}$$

where $\mathbf{C}_{M,3}^{i,e} = \mathbf{F}_{M,3}^{i,eT}\mathbf{F}_{M,3}^{i,e}$ is the right Cauchy-Green deformation tensor. Typically, the Mandel stress is used to drive the viscous flow via the equivalent shear stress for inelastic materials

$$\dot{\gamma}_{neq,i,v} = \frac{\bar{M}_{neq,i}}{G^i(T)\tau_M^i(T, \bar{M}_{neq,i})}, \tag{52}$$

64

where the equivalent shear stress is defined as

$$\bar{M}_{neq,i} = \left[\frac{1}{2} \left(\mathbf{M}_{neq,i} \right)' : \left(\mathbf{M}_{neq,i} \right)' \right]^{1/2}, \tag{53}$$

where $\left(\mathbf{M}_{neq,i} \right)' = \mathbf{M}_{neq,i} - 1/3 \text{tr}(\mathbf{M}_{neq,i})\mathbf{I}$. The relaxation time $\tau_M^i(T, \bar{M}_{neq,i})$ is temperature and stress dependent, and will be discussed in the next section.

The viscous stress rate $\mathbf{D}_{M,3}^{i,v}$ is constitutively prescribed to be

$$\mathbf{D}_{M,3}^{i,v} = \frac{\dot{\gamma}_{neq,i,v}}{\sqrt{2}\bar{M}_{neq,i}} \mathbf{M}_{neq,i} \tag{54}$$

where $\mathbf{D}_{M,3}^{i,v}$ can be equal to the viscous spatial velocity gradient $\mathbf{L}_{M,3}^{i,v} = \dot{\mathbf{F}}_{M,3}^{i,v}(\mathbf{F}_{M,3}^{i,v})^{-1}$ by assuming the viscous deformation to be irrotational, and ignoring the spin rate $\mathbf{W}_{M,3}^{i,v}$. Therefore,

$$\dot{\mathbf{F}}_{M,3}^{i,v} = \mathbf{D}_{M,3}^{i,v}\mathbf{F}_{M,3}^{i,v}. \tag{55}$$

3.3.2.4.3   Relaxation Time and Time-temperature Shift Factor

The relaxation time of the rubbery branches is temperature dependent and is calculated according to the well-established thermorheological simplicity principle (Rubinstein and Colby, 2003),[100] i.e.

$$\tau^i(T) = \tau_0^i a_T(T), \quad \text{for } m + 1 \leq i \leq m + n, \tag{56}$$

where $a_T(T)$ is the time-temperature superposition shift factor and τ_0^i is the reference relaxation time at the temperature when $a_T(T) = 1$. The temperature influence on viscoelastic behavior depends on whether the material temperature is above or below T_g. At temperatures around or above T_g, the WLF equation is used,[101]

$$\log a_T = -\frac{C_1(T - T_M)}{C_2 + (T - T_M)}, \tag{57}$$

where C_1 and C_2 are material constants and T_M is the WLF reference temperature. When the temperature is below T_g, an Arrhenius-type behavior is used to describe a_T,[102]

$$\log a_T = -\frac{AF_c}{k_B}\left(\frac{1}{T} - \frac{1}{T_g}\right), \tag{58}$$

where A and F_c are material constants, k_B is Boltzmann's constant.

For the glassy nonequilibrium branches ($1 \leq i \leq m$), the polymer chain mobility is significantly reduced at temperatures below T_g thus the change in chain conformation is constrained. However, the applied stress can reduce such energy barrier, allowing the chain energy to overcome it and performing a yield-type behavior. As a consequence, the relaxation time in the nonequilibrium branches is not only a function of temperature but also stress and can be evaluated by an Eyring type of function,[103] i.e.

$$\tau^i\left(T, \overline{M}_{neq,i}\right) = \tau_0^i a_T(T) \exp\left(-\frac{\Delta G^i}{k_B T}\frac{\overline{M}_{neq,i}}{s^i}\right), \quad \text{for } 1 \leq i \leq m, \tag{59}$$

where ΔG^i is the activation energy, s^i is the athermal shear strength representing the resistance to the viscoplastic shear deformation in the material. To adequately consider the experimentally observed softening effects, the evolution rule for s^i is defined as

$$\dot{s}^i = h_0^i\left(1 - s^i/s_s^i\right)\dot{\gamma}_{neq,i,v}, \tag{60}$$

where $s^i = s_0^i$ when $\gamma_{neq,i,v} = 0$, and s_0^i is the initial value of the athermal shear strength, s_s^i is the saturation value, h_0^i is a prefactor and $\dot{\gamma}_{neq,i,v}$ is the viscous flow in glassy branches and is defined in Eq. 52. For the cases when $s_0^i > s_s^i$, Eq. 59 represents an evolution rule that characterizes the experimentally observed softening behavior of the material.

3.4 Results and Discussion

The constitutive relations were implemented into a MATLAB (Mathworks, Natick, MA, USA) program. The material parameters were first identified by fitting the experimental results and were later used to predict the property changes, such as modulus, T_g and viscoelasticity. Finally, we are investigating the shape forming behavior of two stage polymers by using the user material subroutine (UMAT) in the finite element software package ABAQUS (Simulia, Providence, RI, USA). This part of the study is currently under research and is not included in this dissertation.

3.4.1   Photomechanical Results

The rubbery modulus is gradually increased during the 2nd stage evolution because of the photoinduced crosslinking among the excess acrylate functional groups. The crosslinking density can be modeled as described in Eq. 23 and the experiments were carried out by shining UV light onto the specimen in DMA at high temperature 100 °C. Both the simulation results and the experimental results during the transition from the 1st stage to the 2nd stage are shown in Figure 18. The material parameters used in the photochemical model are presented in Table 1. It is important to note that the measured modulus from the DMA tests is originally the storage modulus and is approximated to be the rubbery modulus since the operation temperature 100 °C is much higher than the T_g of the polymer network thus all the nonequilibrium branches are melted making the equilibrium branch to be the only functional one.
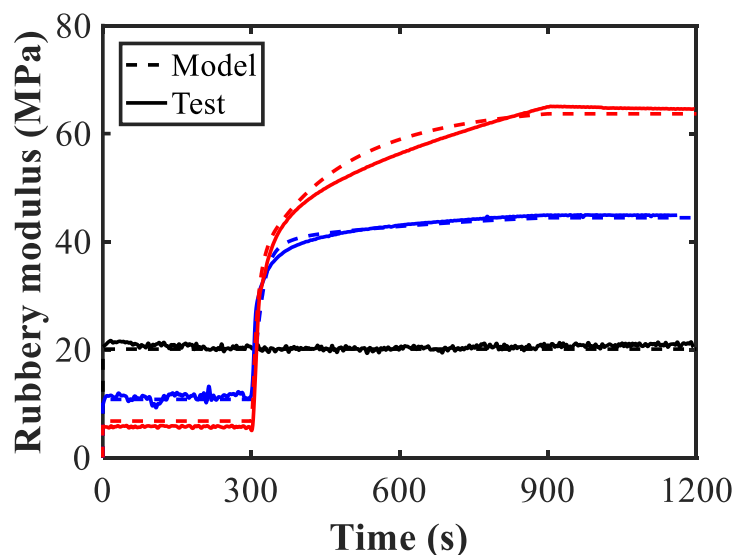
Figure 18. Photomechanical modeling (dash lines) and experimental results (solid lines) during the 2nd stage evolution for thiol acrylate functional group stoichiometric ratios 1:1 (black lines), 1:1.5 (blue lines), and 1:2 (red lines).

As shown in Figure 18, the rubbery modulus remains the same during the first 300 s of the tests when no UV light is irradiated. For samples with excess acrylate in the polymer network, their moduli grow very fast right after the UV irradiation due to the increase of the crosslinking density triggered by the 2nd stage photocuring. The rate of change decreases significantly after 30 s of UV irradiation and the modulus curve finally reaches plateau. The reaction rate slows down because of the decreasing free volume as photocuring continues that significantly affect the propagation rate as described in Eq. 31. Comparing the thiol acrylate ratios 1:1.5 and 1:2, the latter one has a lower 1st stage modulus and a higher 2nd stage modulus since more acrylate functional groups exist in the network that lowers down the crosslinking density at the 1st stage while boosts it at the 2nd stage. With more acrylate functional groups in the polymer network, the sample with ratio 1:2 has a higher propagation rate compared to ratio 1:1.5. The decrease of the propagation rate is also much slower for ratio 1:2 than ratio 1:1.5 since the former one has a larger initial free volume. However, the modulus for the specimen with thiol acrylate ratio 1:1 remains the same before and after UV irradiation. Even though free radicals can still be generated by the photoinitiator reaction upon irradiation, there is no excess acrylate functional groups in the polymer network for the 2nd stage photocrosslinking.

3.4.2   Thermomechanical Results

As shown in Figure 19, the thermomechanical modeling results are compared with the experimental results at both the 1st stage and the 2nd stage for thiol acrylate ratio 1:1, 1:1.5 and 1:2. The storage modulus and tanδ modeling results fit the testing results well in Figure 19(A). As expected, the experimental result curves in Figure 19(A) (1st stage) are almost overlapped with the ones in Figure 19(B) (2nd stage). The 1st stage and the 2nd stage

69

polymer networks have T_g of 26 °C and 25 °C, respectively. The rubbery moduli (measured at 100 °C) for the 1st stage and the 2nd stage are both 28 MPa. This close match is because ratio 1:1 polymer network has no photocrosslinking during UV irradiation thus we use the same set of parameters for both cases. In other words, the so-called 2nd stage for ratio 1:1 is the same as the 1st stage.

(A)　　　　　　　　　　　　　　　(B)
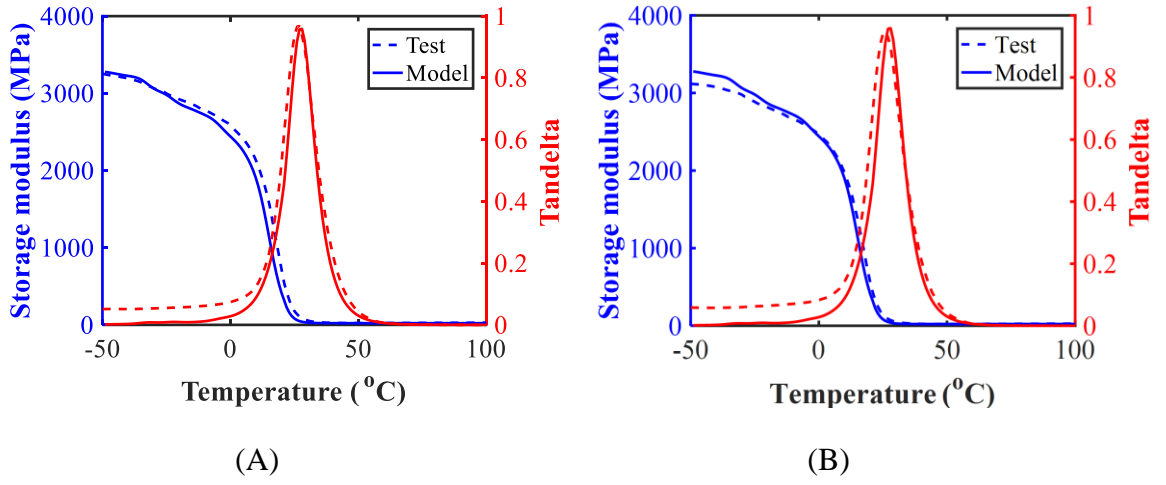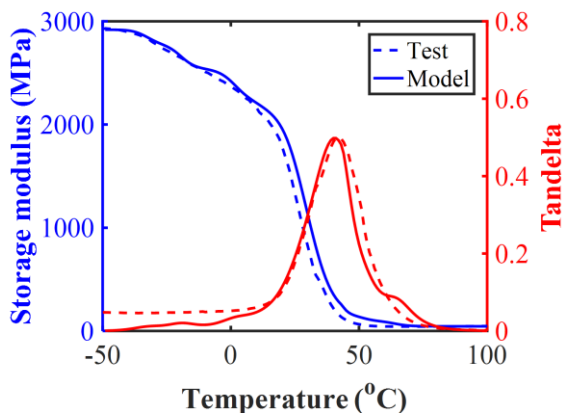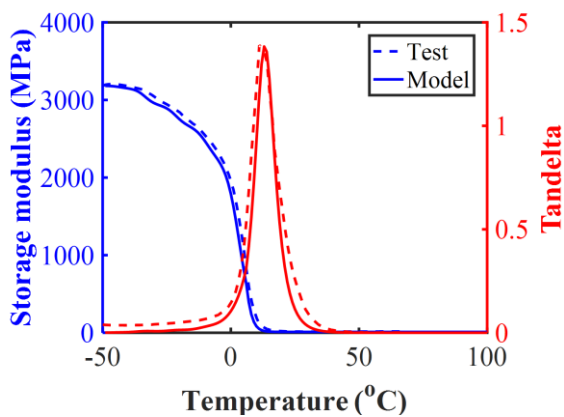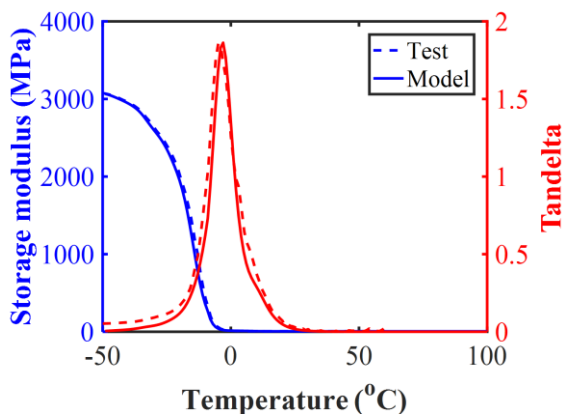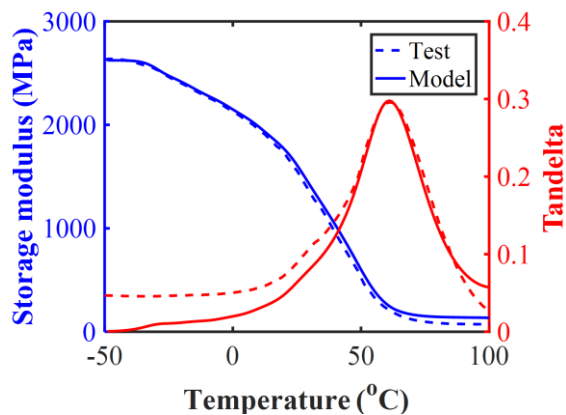
Figure 19. Thermomechanical modeling (solid lines) and experimental results (dash lines) with storage modulus (blue curves) and tanδ (red curves) of thiol acrylate stoichiometric ratio 1:1 (A, B), 1:1.5 (C, D) and 1:2 (E, F). (A, C, E) are the 1st stage and (B, D, F) are the 2nd stage.

Unlike the polymer network with thiol acrylate ratio 1:1 that is in its rubbery state at room temperature, the two-stage polymer system with thiol acrylate ratio 1:1.5 is in rubbery state at the 1st stage and is in glassy state at the 2nd stage under room temperature. As shown in Figure 19(C), the 1st stage polymer network has a T_g of 12 °C and a rubbery modulus of 17 MPa. Compared with ratio 1:1, polymer network with excess acrylate functional groups has a lower T_g and a smaller rubbery modulus at the 1st stage since the network is not fully crosslinked. However, the T_g and rubbery modulus increase to 42 °C and 48 MPa at the 2nd stage, respectively, as shown in Figure 19(D). The photocrosslinking of the excess acrylate functional groups significantly change the modulus at room temperature from 17 MPa to 2 GPa so that the polymer system changes from rubbery state to glassy state.

Similar to the case with ratio 1:1.5, the results of thiol acrylate ratio 1:2 show an increasing T_g and rubbery modulus after UV irradiation. As shown in Figure 19(E), the T_g at the 1st stage is only -4 °C since more unreacted acrylate functional groups exist in the system. The rubbery modulus at the 1st stage drops to 7 MPa that is the smallest among the three ratios. After the transition to the 2nd stage, a higher rubbery modulus about 76 MPa is achieved as shown in Figure 19(F). The T_g of the 2nd stage polymer network is also increased to 61 °C. Thus at room temperature, the two-stage polymer with ratio 1:2 is rubbery at the 1st stage and glassy at the 2nd stage.

While only three groups with different ratios have been investigated in this work, polymer system with other ratios can be similarly tested and the developed model can be used to predict the behaviors with the adjusted fitting parameters. However, the 1st stage polymer network may not reach the gel point if there are too much unreacted acrylates.

3.4.3   Viscoelastic Tension Results

Figure 20 shows the linear elastic behavior of the two-stage polymers with thiol acrylate ratio 1:1, 1:1.5 and 1:2. Both the 1st stage polymers and the 2nd stage samples were tested under tension mode by DMA. Two operation temperatures were used that are high temperature (HT at 100 °C) and room temperature (RT at 22 °C). As shown in Figure 20(A), the experimental results of the 1st stage polymer present a higher modulus at HT than the one at RT which can be explained by the entropy elasticity theory as described in Eq. 47. The same corresponding sets of fitting parameters are used in the viscoelastic model section as was used in the photomechanical and thermomechanical model sections. For this particular ratio 1:1 case, the same set of parameters is used for both the 1st stage and the 2nd stage polymers for the same reason as described in the previous section. When compared with the stress-strain relationship of the 2nd stage in Figure 20(B), both the rubbery modulus and room temperature modulus do not have an obvious change. The 2nd stage polymers also exhibit a linear elastic behavior as the model predicts which is the result of a negligible photoinduced property change.

(A)   (B)
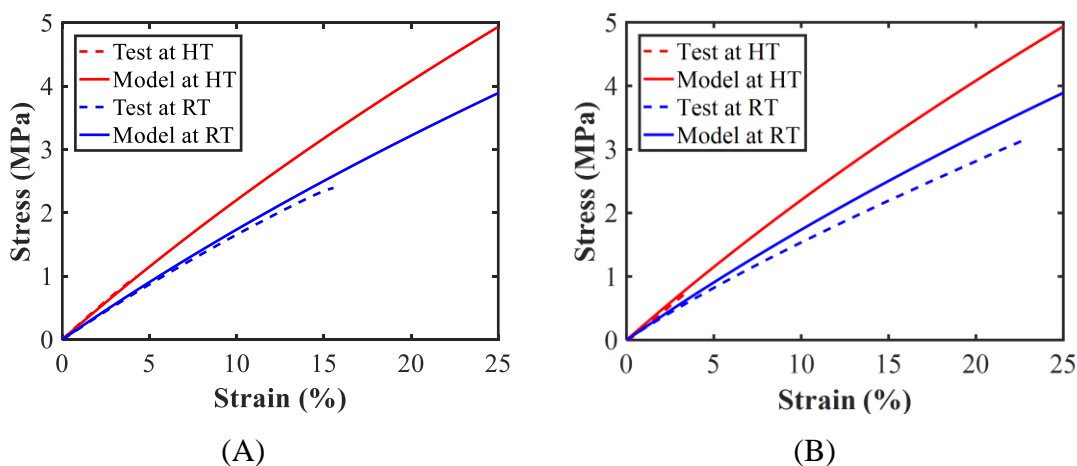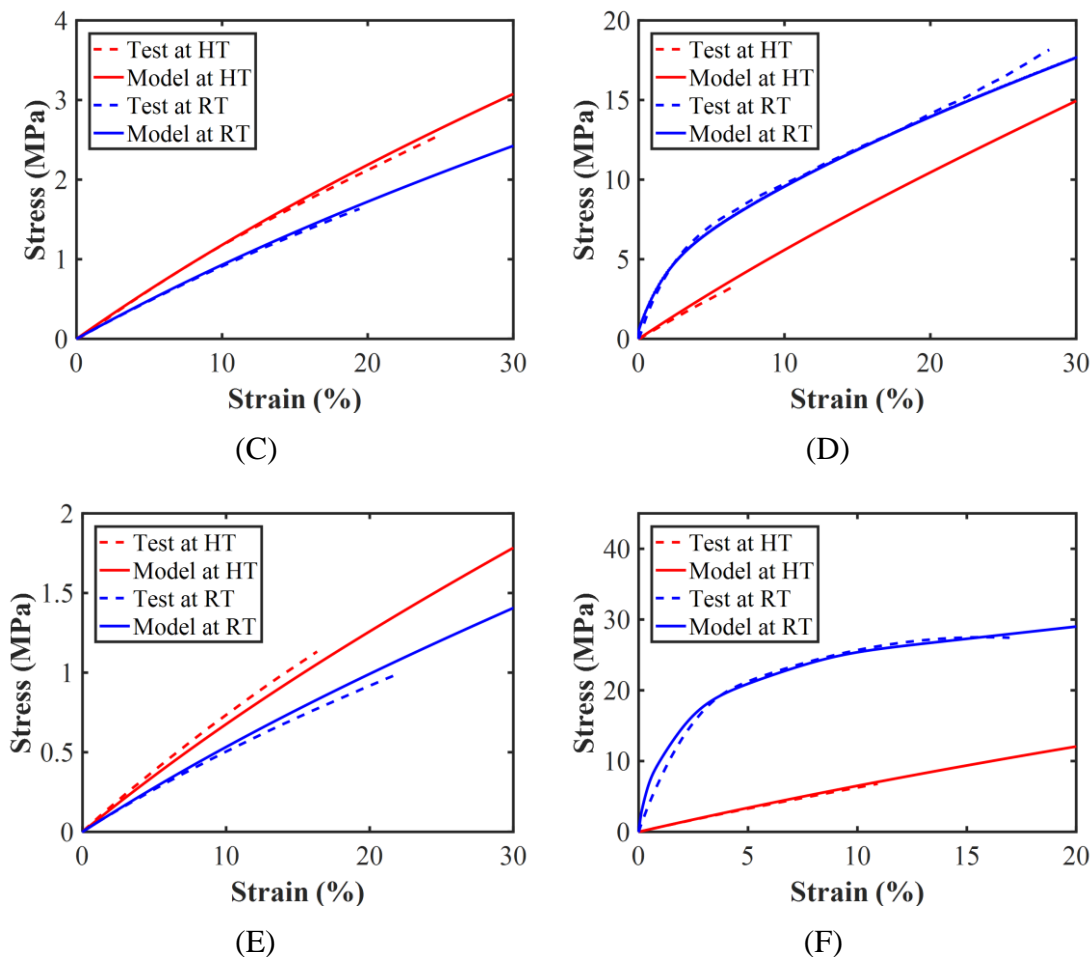
Figure 20. Viscoelastic modeling (solid lines) and experimental tension results (dash lines) at high temperature (red curves) and room temperature (blue curves) for thiol acrylate stoichiometric ratio 1:1 (A, B), 1:1.5 (C, D) and 1:2 (E, F). (A, C, E) are the 1st stage and (B, D, F) are the 2nd stage.

The same elastic behavior is observed at the 1st stage of polymer network with thiol acrylate ratio 1:1.5. As shown in Figure 20(C), the room temperature modulus and the rubbery modulus are significantly decreased compared to ratio 1:1 as the network is not fully crosslinked until UV irradiation. Figure 20(D) shows that not only the rubbery modulus at the 2nd stage is dramatically increased after photocrosslinking, the tension testing results at room temperature clearly exhibits a viscoelastic behavior. The viscoelasticity is introduced by the photocrosslinking of the acrylate functional groups that

increase the relaxation time in the nonequilibrium branches. The increasing viscosity in the nonequilibrium branches also has a significant influence on the nonequilibrium branch stress thus the polymer network exhibits larger strength at room temperature than at high temperature.

Figure 20(E) and 20(F) present the modeling and experimental results of thiol acrylate ratio 1:2. The rubbery modulus and room temperature modulus of the 1st stage are the smallest among the three cases. Since the viscosity of the 1st stage polymer network is neglectable, the stress-strain relationship is linear and the rubbery modulus is larger than room temperature modulus as shown in Figure 20(E). However, Figure 20(F) shows that the initial room temperature modulus is significantly larger than its rubbery modulus after the 2nd stage crosslinking due to the photoinduced viscoelasticity. The softening effect of the glassy branches contributes to the yielding when loading force continues to increase. This viscoelastic behavior is more obvious than the ratio 1:1.5 since there are more acrylates to provide photocrosslinks in the ratio 1:2 case.

3.4.4   Supplemental Materials

The photomechanical model is coupled with the thermomechanical model by substituting the rubbery modulus for the equilibrium branch and nonequilibrium rubbery branch elastic moduli in the multi-branch constitutive model. The material properties in the nonequilibrium glassy branches (τ_0^i, E^i for $1 \leq i \leq m$) and nonequilibrium rubbery branches (τ_0^i for $m + 1 \leq i \leq m + n$) are fitted by using nonlinear regression (NLREG) method. The elastic moduli of glassy branches and relaxation times at room temperature in each branch were estimated by approaching the storage modulus modeling results with the

experimental results. The same fitting parameters were then used to predict $\tan\delta$ to validate

the model. The temperature dependent storage modulus $E_s(T)$, loss modulus $E_l(T)$ and

$\tan\delta(T)$ are respectively expressed as

$$E_s(T) = E_{eq} + \sum_{i=1}^{m+n} \frac{E^i(T)w^2(\tau^i(T))^2}{1 + w^2(\tau^i(T))^2}, \tag{61a}$$

$$E_l(T) = \sum_{i=1}^{m+n} \frac{E^i(T)w\tau^i(T)}{1 + w^2(\tau^i(T))^2}, \tag{61b}$$

$$\tan\delta(T) = \frac{E_l(T)}{E_s(T)}, \tag{61c}$$

where w is the testing frequency, $\tau^i(T)$ and $E^i(T)$ are the relaxation time and the elastic

modulus in each nonequilibrium branch. The fitting parameters used in the

thermomechanical model are shown in Table 2 together with the ones used in the

photomechanical model.

Table 2. Parameters used in the constitutive model are listed along with reference from which the value was obtained ("calculated" means that it is calculated from the information provided by the vendor)

Parameter	Ratio 1:1	R1:1.5, 1st stage	R1:1.5, 2nd stage	R1:2, 1st stage	R1:2, 2nd stage	Units	Description	Reference
α_I	118	118	118	118	118	L mol^{-1} cm^{-1}	Photoinitiator molar absorptivity	Calculated
$C_I(0)$	0.0465	0.0458	0.0458	0.0454	0.0454	mol L^{-1}	Initial photoinitiator concentration	Calculated
A_{matrix}	0	0	0	0	0	cm^{-1}	Photoabsorber coefficient	Calculated
$C_R(0)$	0	0	0	0	0	mol L^{-1}	Initial radical concentration	Calculated

Symbol						Units	Description	
$[C=C]_0$	5.40	6.52	0	7.27	0	mol L^{-1}	Initial double bond concentration	Calculated
$[SH]$	5.40	4.35	4.35	3.64	3.64	mol L^{-1}	Thiol group concentration	Calculated
β	1.8×10^{-5}	1.8×10^{-5}	1.8×10^{-5}	1.8×10^{-5}	1.8×10^{-5}	s^2 kg^{-1}	Photoinitiation coefficient	Calculated
m	2	2	2	2	2	Dimensionless	Radicals generated per initiator	Fitted
n	2	2	2	2	2	Dimensionless	Radical termination exponent	Fitted
k_{p0}	13	13	13	13	13	L mol^{-1} s^{-1}	Propagation rate prefactor	Fitted
A_p	1.5	0.66	0.66	1.66	1.66	Dimensionless	Autodeceleration rate	Fitted
f_{cp}	0.11	0.062	0.062	0.11	0.11	Dimensionless	Propagation critical free volume	Fitted
k_{t0}	80	80	80	80	80	L mol^{-1} s^{-1}	Radical termination prefactor	Fitted
A_t	1.2	1.2	1.2	1.2	1.2	Dimensionless	Autoacceleration rate	Fitted
f_{ct}	0.05	0.05	0.05	0.05	0.05	Dimensionless	Termination critical free volume	Fitted
α_m	6.3×10^{-4}	6.3×10^{-4}	6.3×10^{-4}	6.3×10^{-4}	6.3×10^{-4}	°C^{-1}	Volume expansion coefficient	Fitted
T_{gm}	-60	-60	-60	-60	-60	°C	Monomer T_g	Measured
α_p	1.3×10^{-4}	1.1×10^{-4}	1.7×10^{-4}	1.0×10^{-4}	2.6×10^{-4}	°C^{-1}	Volume expansion coefficient	Fitted
T_{gp}	25	12	42	-4	61	°C	Polymer T_g	Measured
ρ_m	1	1	1	1	1	g/mL	Monomer density	Measured
ρ_p	1.3	1.3	1.3	1.3	1.3	g/mL	Polymer density	Measured
α	1	0.67	0.67	0.5	0.5	Dimensionless	Stoichiometric ratio	Calculated
φ_1	0.4	0.4	0.4	0.4	0.4	Dimensionless	1st stage crosslinking prefactor	Fitted

Parameter						Units	Description	Source
φ_2	1.4	1.4	1.4	1.4	1.4	Dimensionless	2nd stage crosslinking prefactor	Fitted
C_1	17.44	24.44	17.44	22.44	17.44	Dimensionless	WLF constant	Fitted
C_2	180	180	180	180	500	°C	WLF constant	Fitted
T_M	23	6	44	-9	63	°C	WLF reference temperature	Fitted
AF_c/k_B	-15500	-14500	-11500	-12500	-10000	K	Pre-exponential Arrhenius factor	Fitted
E^1	200	220	50	356	50	MPa	Modulus of the 1st branch	Fitted
E^2	1000	270	50	1000	52	MPa	Modulus of the 2nd branch	Fitted
E^3	200	220	50	83	170	MPa	Modulus of the 3rd branch	Fitted
E^4	400	590	50	79	252	MPa	Modulus of the 4th branch	Fitted
E^5	100	410	236	106	545	MPa	Modulus of the 5th branch	Fitted
E^6	700	530	306	590	397	MPa	6th branch	Fitted
E^7	300	480	940	476	760	MPa	7th branch	Fitted
E^8	300	420	1000	361	73	MPa	8th branch	Fitted
τ_0^1	2.8×10^{-6}	9.9×10^{-2}	1.0×10^{-1}	1.4×10^{-3}	2.0×10^{-6}	s	Initial relaxation time	Fitted
τ_0^2	5.6×10^{-2}	5.6×10^{-4}	1.0×10^{0}	5.9×10^{-2}	2.0×10^{-6}	s	Initial relaxation time	Fitted
τ_0^3	3.1×10^{-5}	3.1×10^{-5}	1.0×10^{1}	7.2×10^{-5}	1.3×10^{-4}	s	Initial relaxation time	Fitted
τ_0^4	1.0×10^{-1}	9.9×10^{-2}	2.6×10^{-6}	2.8×10^{-4}	7.1×10^{-4}	s	Initial relaxation time	Fitted
τ_0^5	2.4×10^{-4}	7.4×10^{-3}	2.0×10^{-5}	5.9×10^{-2}	4.4×10^{-3}	s	Initial relaxation time	Fitted
τ_0^6	5.6×10^{-2}	9.9×10^{-2}	6.3×10^{-4}	5.9×10^{-2}	1.6×10^{-2}	s	Initial relaxation time	Fitted
τ_0^7	1.7×10^{-3}	9.9×10^{-2}	2.0×10^{-2}	9.5×10^{-3}	5.3×10^{-2}	s	Initial relaxation time	Fitted
τ_0^8	1.1×10^{-2}	9.9×10^{-2}	4.6×10^{-2}	5.9×10^{-2}	1.2×10^{1}	s	Initial relaxation time	Fitted
τ_0^9	4.3×10^{-8}	2.2×10^{-6}	3.0×10^{-3}	5.9×10^{-2}	3.1×10^{-5}	s	Initial relaxation time	Fitted
τ_0^{10}	1.0×10^{-7}	2.2×10^{-6}	3.1×10^{-3}	5.9×10^{-2}	1.9×10^{-5}	s	Initial relaxation time	Fitted
τ_0^{11}	2.5×10^{-7}	2.2×10^{-6}	1.7×10^{-6}	1.3×10^{-4}	9.7×10^{-6}	s	Initial relaxation time	Fitted
τ_0^{12}	2.5×10^{-7}	9.9×10^{-2}	1.0×10^{-6}	1.6×10^{1}	2.0×10^{-6}	s	Initial relaxation time	Fitted

Parameter						Unit	Description	Source
ΔG^1	4.5×10^{-19}	4.5×10^{-19}	2.5×10^{-19}	2.5×10^{-19}	1.5×10^{-19}	J	Zero stress activation energy	Fitted
ΔG^2	4.5×10^{-19}	4.5×10^{-19}	1.0×10^{-19}	1.0×10^{-19}	1.5×10^{-19}	J	Zero stress activation energy	Fitted
ΔG^3	4.5×10^{-19}	4.5×10^{-19}	1.0×10^{-19}	1.0×10^{-19}	1.5×10^{-19}	J	Zero stress activation energy	Fitted
ΔG^4	4.5×10^{-19}	4.5×10^{-19}	4.5×10^{-19}	4.5×10^{-19}	1.5×10^{-19}	J	Zero stress activation energy	Fitted
ΔG^5	4.5×10^{-19}	4.5×10^{-19}	4.5×10^{-19}	4.5×10^{-19}	2.0×10^{-19}	J	Zero stress activation energy	Fitted
ΔG^6	4.5×10^{-19}	4.5×10^{-19}	4.5×10^{-19}	4.5×10^{-19}	5.0×10^{-20}	J	Zero stress activation energy	Fitted
ΔG^7	4.5×10^{-19}	4.5×10^{-19}	1.0×10^{-19}	1.0×10^{-19}	8.5×10^{-19}	J	Zero stress activation energy	Fitted
ΔG^8	4.5×10^{-19}	4.5×10^{-19}	1.0×10^{-19}	1.0×10^{-19}	4.0×10^{-19}	J	Zero stress activation energy	Fitted
h_0^1	2.0×10^5	2.0×10^5	3.0×10^5	3.0×10^5	2.0×10^5	MPa	Prefactor parameter	Fitted
h_0^2	2.0×10^5	2.0×10^5	2.0×10^5	2.0×10^5	2.0×10^5	MPa	Prefactor parameter	Fitted
h_0^3	2.0×10^5	2.0×10^5	2.0×10^5	2.0×10^5	2.0×10^5	MPa	Prefactor parameter	Fitted
h_0^4	2.0×10^5	2.0×10^5	2.0×10^4	2.0×10^4	2.0×10^5	MPa	Prefactor parameter	Fitted
h_0^5	2.0×10^5	2.0×10^5	2.0×10^5	2.0×10^5	1.0×10^5	MPa	Prefactor parameter	Fitted
h_0^6	2.0×10^5	2.0×10^5	2.0×10^5	2.0×10^5	2.0×10^5	MPa	Prefactor parameter	Fitted
h_0^7	2.0×10^5	2.0×10^5	2.0×10^5	2.0×10^5	1.0×10^5	MPa	Prefactor parameter	Fitted
h_0^8	2.0×10^5	2.0×10^5	5.0×10^3	5.0×10^3	2.0×10^5	MPa	Prefactor parameter	Fitted
s_s^1	2.0×10^4	2.0×10^4	5.0×10^4	5.0×10^4	2.0×10^4	MPa	Saturation shear strength	Fitted
s_s^2	2.0×10^4	2.0×10^4	6.0×10^4	6.0×10^4	6.0×10^4	MPa	Saturation shear strength	Fitted
s_s^3	2.0×10^4	2.0×10^4	6.0×10^4	6.0×10^4	3.0×10^4	MPa	Saturation shear strength	Fitted

s_s^4	2.0×10^4	2.0×10^4	2.0×10^4	2.0×10^4	5.0×10^4	MPa	Saturation shear strength	Fitted
s_s^5	2.0×10^4	2.0×10^4	2.0×10^4	2.0×10^4	5.0×10^4	MPa	Saturation shear strength	Fitted
s_s^6	2.0×10^4	2.0×10^4	2.0×10^4	2.0×10^4	2.0×10^4	MPa	Saturation shear strength	Fitted
s_s^7	2.0×10^4	2.0×10^4	3.0×10^3	3.0×10^3	2.0×10^4	MPa	Saturation shear strength	Fitted
s_s^8	2.0×10^4	2.0×10^4	3.0×10^3	3.0×10^3	3.2×10^4	MPa	Saturation shear strength	Fitted
s_0^1	6.5×10^4	6.5×10^4	6.0×10^4	6.0×10^4	3.0×10^4	MPa	Initial shear strength	Fitted
s_0^2	6.5×10^4	6.5×10^4	1.5×10^4	1.5×10^4	1.5×10^4	MPa	Initial shear strength	Fitted
s_0^3	6.5×10^4	6.5×10^4	1.5×10^4	1.5×10^4	1.5×10^4	MPa	Initial shear strength	Fitted
s_0^4	6.5×10^4	6.5×10^4	6.5×10^4	6.5×10^4	1.5×10^4	MPa	Initial shear strength	Fitted
s_0^5	6.5×10^4	6.5×10^4	6.5×10^4	6.5×10^4	2.5×10^4	MPa	Initial shear strength	Fitted
s_0^6	6.5×10^4	6.5×10^4	6.5×10^4	6.5×10^4	2.5×10^4	MPa	Initial shear strength	Fitted
s_0^7	6.5×10^4	6.5×10^4	2.0×10^3	2.0×10^3	1.5×10^4	MPa	Initial shear strength	Fitted
s_0^8	6.5×10^4	6.5×10^4	2.0×10^3	2.0×10^3	4.2×10^4	MPa	Initial shear strength	Fitted

3.5 Conclusions

Two-stage reactive polymers are active polymers with controllable properties such as tunable modulus and T_g. With certain programming steps and manipulation of the training parameters, two-stage polymers can be used as functional polymers that are easy to be tailored at the 1st stage and stiff at the 2nd stage upon irradiation. Thus, a photo-thermomechanical viscoelastic model is necessary to be developed to study the underlining mechanism. In this chapter, we developed a constitutive model to describe the photochemical and thermomechanical behaviors of two-stage reactive polymers. A simplified photochemical model is first developed to capture the modulus change during photocuring at the 2nd stage. Then the model is implemented into a multi-branch

constitutive model to capture the thermomechanical behaviors of two-stage polymers both at their 1st stage and 2nd stage. We also observe photoinduced viscoelasticity in the 2nd stage polymeric specimen and use this modified model to understand and explain the behavior.

CHAPTER 4.   3D PRINTING OF POROUS MATERIALS USING PHOTCURABLE RESIN

Porous polymeric materials have a wide range of applications, including tissue scaffolds, catalyst supports, membrane filters, *etc*. This chapter presents a new fabrication method to prepare components of porous materials by combining 3D printing with salt leaching. Sacrificial salt particulates and photocurable resin are mixed and used as the ink. 3D objects are then printed in a customized Digital Light Processing (DLP) printer. Owing to the interconnection of salt particles in the objects, porous polymeric components can be obtained upon salt leaching. Multiple pore sizes can be achieved by using selectively sieved salt powders in the ink formula. This method is very simple to implement for different photocurable resins to create 3D porous objects with complicated shapes. In addition, this new method has the advantages of self-supporting and can be used to print hollow components, especially the part with Droste effect (Russian doll). As examples, we demonstrate a shape memory effect by using shape memory polymers as the resin and 3D printing shape memory foams. Dual-pore scaffolds are also 3D printed with potential applications in tissue engineering. In addition, the porous components can be used as a template for embedding conductive material to obtain 3D printed objects that function as flexible conductive components. Finally, the pores can be filled with a second material to obtain a composite with tunable modulus. The work presented in this chapter has been published in *Materials Horizons* in 2017.[104]

4.1 Introduction

Porous polymers have attracted increasing research interest due to their light weight and high surface area, making them excellent candidates for a variety of applications, including filtration,[105] catalyst,[106] drug release,[107, 108] cell scaffolds,[109, 110] gas storage and separation,[111] electrode materials for energy storage,[112] templates for structure replication,[113] *etc*.[114] Many methods of preparing porous polymers have been developed, including gas foaming,[115, 116] phase separation,[117, 118] high internal phase emulsion,[119, 120] breath figure,[121, 122] direct templating,[123, 124] *etc*. In a gas foaming process, thermoplastic polymers are solubilized in a pressured container with aerating gases at high temperature for hours before cooling or heating to the desired foaming temperature. The subsequent depressurization to ambient pressure allows the nucleation and growth of gas voids.[116] Templating methods are also typically used. For example, researchers have developed both water-in-oil (W/O) and oil-in-water (O/W) high internal phase emulsions (HIPE) where a photocurable precursor is used as a continuous phase in W/O and forms a porous skeleton after evaporation of the dispersed aqueous droplets,[120] while porous structures with interconnected polymer beads are created in the case of O/W.[125] In these HIPE methods, preparing resins with controllable emulsion concentrations is a challenge. A relatively simple approach is to use the so-called porogens, such as waxes, sugars, salts and other soluble particulates, which can be leached away after the curing of the polymer resin, if the porogens form a continuous phase in the resin. The porosity and the pore size can be effectively controlled by the choice of the porogen. Although a porosity lower than 60% is hard to obtain, as the porogens cannot form a continuous phase to be leached

completly; this method can reach up to 96% porosity and is relatively simple to implement.[123]

The traditional porous polymer preparation methods lack design flexibility and customization. For instance, molds are typically needed for each shape, or postprocessing such as machining is necessary in order to create desired shapes. Moreover, some of the methods described above need special preparation conditions such as high temperature or high pressure. 3D printing, or additive manufacturing, is well known for its flexibility in creating components with complex structures and shapes, making them ideal for applications that require personalization and less waste of raw materials. As introduced in Chapter 1, 3D printing is a method to fabricate 3D objects in a layer-by-layer manner.[49-52] For polymers, the most widely used methods are FDM, which is based on extruding melted thermoplastic polymers, SLA, which selectively cures photopolymers in a bath of resin by using a raster laser, polyjet printing, which inkjets photocurable resin onto the substrate followed by UV curing, SLS, which sinters polymer powders into 3D model, and binder jetting, which sprays binder to glue powdered polymers. In the SLA approach, the raster laser can be replaced by a projector and the entire layer is cured at once.[126] This method is referred to as the DLP method. Compared with SLA, DLP is relatively fast and is low cost. In recent years, 3D printing methods have started to be used for porous polymeric structures. Krajnc and his coworkers have developed a method that combines W/O HIPE with DLP 3D printing, and they have prepared porous polymeric materials layer-by-layer.[120] Magdassi et al.[125] developed a reverse ink that is O/W HIPE; using this they 3D printed porous structures with interconnected polymeric beads. The continuous aqueous phase could be replaced by metallic inks to demonstrate conductive applications.

Recently, Cosgriff-Hernandez et al.[127] developed a photocurable emulsion W/O ink that can be extruded from a direct-write printer and retain its shape while curing. However, the HIPE ink synthesis needs relatively complicated preparation steps. Cox et al.[128] 3D printed porous scaffolds for bone tissue application using a binder-powder system, and they gained micropores from the imperfect packing of powder particles. However, these non-designed microscale pores lack control and the designed millimeter scale pores from Computer Aided Design (CAD) model are too large to be applicable to other applications.

In this chapter, we introduce a new method by combining DLP 3D printing with the salt leaching method to print porous polymeric components. The inks used for 3D printing were photocurable resins mixed with salt particulates. Three kinds of inks were used, including a PEGDA (poly(ethylene glycol) diacrylate) ink, a Standard Clear ink (Autodesk, Inc. San Rafael, CA, USA) and a Spot-E ink (Spot-A Materials, Barcelona, Spain); the latter two are commercially available. Several components, including a relatively complex model of trefoil knot, have been 3D printed to demonstrate the feasibility of this method. The pore size of the printed objects depends on the size of the salt particulates. Since the ink itself acts as a support during printing and is leachable after printing, this method provides a solution to 3D print objects that are fully encapsulated by another object. This new approach is simple to operate and can be used for many photocurable resins to achieve various functionalities, including porous scaffolds for tissue engineering, shape memory foams and porous templates for conductive material infiltration.

Besides the work published in the paper, some following-up work have been done and is presented in this chapter. These updates are mainly focused on metalizing the 3D

printed porous template and thus creating porous metallic parts based on the polymer structures. The metalized 3D printed porous polymeric structures have random distributed pores. When compared to the other 3D printing methods of metals including powder bed fusion, metal binder jetting and SLS. However, none of the above techniques are targeted on manufacturing highly porous metallic structures that can be used as lightweight materials, catalyst carriers, electrodes, *etc*. Since polymers are not conductive so that traditional electroplating cannot be used to deposit thin metal layer on porous polymeric materials. One possible and promising solution is to utilize electroless nickel deposition as described in the following sections.

4.2   Experimental Section

4.2.1   Materials and Ink Preparation

Three kinds of photocurable resins were used in this work. The first resin is poly(ethylene glycol) diacrylate (PEGDA, Mn=250) purchased from Sigma-Aldrich (St. Louis, MO, USA). The PEGDA resin is mixed with Irgacure 819 (1.0 wt%) and Sudan I (1.0 wt%) to enable photocurability. The second type of resin is a Standard Clear resin purchased from Autodesk, Inc. (San Rafael, CA, USA). The third resin is a Spot-E resin obtained from Spot-A Materials (Barcelona, Spain). Both Standard Clear and Spot-E are commercial 3D printing inks and are photocurable in the near UV and visible spectrum. Other materials used in this paper including ethylene glycol (EG), photoinitiator Irgacure 819 (phenylbis(2,4,6-trimethylbenzoyl) phosphine oxide), photoabsorber Sudan I, conductive ink PEDOT:PSS (poly(3,4-ethylenedioxythiophene)-poly(styrenesulfonate) 1.3 wt% dispersion in H_2O, conductive grade), and salt particulates (sodium chloride) were

purchased from Sigma-Aldrich. The salts are manually sifted by 300 µm and 180 µm sieves to prepare coarse (> 300 µm) salts and fine salts (180~300 µm), respectively. The extra-fine grade (75 ~ 180 µm) is prepared by grinding the salts first and then sifting by 180 µm and 75 µm sieves. The sieves with pore size 75 µm, 180 µm and 300 µm were purchased from H&C sieving systems (Columbia, MD, USA). Each of the three photocurable resins is manually mixed with salt particulates in a volume ratio approximately 26%:74%. Essentially, the 3D printing ink is the final mixture of photocurable resin and salt particulates. We refer to the three ink mixtures as PEGDA ink, Standard Clear ink and Spot-E ink, correspondingly.

4.2.2   Custom-made DLP Apparatus

Once the ink was prepared by mixing salt particulates and photocurable resin, it was loaded onto a customized printing platform, which consists of three components, including a feeding container, a rotating blade, and a printing piston. The design of this porous 3D printer is based on a DLP 3D printer, which is shown in Figure 21(a). The printing piston is attached to a motion stage (MTS50-Z8, Thorlabs Inc, Newton, NJ, USA) that moves vertically, controlled by Thorlabs APT software. The rotating blade is attached to a motor controlled by an Arduino board (model UNO R3). Both the printing platform and the rotation motor are adhered to the desktop. The DLP projector (Vivitek D912HD, optics modified for 30 ~ 70 micron pixels) is hung over the printer on a homemade frame and the projected images are the cross-sections of the CAD model sliced by CreationWorkshop (DataTree3D, Dallas, TX, USA). By using MATLAB with Arduino add-on, we are able to synchronize the motion stage, the rotation motor and the project during printing.

4.2.3 Mechanical Tests

Thermomechanical tests, uniaxial compression and tension tests were conducted by using a dynamic mechanical analyzer (DMA, Model Q800, TA Instruments Inc., New Castle, DE, USA). For thermomechanical test, solid specimens approximately 0.15 mm thick, 3 mm wide and 10 mm long were machined from a larger sample of cured Spot-E and PEGDA. A specimen was mounted between film tension fixtures under multi-strain mode of Q800 tester and preloaded by 1×10^{-3} N force to maintain straightness. The rectangular specimen was first heated to 100 °C and held isothermal for 10 min to reach thermal equilibrium. During the test, the strain was oscillated at a frequency of 1 Hz with a peak-to-peak amplitude of 0.15% while the temperature was decreased from 100 °C to 0 °C at a rate of 3 °C min^{-1}. The temperature corresponding to the peak of the tan δ curve is defined as the glass transition temperature. For tension tests, samples with the same dimension were loaded at a rate of 1 N min^{-1} until break. For compression tests, both porous and solid cubes with dimensions approximately $5\times5\times5$ mm^3 were cut from the larger 3D printed sample. The specimen was placed at the center between the compression clamps, and a preloaded force of 1×10^{-3} N was applied to measure the actual height. The test was run under controlled force mode at a rate of 3 N min^{-1} up to 18 N.

4.2.4 Shape Memory Tests

The Spot-E 3D printed porous foam was tested for its shape memory behaviors. A typical shape memory cycle consists of two steps: programming step and recovery step. In the programming step, the porous cube was first compressed on a hotplate at 45 °C, which was above its T_g of 37.5 °C measured by DMA. The compressed cube was then transferred

into ice water while maintaining the deformation to fix its shape as the temperature was below its T_g. During the free recovery step, the cube was put onto the hotplate at 70 °C. The same cube was tested multiple times to demonstrate its repeatability.

4.2.5   SEM Imaging

Field emission scanning electron microscope images were taken using a Hitachi FE-SEM SU8010 instrument (Hitachi, Ltd., Chiyoda, Tokyo, Japan). To investigate the pore size and distribution of the 3D printed components, samples near the core location of the components were cut with a sharp knife and fixed on the specimen stub by using conductive adhesive tape before observation. Parameters for the FE-SEM included accelerating voltages at 1 kV with a current of 10 mA. Images with magnifications of 40×, 120× and 180× were taken and shown in this paper.

4.2.6   Micro-CT Porosity Measurement

Quantitative porosity measurements were conducted using a micro-computed tomography platform (Micro-CT, Zeiss Metrotom, Oberkochen, Germany), with an effective spatial resolution of 11.95 µm/voxel. The X-ray tube of the tomographic platform was used under scanning conditions of 40kV and 200 µA, corresponding to an 8 µm focal spot size. During the tomographic scan, the porous samples were rotated in incremental steps over a total angular range of 360° to facilitate 3D image acquisition. The stack of digital slices of the porous samples generated by Micro-CT was imported into MATLAB to reconstruct 3D structure, analyse the pore morphology and pore size, and measure the porosity. Detailed information about Micro-CT process and data postprocessing can be found at previous work.[129]

4.2.7 Electroless Nickel Deposition

The whole process includes surface cleaning, sensitizing, surface activation and actual plating. The 3D printed parts are first cleaned by immersing in an acetone bath followed by immersing in NaOH solution. After surface cleaning, the cleaned parts are sensitized by immersing in an aqueous solution containing $SnCl_2 \cdot 2H_2O$ and 37% HCl. The surface is activated with palladium catalyst by immersing in solution containing PdCl and 37% HCl. Finally, the activated parts are metallized with nickel by immersing in a bath of nickel chloride and sodium hypophosphite. An important and repeated step is dipping and washing in distilled water bath after each chemical treatment step.

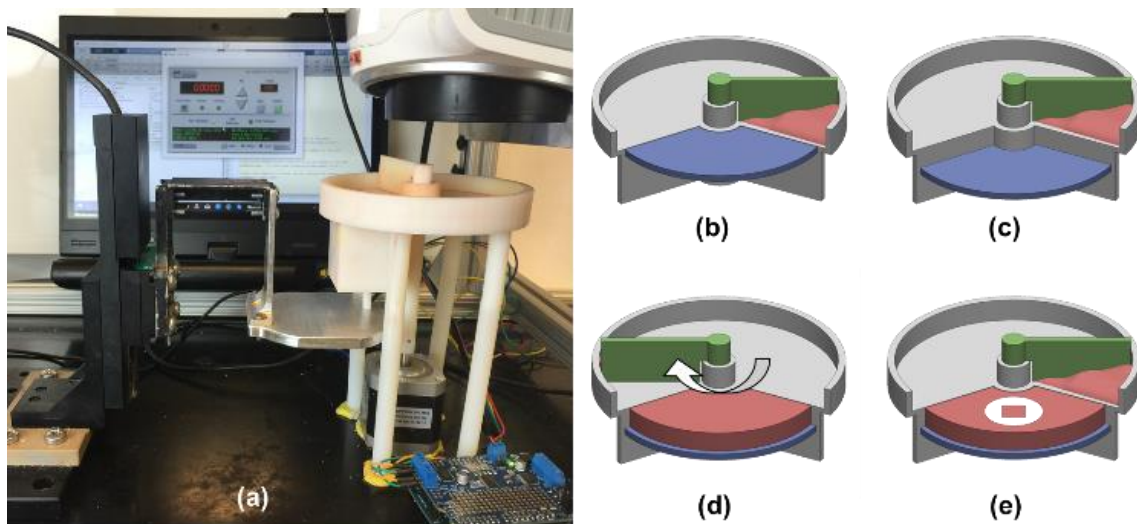## 4.3 Results and Discussion

4.3.1 3D Printing Process

Figure 21. (a) 3D printer setup and schematics (b-e) showing the printing process. (b) Starting position. (c) Printing piston moves down and creates a gap. (d) Fill the gap with one layer of ink. (e) Photocuring of a pattern.

A printing process is depicted in Figure **2**1(b-e). At the beginning, the printing piston stands by and is levelled with the surface of the feeding container as shown in Figure 1(b). When the printing starts, the printing piston moves down by 200 µm, driven by the vertical motion motor. This creates a gap as shown in Figure 1(c). Then the rotating blade starts to sweep the ink at a speed of 4 rpm onto the lowered printing piston, and smooths the surface at the same time (Figure 1(d)). After the rotating blade returns to its original location, the projector is turned on and projects the light with the part cross-section pattern to initiate polymerization of the resin as shown in Figure 1(e). In this paper, each layer was photocured for 10 s at a light intensity of 10.6 mW cm^{-2}. The bright square on the printing piston in Figure 1(e) indicates the irradiated area, which is on the top of the piston. After one cross-section is cured, the printing piston is lowered by another layer thickness of 200 µm and the printing process continues. In the current approach, each layer can be printed within 25 s and a 10 mm tall structure takes about 20 min. A real-time printing process can be found in video in the supplemental materials online. Pores in the printed object are generated by salt leaching inside a 2000 mL beaker full of water. The printed components are suspended in the beaker to avoid salt saturation near the bottom of the beaker. Depending on the size of the object, the salt leaching takes 10 min to 6 hours. Once the salt leaching finishes, the porous structures are placed in an oven at 80 °C for two hours to dry.
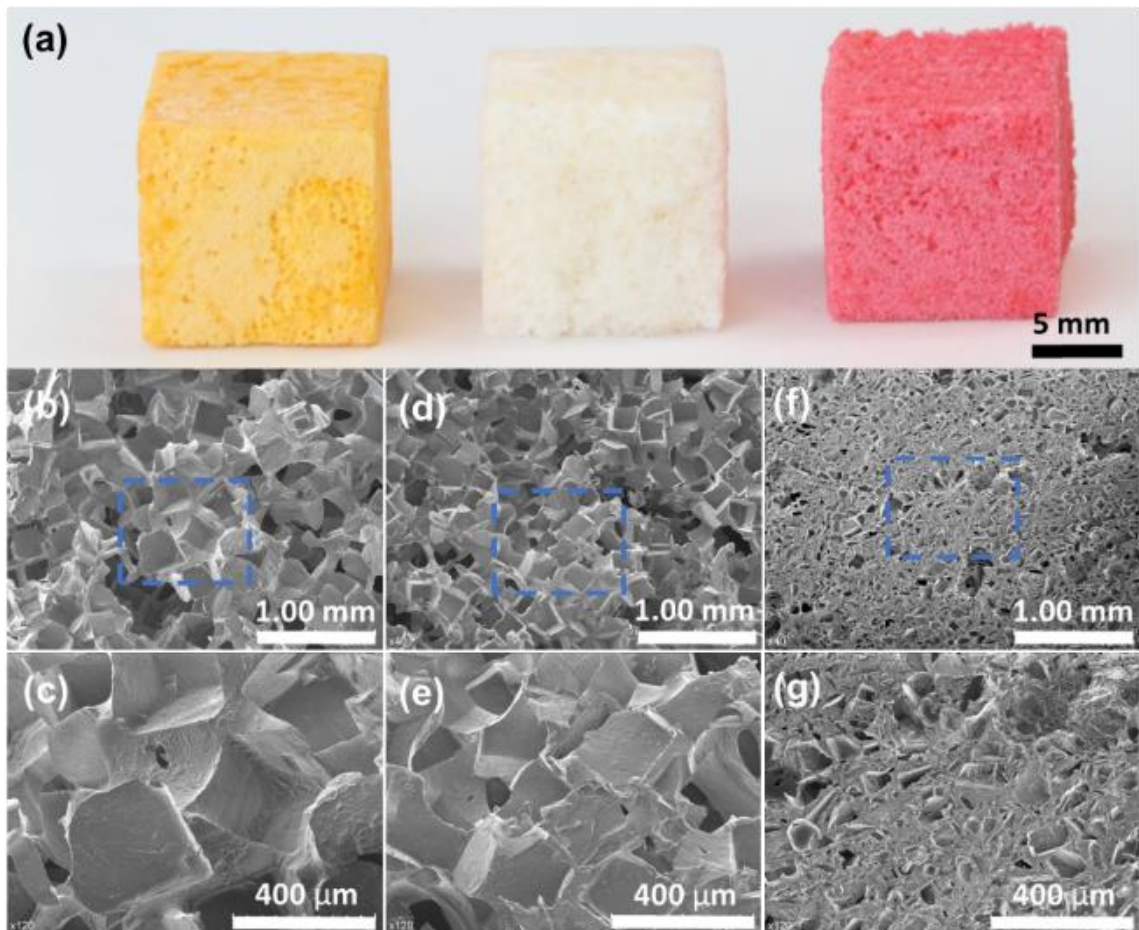
Figure 22. (a) Cubes 3D printed by using extra-fine PEGDA, Standard Clear and Spot-E ink from left to right. SEM images of the porous structures printed by using (b) coarse, (d) fine and (f) extra-fine Spot-E ink; the dashed rectangular areas in (b), (d) and (f) are zoomed in and shown in (c), (e) and (g), respectively.

4.3.2 *Characterization of Ink and Porous Structures*

To characterize the printing quality, we first printed a simple structure of a cube. Here, the salt particulates were ground and sifted for three different size ranges: coarse (> 300 µm), fine (180~300 µm) and extra-fine (75~180 µm). In order to maintain an interconnected sacrificial template phase, the three photocurable resins were mixed with large amount of salt particulates in a fixed volume ratio 26%:74% as described. The rheological behaviour of each resin was measured by using a viscometer (DV2T,

Brookfield Engineering, Middleboro, MA, USA) with CPA-41Z spindle at 0.1 rpm and the result is shown in Figure S1. The ink viscosity is significantly affected by the large amount of the salt particulates thus it behaves like a paste. Photocalorimetry tests have been conducted to measure the extent of crosslinking in each kind of the inks using differential scanning calorimeter (DSC, model Q200, TA Instruments Inc., New Castle, DE, USA). The comparison of photo-DSC results, as shown in Figure S2, show that each ink has a heat released above 95% of its corresponding pure resin. Therefore, the influence of salt particulates on the extent of photocrosslinking is negligible. In printing, the platform moves down for 200 µm, which is the current minimum achievable layer thickness comparing the size of the extra-fine salt particulates. Since this gap is smaller than the coarse and fine salt particulates, it implies that the coarse and fine ink may need two printing cycles to completely fill the gap. However, it does not affect the quality of the print when the targeted object is a cube and a better resolution can be achieved by further sifting the ink to a narrower range such as 75~100 µm.

Figure 22(a) shows the three cubes that were printed by using extra-fine PEGDA, Standard Clear and Spot-E ink, respectively. It presents the good quality of the cubes, demonstrating this method can be applied to different resin to achieve porous objects. 3D printed Spot-E cubes with varied salt sizes were sliced into small pieces for studying their pore structures using FE-SEM. As shown in Figure 22(b) and 2(g), the cube printed by coarse ink has large cubic voids (average pore size 380 µm) as the cavities are formed by leaching of salt cubes, and the voids are randomly distributed and interconnected. It also shows that
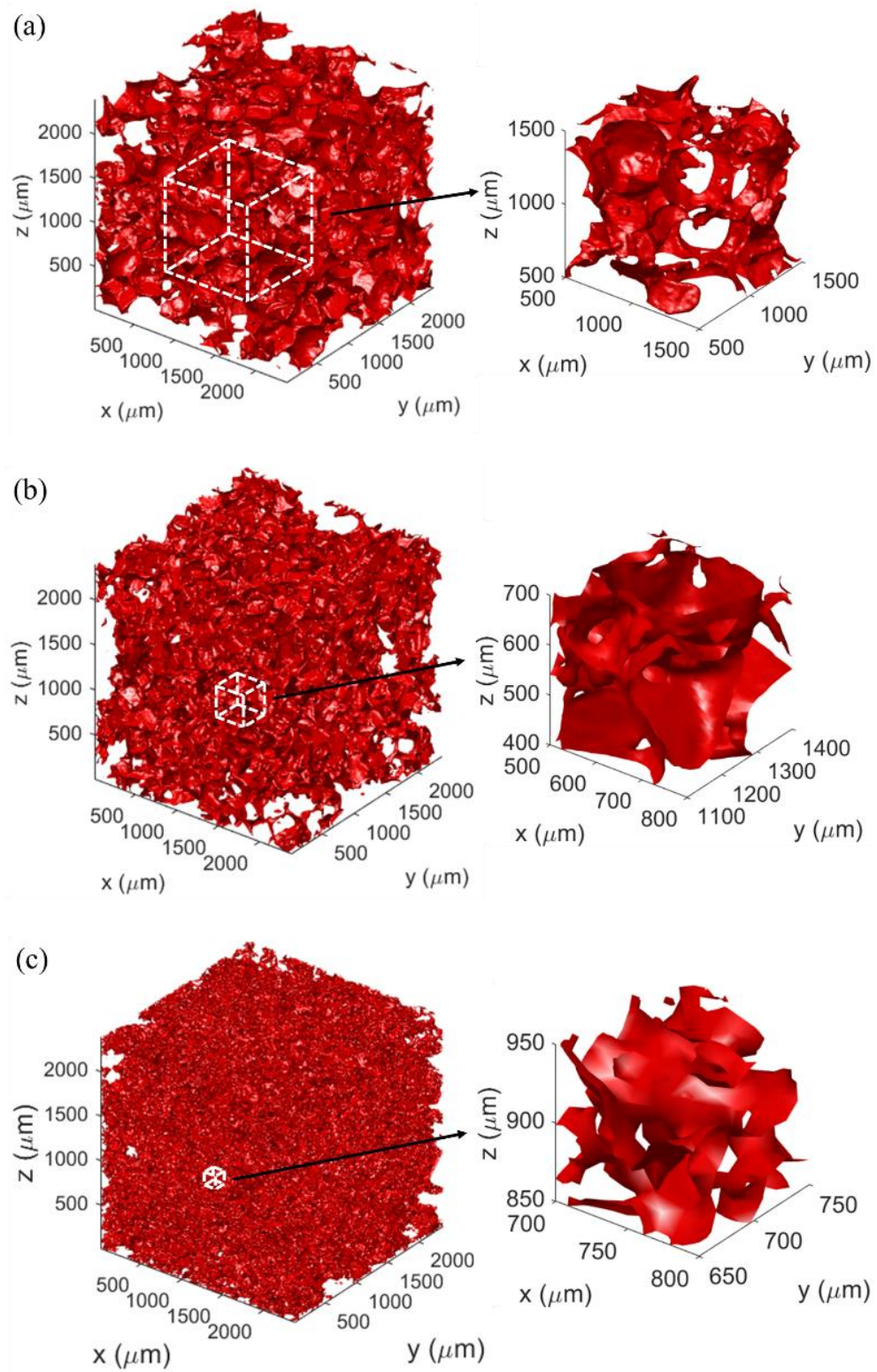
Figure 23. Micro-CT scanning results of porous cubes 3D printed by using (a) coarse, (b) fine and (c) extra-fine Spot-E ink.

some extra-large voids exist in the porous structure, and the sizes of these voids are obviously larger than any salt cubes. Most likely, these unusual voids were once a pile of several salt particulates. These salt cubes were so close-packed that almost no photocurable resin penetrated the core, or the resin in the gaps between them could not be photocured into a connected network and thus formed a much larger cavity after salt leaching. The pore structure and distribution of the fine cubes in Figure 22(d) do not have obvious differences compared to the coarse cubes, but the pore size (average pore size 228 µm) as is noticeably smaller than that of the coarse cubes. The pore size (average pore size 91 µm) is further reduced when the extra-fine ground salts are used as template in the ink, as shown in Figure 2(f). The pore structures are completely arbitrary and some pore sizes are even smaller than the lower bound of 75 µm. These tiny pores might be due to the combination of the imperfect packing of the salt particulates and the survival of the ultra-fine salt particulates. To further investigate, an ultra-fine ink with salt particulates (<75 µm) was used for 3D printing cubes. However, the ink behaved more paste-like, and it became difficult to deposit the ink onto the printing platform. Moreover, the ultra-fine salts in a cube printed with the help of manual interference could not be fully leached out. It is possible that when the size of the salts decreases to the ultra-fine range, a complete interconnection of the salts cannot be achieved. In other words, the possibility for ultra-fine salt particulates to contact with each other is much lower than it is for the coarse, fine or extra-fine salts. Thus most of the salt particulates are encapsulated by the cured polymers and cannot be leached out. This may also explain why porous structures with porosity lower than 60% are very hard to achieve by the salt leaching approach.[123]
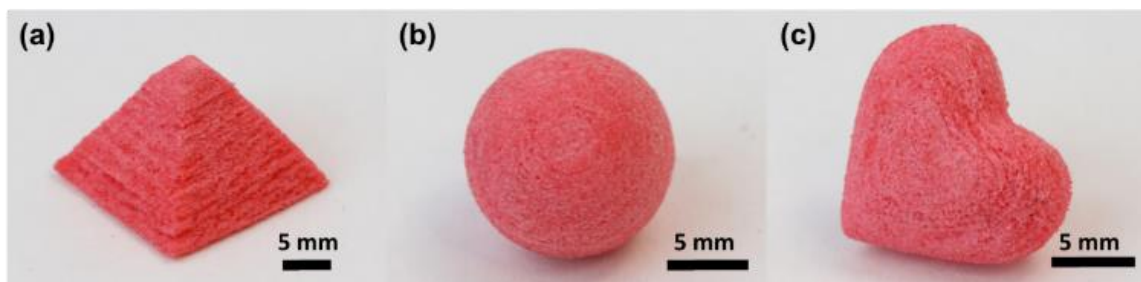
95

Figure 24. 3D printed porous structures including (a) pyramid, (b) sphere and (c) heart shape.

Moreover, the porosity of each Spot-E cubes was quantitatively measured by Micro-CT as shown in Figure 23. The differences in pore size among the three cubes are more visually obvious when shown in the 3D structures. The zoom-in pictures show that the pores are indeed both randomly distributed and interconnected. According to the postprocessing results in MATLAB, the final porosities for the coarse, fine and extra-fine were 73.9%, 76.5% and 72.9%, respectively. The average porosity of the tested three cubes is 74.4% and is very close to the volume of the salt in the ink which is 74%. Deviations may due to the inhomogeneity in the manually mixed ink. The pore size ranges for the coarse, fine and extra-fine were 350 μm – 450 μm, 200 μm – 250 μm, and 55 μm – 100 μm, respectively. These results are consistent with SEM images. The possible explanations for the existence of the pore size smaller than 75 μm in the extra-fine sample was discussed above.

4.3.3   3D Printed Porous Structures

To further demonstrate the flexibility of this 3D printing technique, multiple structures were printed using extra-fine Spot-E resin. Figure 24 shows three printed objects where the level of difficulty to print each object increases from left to right. Compared to

the pyramid (Figure 24(a)), the sphere (Figure 24(b)) required much more precise control of the curing time and the layer thickness. Moreover, multiple heart models were printed in different positions, including front to back as shown in Figure 4(c), and upside down thus the two round tips were first isolated and then merged together.
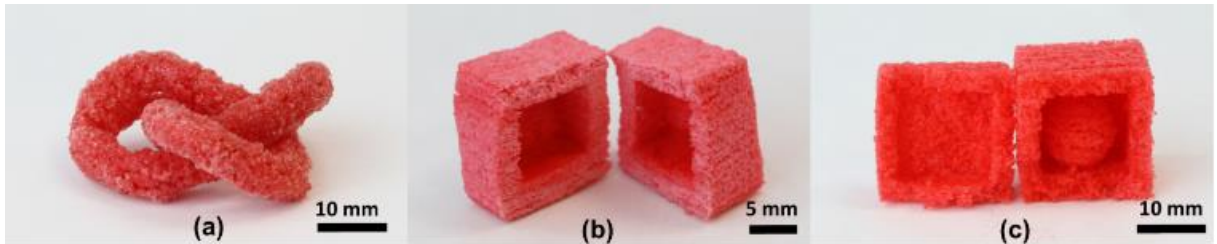

Figure 25. 3D printed (a) trefoil, (b) hollow cube and (c) ball in a hollow cube.

During printing all uncured ink remains as it is and becomes the supporting structure for the object. Therefore, there is no need to create additional supporting structures. In Figure 25(a), a porous trefoil knot was printed; this relatively complicated structure can be 3D printed without using any special supports. Besides the advantage of being self-supporting, the uncured ink can be used to create a hollow structure. For instance, the hollow cube shown in Figure 25(b) was originally printed as one piece while the uncured ink in the middle behaved as a support to the roof layers. During the salt leaching step, not only were the salts dissolved, but the uncured Spot-E resin was also flushed out of the cube through pores, generating the hollow core inside of the cube. Due to the hydrophobicity of the uncured resin, this flushing step was done under running water along with gentle squeezes. The hollow cube in the photo was cut in two halves to prove this additional advantage compared to traditional 3D printing using polymer powders. Furthermore, and more interestingly, free structures can be 3D printed with one inside

another without any connections (similar to the so called Droste effect). To prove this concept, a ball was printed inside of a hollow cube as shown in Figure 25(c). The ball and the hollow cube had no connections and were printed in one printing process, followed by salt leaching. The whole structure was one piece by appearance and only revealed its encapsulated sphere after cutting, as shown in the online video resourses.

4.3.4   Dual-pore Scaffolds and Multi-ink Printing

Besides the microscale pores generated by salt leaching, macroscale pores can be implemented to achieve dual pore sizes with scale variation. Figure 26 shows the cylindrical scaffold with dual pore sizes and SEM images of the pore structures. The scaffold CAD model[128] is shown in Figure 26(a) and the printed scaffolds using Spot-E and PEGDA are shown in Figure 26(b) and (c), respectively. One quarter of both the CAD model and the scaffolds was cut off to show their internal details. PEGDA was chosen as an alternative resin to show the potential application of this 3D printed porous scaffold in tissue engineering, because of its good biocompatibility, non-immunogenicity, and resistance to protein adsorption.[130] The printed components have porous structures of both microscale and macroscale. The microscale pores were created by pure salt leaching of the extra-fine salts. On the other hand, the macroscale pores were designed in the CAD model with 2 mm pore size and were generated by removal of the uncured ink during salt leaching. The SEM images of the PEGDA scaffold are shown in Figure 26(d,e) where the microscale pores are evenly distributed in the scaffolds and are interconnected as expected. Based on other researchers' study, the microscale randomly distributed pores provide a high cell density, and the macroscale designed pores help maintaining a high cell viability due to their functionality as efficient nutrient/oxygen supplies.[131]
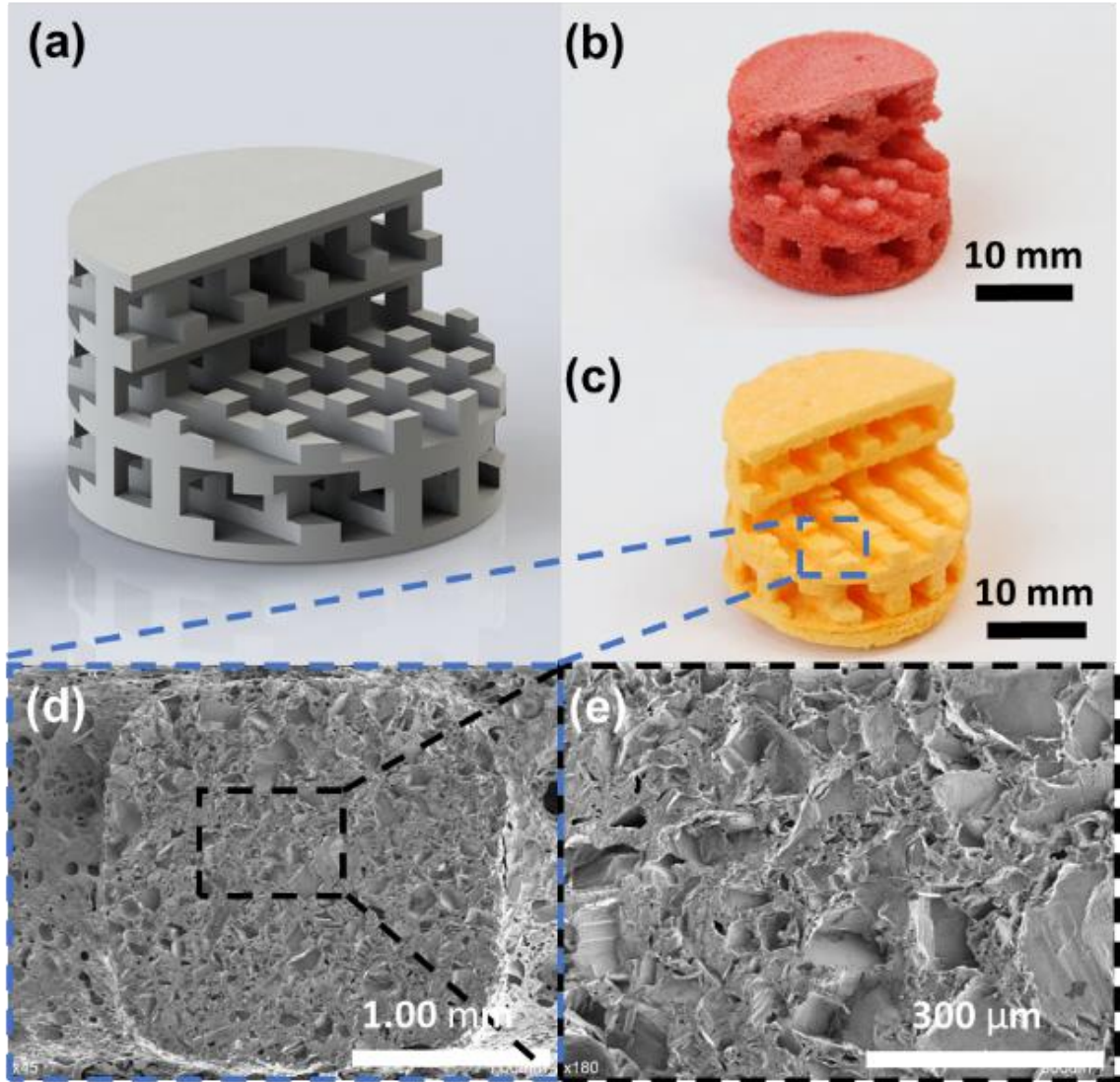
Figure 26. 3D printed scaffold with macro pores designed in CAD model and micro pores generated by salt leaching.

By using a CAD design, the micro-macro pores can also be controlled to provide more functionality. However, the micro-pore size is dependent only on the salt particulates in the ink and is fixed in one layer after printing. Here, we are able to control the pore size distribution vertically by pausing the printing and switching the ink. A cube contains coarse, fine, and extra-fine pores, and a solid roof from the bottom to the top can be printed successfully as shown in Figure 27(a). The solid section can also be sandwiched between

porous sections as shown in Figure 27(b). The volume ratio between salt and resin is fixed as described above, so each printed layer should have the same resin content but with various pore sizes. The layers printed by extra-fine ink should have more cohesion compared to the coarse ones since extra-fine ink has smaller size of defects. As for the two layers printed by different inks, the cohesion is increased if the top layer has smaller pore size and vice versa. Thus, besides the manipulation of pore size, this method can be applied to achieve gradient porosity and varied material properties such as strength and stiffness. Such a flexibility provides more control over the micro-porous structure for potential applications in tissue engineering and biomedical applications such as artificial joint containing rigid bones and soft cartilage.
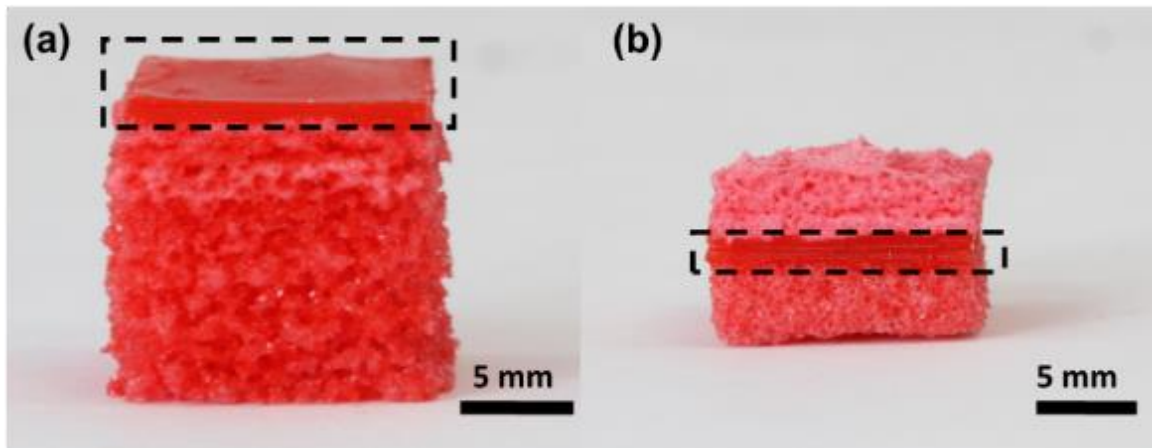

Figure 27. Pore size distribution can be controlled by switching ink during printing. (a) From bottom to top, a cube contains coarse, fine, extra-fine pores and solid roof. (b) Solid section is sandwiched between extra-fine (top) and fine (bottom) sections. Solid sections are marked in the black rectangle.

4.3.5   Shape Memory Effect

Shape memory effects in polymers are widely studied for their potential in biomedical devices.[4, 7, 14, 132, 133] In a typical shape memory cycle for amorphous

covalently network, a polymer is first heated to above its glass transition temperature (T_g) then deformed. The temperature is then lowered to below T_g, followed by removing the external load. The polymer will stay in the deformed shape, until the temperature increases to above T_g where the material recovers its original shape. Based on the DMA thermomechnical testing results as shown in Figure 35(a), the glass transition temperatures of the cured Standard Clear, PEGDA, and Spot-E are 66.5 °C, 69.2 °C, and 37.5 °C, respectively. Although both PEGDA and Standard Clear have T_g above the room temperature 22 °C, they are not as flexible as Spot-E as shown in Figure 35(b). Thus Spot-E ink is chosen to 3D print porous shape memory foams. A 15 mm tall porous cube was first printed as shown in Figure 28(a). To better fix the programmed shape, the compressed porous Spot-E cube was immersed in the ice water before it was put onto the hotplate that is 70°C as shown in Figure 28(b). An almost full recovery was observed after 2 min, as in Figure 28(c). The recovery loss may be due to the internal damage of the porous structure during the large compression in the shape programming step. It is important to note that this shape memory effect of the 3D printed porous sample is derived from the glass transition of the material, not from the porous structure. The entire shape memory test is recorded in video in the supplemental information online. Quantitative shape memory measurements were carried out by using DMA and the results of solid Spot-E strip, porous Spot-E cube and its cyclic testing results are shown in Figure 36. Since the T_g of Spot-E is very close to body temperature, the compressed cube can also be slowly recovered after placing it in the hand. Such thermo-triggered actuation of porous shape memory polymers can be applied to drug delivery and other biomedical applications.

Figure 28. Shape memory test showing (a) a 3D printed porous cube, (b) programmed into a compressed shape, and (c) recovered back to original shape.

4.3.6   Functional Composites

Another application of porous structures is to use them as templates for embedding other materials. For instance, the conductive ink can be integrated to enable conductivity in a 3D printed porous structure, which provides an alternative method to 3D print conductive objects. To prove this concept, two zigzag strips of Spot-E fine porous structure were 3D printed. The conductive ink was prepared by mixing PEDOT:PSS with 5% volume of ethylene glycol (EG) for 5 min. The addition of EG is for the purpose of improving conductivity.[134] The porous strips were then soaked in the conductive ink and dried in the ambient environment. The resistance of the porous strips was measured as 50 kΩ using a multimeter. The entire conductivity test can be found in video online in supplemental information and the SEM images of the conductive samples can be found in Figure 37. As shown in Figure 29(a), a LED bulb was first inserted into the two strips and it was then fully ignited at 32 V. Furthermore, the two strips are flexible and compressible, thus the LED bulb stayed on when loading force was applied on the strips in Figure 29(b). The conductivity is assumed to be independent of the polymer materials, which only provide interconnected pores. PEDOT:PSS was chosen for its ability to demonstrate flexibility with an easy operation. Apparently, a more conductive ink, such as silver inks,

can be used to greatly improve conductivity. As a result, this method merges 3D printing of porous structures with post-processing of conductive ink embedding and can be used to fabricate interdigitate circuits, capacitors and batteries.
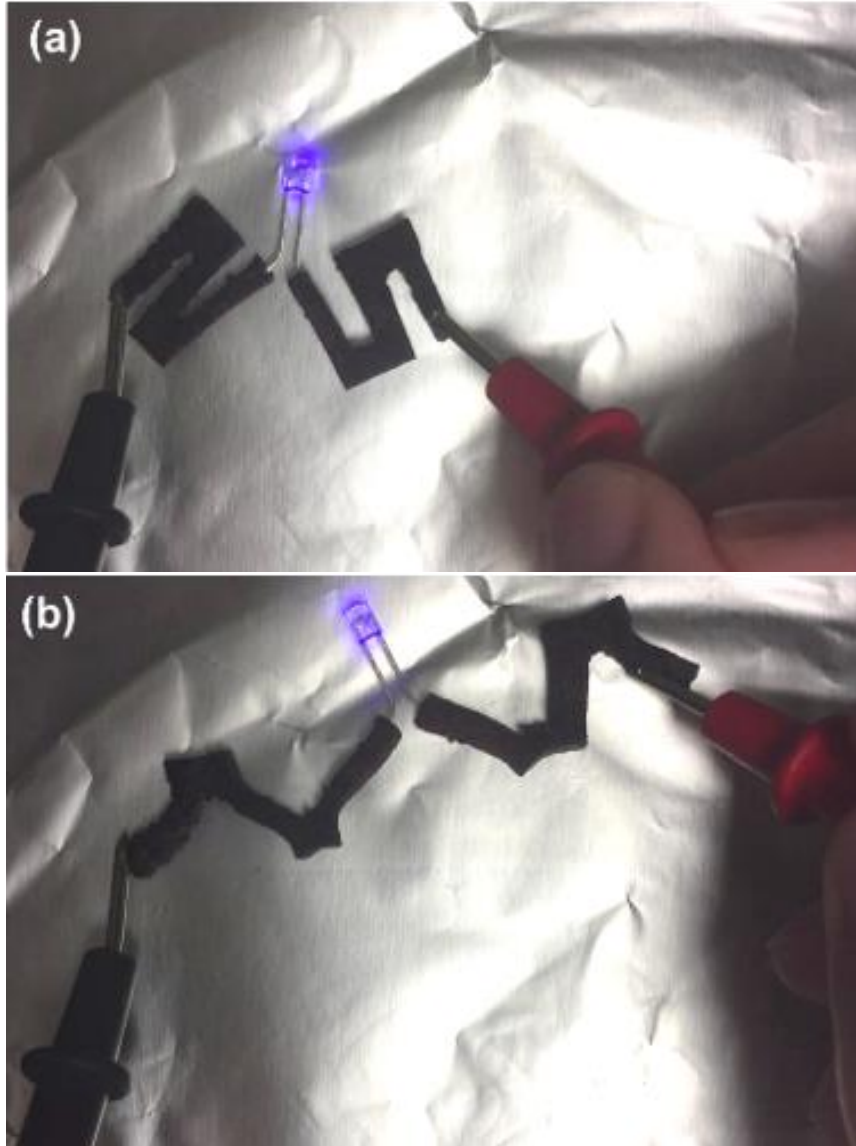

Figure 29. (a) LED bulb is lighted up when voltage is applied through porous polymer materials infiltrated with conductive ink and (b) the bulb keeps shining during stretching the porous conductive material.

The effective modulus of the porous structure can be further tuned by infiltrating another polymer. Here, we infiltrate the Spot-E porous cube by the Standard Clear resin,

followed by photocuring the infiltrated resin. The compression testing results for porous, solid and composite cubes were conducted using DMA with procedures described in the experimental section. Figure 30 presents the stress-strain curves showing the obvious difference of their elastic moduli. Compared to a solid Spot-E cube, the modulus of a porous Spot-E cube is significantly decreased from 4 MPa to 0.15 MPa.
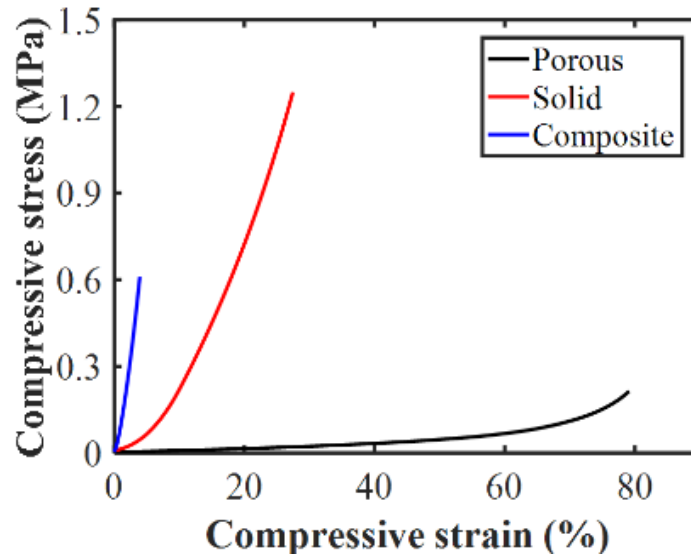

Figure 30. DMA comparison testing results among porous Spot-E cubes, solid Spot-E cubes and composite cubes made by infiltrating porous Spot-E cubes with Standard Clear resin.

Owing to the elastic property of Spot-E resin, the porous cubes can be compressed up to 80% strain and can recover to 90% of their original shape. After the Standard Clear resin was infiltrated and cured, the modulus of the composite cube dramatically increased to 15 MPa, which is two orders of magnitude higher than before infiltration. It should be noted that, even though the small infiltrated cubes (5 mm × 5 mm × 5 mm) were shined light for 5 min on each facet, the Standard Clear resin may still not be fully cured due to limited penetration of light. A more practical approach is to infiltrate the pores with thermally cured resins, such as PDMS, epoxy, *etc*. The example demonstrated here proves

the feasibility of creating functional polymer composites using 3D printed porous components as a starting template.

4.3.7 *Metallization of the Porous Polymeric Template*

All chemicals for electroless nickel deposition were obtained from Sigma-Aldrich (Milwaukee, WI) and the solutions are kept in beakers as shown in Figure 31(a). A 3D printed hollow cube was cut in half and one part was used as the specimen for electroless nickel deposition. The two half samples are compared side by side after each chemical treatment in Figure 31(b-f). To prepare the sample for electroless nickel deposition, it was first cleaned by immersing in an acetone batch with gentle agitation for 2 minutes. After rinsing in deionized (DI) water for 1 minute, the sample was immsersed in a 1 M NaOH solution for 2 minutes followed by rinsing in DI water for another 1 minute. Then, the sample was immersed in an aqueous solution containing 3.5 g/L of $SnCl_2 \cdot 2H_2O$ and 5.0 mL/L 37% HCl for 2 minutes to get the surface sensitized followed by rinsing in DI water for 1 minute. After sensitization, the sample was activated with palladium catalyst by immersing in an aqueous solution containing 0.5 g/L PdCl and 4.0 mL/L 37% HCl for 2 minutes followed by rinsing in DI water for 1 minute. After activation, the surface was metallized with nickel by immersing in a bath consisting of equal parts by volume of $NiCl_2$ and $NaPO_2H_2$. This step was performed at 80 °C with vigorous stirring at a magnetic hotplate. The thickness of the coated nickel was controlled by the operation time. The sample was finally removed and rinsed with DI water for 1 minute and allowed to air dry. This electroless nickel deposition procedure was followed by the work of Zheng et al. without the final polymer thermal decomposition that can be operated by heat-treating in a furnace in air at 500 °C for 4 hours.[135]
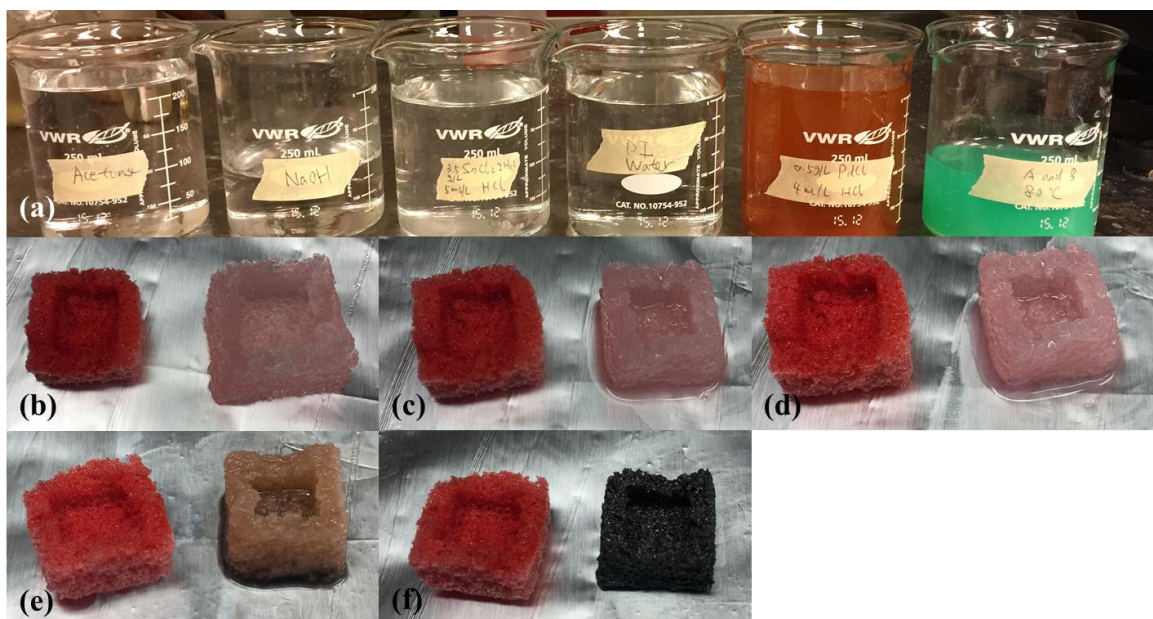
Figure 31. (a) All the chemical solutions required for electroless nickel plating. The chemical treated sample after (b) acetone, (c) NaOH, (d) sensitization, (e) activation and (f) nickel plating.

As shown in Figure 31(b), the acetone rinsed half has a faded colour compared to the original half and its volume is clearly expanded due to the solvent absorption. The size recovered to normal after rinsed by the base as shown in Figure 31(c) and no significant difference was observed after sensitization in Figure 31(d). After activation step, the colour changed to brown. The part was then placed in the final beaker for the actual nickel plating and it turned to completely black as an evidence of a successful metallization. The final parts became stiff and a small piece was cut for SEM images. As shown in Figure 32, the porous parts are coated with nickel. The coating, however, was not smooth since some of the regions have a slightly darker colour, indicating the final step time was not long enough or the coated area has a nonuniform thickness distribution.
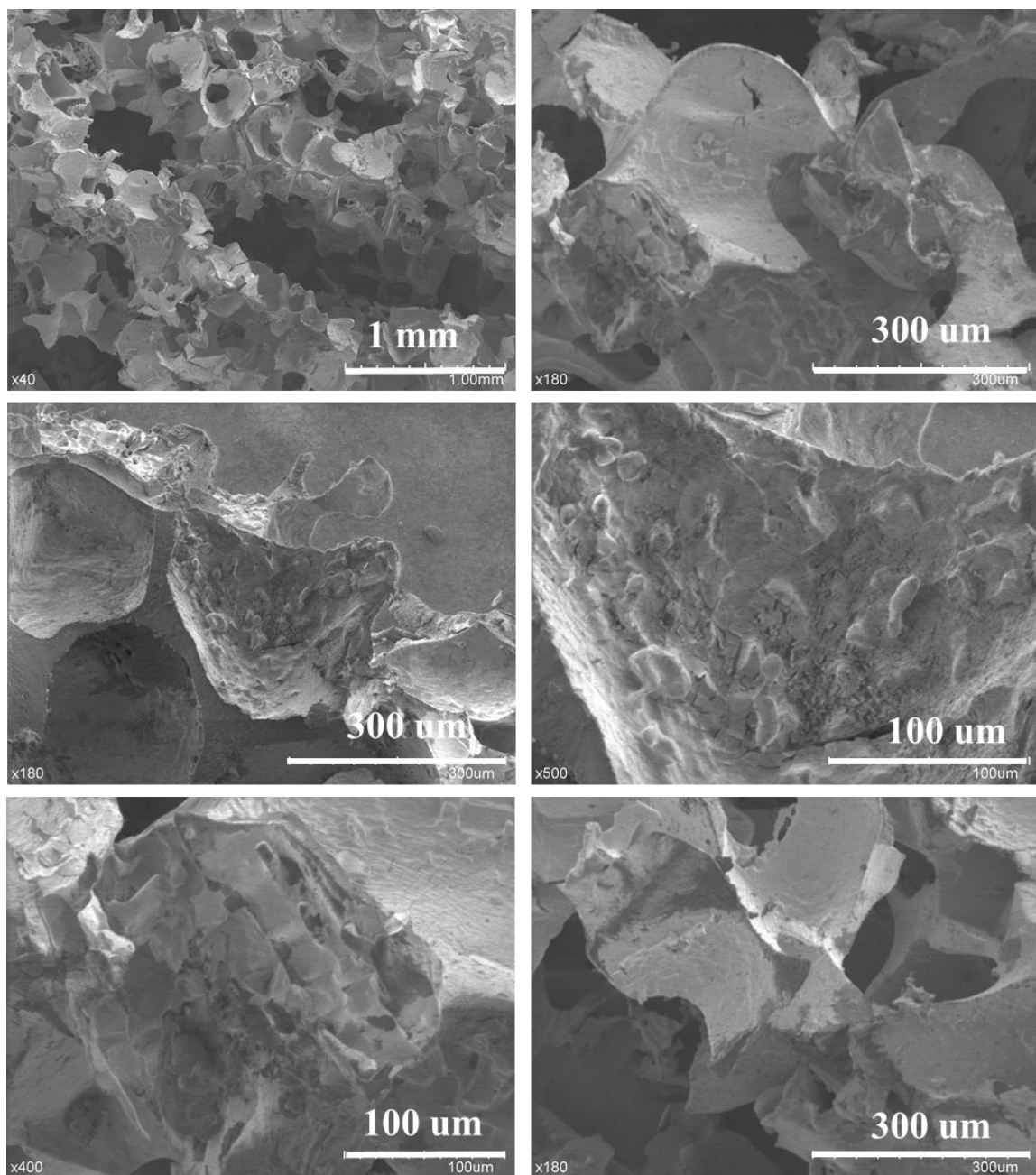
Figure 32. SEM images of the electroless nickel plated porous metallic foam using a 3D printed porous polymeric template.

4.4 Supplemental Materials

4.4.1 Rheological Behaviour of the Ink

Although the three base resins were measured successfully but the current setup cannot measure the viscosity of the ink properly as shown in Figure 33. Future study on the rheological behavior of the ink may require a rheometer with a sandblasted cylinder measuring system that can reduce wall slipping effects and is designed for measuring slurry.
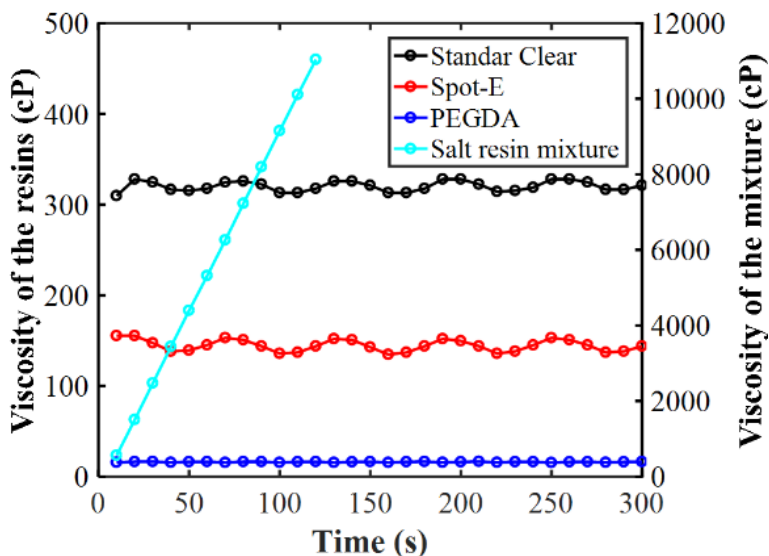

Figure 33. Rheological testing results showing the viscosity of Standard Clear resin, Spot-E resin and PEGDA resin are 320 cP, 145 cP and 16 cP, respectively. Salt resin mixture (volume ratio 10% salt to 90% Spot-E) is out of the range of our rheometer.

4.4.2 Photo-DSC tests

The photo-DSC tests were conducted by using DSC Q200 as introduced in the main text and the heat flow curves are plotted in Figure 34. The peak represents the heat flow from the tested sample during light irradiation, and an integral of the curve gives the heat

released during polymerization. After integral, the heat released from Standard Clear resin, PEGDA resin and Spot-E resin are 336 J/g, 513 J/g and 343 J/g, respectively. The heat released from Standard Clear ink, PEGDA ink and Spot-E ink are 58 J/g, 87 J/g and 51 J/g, respectively. Since the ink has salt particulates in its composition so that the measured heat released per mass need to be converted according to the mass ratio between salt and resin. After conversion, the heat released from the resins in Standard Clear ink, PEGDA ink and Spot-E ink value are 318 J/g, 495 J/g and 328 J/g, respectively. The extent of crosslinking for each ink is calculated by comparing the heat released from the pure resin and the heat released from the resin in the ink. As a result, the extent of crosslinking for Standard Clear ink, PEGDA ink and Spot-E ink are 94.6%, 96.4% and 95.6%, respectively. Therefore, we assume the influence of salts on the extent of photocrosslinking can be neglected.
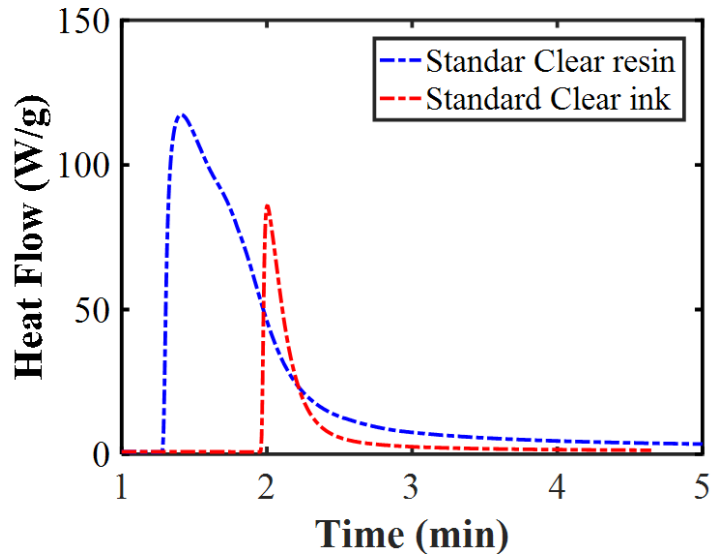

(a)
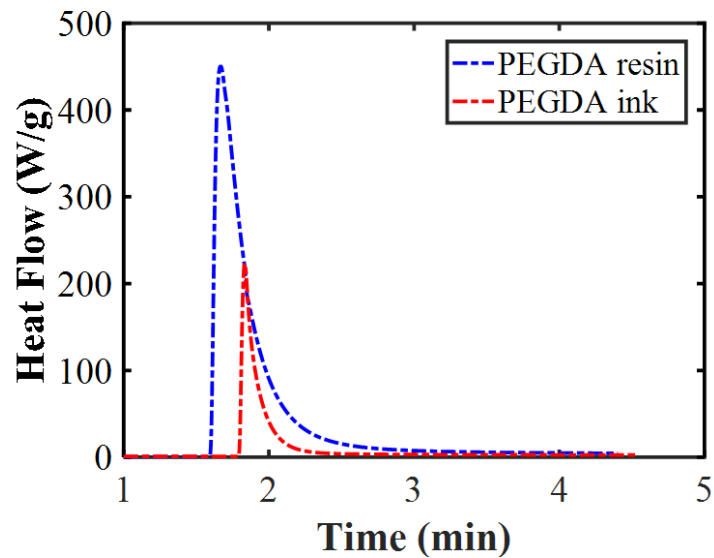
(b)
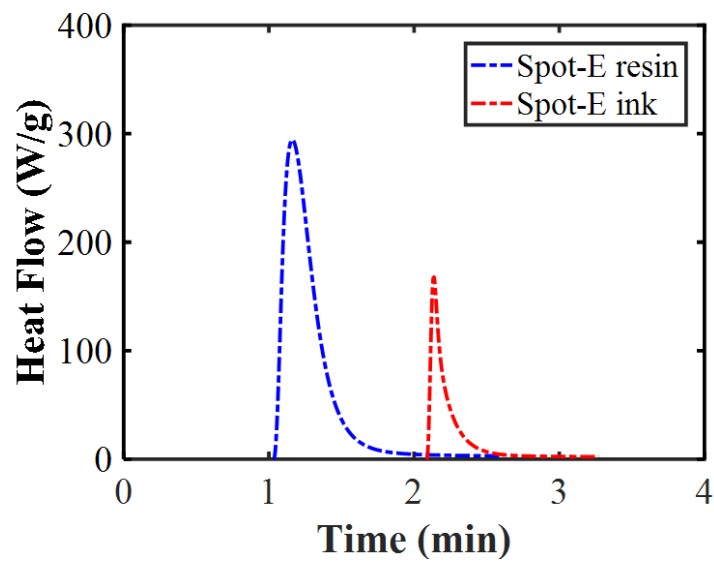
(c)

Figure 34. Photo-DSC results showing the resin in (a) Standard Clear ink, (b) PEGDA ink and (c) Spot-E ink have an extent of crosslinking higher about 95%.

4.4.3 *Thermomechanical and Tension Tests*

The procedures of the thermomechanical and the uniaxial tension tests are introduced in the experimental section of the manuscript. The solid lines in Figure 35 represents storage modulus of each resin and the dash lines are the corresponding normalized tan δ curves. Stretchability of Standard Clear and PEGDA is obviously smaller than Spot-E which is the reason Spot-E was chosen for printing most of the samples including shape memory foams.
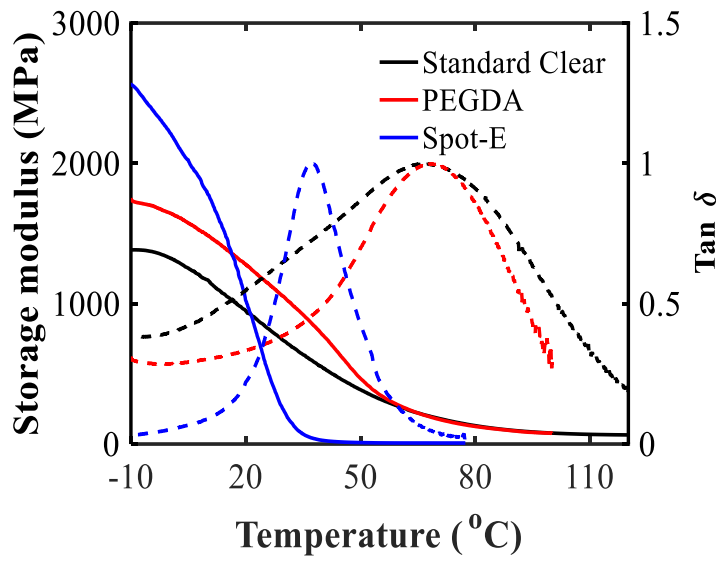
(a)
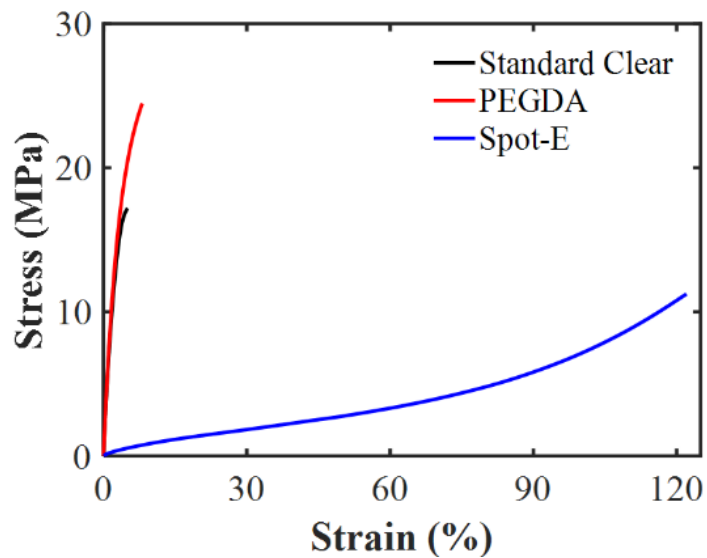
(b)

Figure 35. (a) Thermomechanical testing results showing the T_g of Standard Clear, PEGDA and Spot-E are 66.5 °C, 69.2 °C and 37.5 °C, respectively. (b) Tension testing results measured the modulus of Standard Clear, PEGDA and Spot-E are 640 MPa, 670 MPa and 4.5 MPa, respectively.
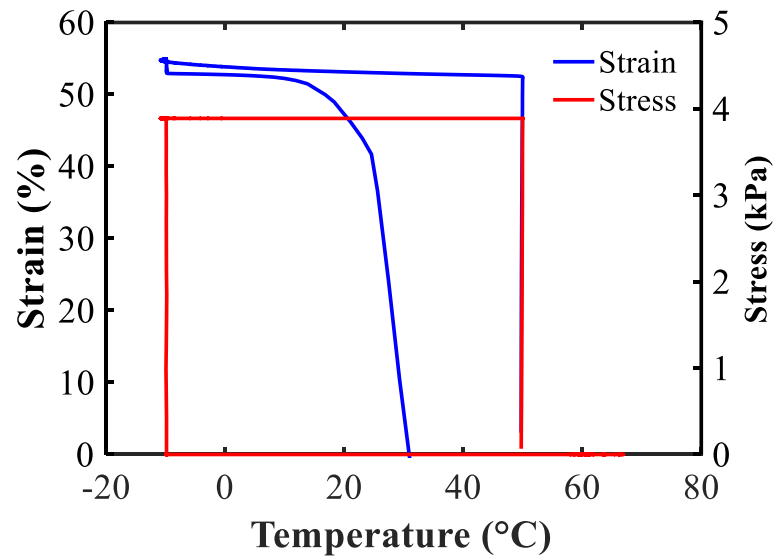
4.4.4 Shape Memory Tests

To quantitatively study the shape memory properties of 3D printed porous materials, such as recovery time and shape fixity, DMA tests have been conducted on both solid sample and porous sample for comparison. The first test was done by uniaxially stretching a solid strip made of Spot-E resin as shown in Figure 36(a). The strip was first loaded to 30% strain at 50 °C that is above its T_g and then the temperature was decreased to -10 °C at a rate of 3 °C min^{-1} while maintaining the displacement. After cooling down to -10 °C for 2 min, the applied load was released and the deformed shape was fixed at almost 100%. The temperature was then rapidly jumped to 70 °C and the original shape was recovered within 2 min. The second test was designed similarly but was conducted by compressing a porous cube (3D printed by fine ink). As shown in Figure 36(b), the porous cube was programmed by a 50% compression at 50 °C. The applied load was maintained the same while temperature was dropped down to -10 °C at the same rate as the first test. The shape fixity of porous cube after unloading at -10 °C was approximately 96% and the recovery time was shorter than 1 min after heating. The observation of a faster response time for the porous cube can be explained by the fact that the porous cube has a much larger surface area thus can be heated up much faster than the solid strip. As a comparison between Figure 36(a) and (b), the beginning trending of both recovery curves are almost the same before 15 °C but the curve of the porous cube keeps decreasing until fully recovery. This phenomenon may be caused by the growing pore volume during recovery that accelerates the heating of the material. To test the repeatability of shape memory foam, the same porous cube was tested for 8 cycles as shown in Figure 36(c). No obvious shape fixity change nor shape recovery loss was observed during the test. Interestingly, Figure

36 show that the porous cube recover faster than the solid strip. This might be due to that the porous cube can be heated faster than the solid strip.
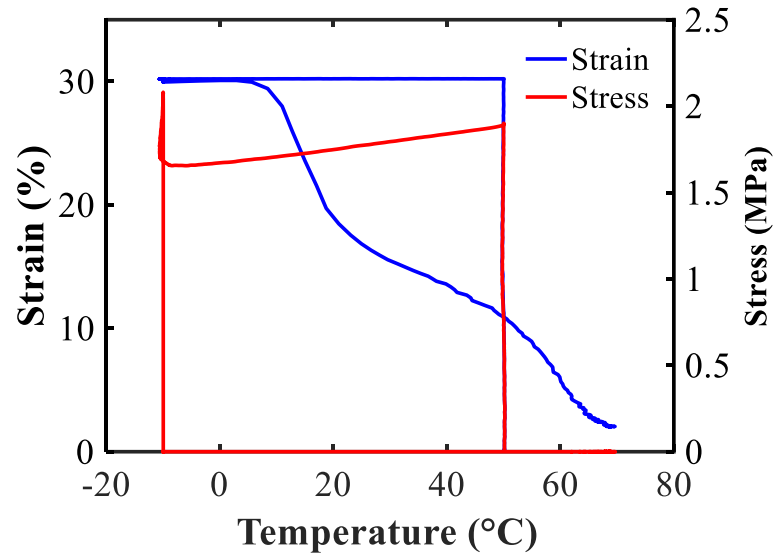
(a)

(b)
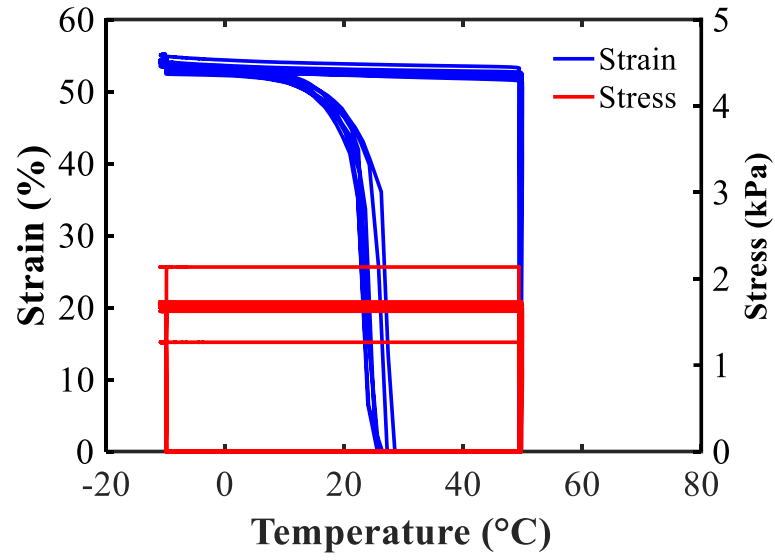
(c)

Figure 36. Shape memory testing results for (a) solid strip, (b) porous cube and (c) its cyclic testing results.

4.4.5 Infiltrated Conductive Sample Surface Profile

In order to check the conductive ink infiltration and coating quality, SEM images were taken on the infiltrated porous samples. However, comparing to the SEM images in Figure 37, the SEM images of the infiltrated sample show no difference, indicating a relatively complete wetting of PEDOT:PSS in the pores of the printed sample.

Figure 37. SEM images of PEDOT:PSS infiltrated samples.

4.5   Conclusions

We developed a new fabrication method to prepare porous polymeric components by combining DLP 3D printing method with salt leaching. The components are 3D printed using photocurable resin mixed with salt particulates. The pore sizes are determined by the salt particulate sizes, which can be tuned by grinding and sieving. Both FE-SEM a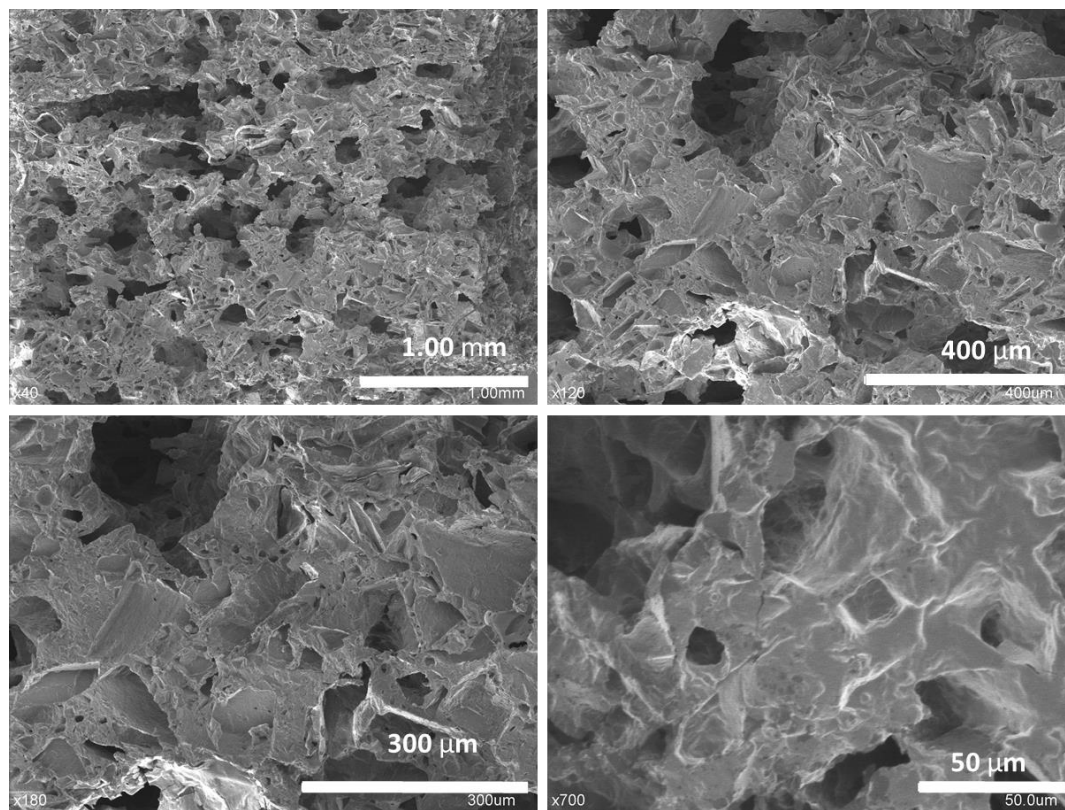nd Micro-CT were used to characterize the pore size, distribution and porosity of the porous sample. Various object shapes have been printed including cube, pyramid, sphere, heart, hollow cube with ball inside, trefoil knot and dual-pore scaffolds. DMA compression results show that the porous samples have significantly decreased effective modulus compared to the solid, while an infiltration of secondary photocurable resin can further tune the modulus of the composite. Compared to the previous methods, this method is very simple to implement for different photocurable resins to create 3D porous objects with complicated shapes. In addition, this new method has the advantages of self-supporting and can be used to print hollow components, especially the part with Droste effect (one object within another). Possibilities for applications such as tissue engineering, 3D printed shape memory foam and additive manufactured flexible conductive components have been demonstrated. Besides, various functionalities can be achieved depending on the properties of the photocurable resin used in the ink and the secondary embedded materials. The porous sample can also be chemical treated and be able to electroless nickel plated thus a porous metal can be printing assisted with random distributed pores. Some other potentially achievable applications include energy absorber, battery fabrication, and porous membranes for water purification.

CHAPTER 5. OVERALL CONCLUSIONS

The overall objective of this dissertation is to study the light interaction with polymers such as the complex photomechanical behaviors of photopolymers, and explore the multifunctionalities of the 3D printed porous photopolymers. The photomechanical study includes research of active network polymers through experimental and theoretical investigations. Two representative polymer systems are selected in this dissertation: light activated polymers and two-stage reactive polymers. Both polymers are light responsive and can perform certain functionalities upon irradiation. The research strategy includes experimental testing on the light responsive polymers and 3D printed polymeric structures, development of constitutive models to predict material behavior, and modification of the existing 3D printing methods to fabricate innovative structures.

Specifically, LAPs relax the internal stress and thus perform a shape morphing effect. Our contribution to this polymer system is the design of a laminated composite that can avoid the drawback of an external load requirement during actuation. The photomechanical model developed for this laminated composite helps to optimize the laminate parameters during fabrication. The study of oxygen inhibition on covalently adaptive networks (CANs), interfacial strength and molecular dynamic simulations on BERs have been conducted as well.[86, 87, 136, 137] The laminated composite has been examined to be able to achieve free-standing actuation. Other researches have been done on frontal photopolymerization and dessolvation induced origami by using DLP 3D printing method.[138, 139] To investigate the photoinduced viscoelastic behavior of the two-stage reactive polymers, we developed a photoviscoelastic model and validated the model

by comparing the simulation results with the experimental results. This polymer system is suitable for shape morphing and surface wrinkling applications. Photopolymerization is widely used in additive manufacturing and we modified 3D printing apparatus and ink formulation to fabricate innovative porous structures. Various photocurable monomers are mixed with salt particulates to 3D print porous polymeric materials. Different porous structures have been fabricated with interconnected pores. Besides the versatility of the inks and complex structures, multifunctionalities are demonstrated such as shape memory foam, conductive parts assisted by 3D printing, property change by secondary material infiltration, and porous metal polymer composite by metallization.

REFERENCES

[1]   A. Lendlein, S. Kelch, *Angew Chem Int Edit* **2002**, 41, 2034.

[2]   A. Lendlein, J. Canisius, J. Schulte, K. Kratz, *Smst-2003: Proceedings of the International Conference on Shape Memory and Superelastic Technologies* **2004**, 563.

[3]   A. Lendlein, S. Kelch, *Clin Hemorheol Micro* **2005**, 32, 105.

[4]   C. Liu, H. Qin, P. T. Mather, *Journal of Materials Chemistry* **2007**, 17, 1543.

[5]   H. J. Qi, T. D. Nguyen, F. Castro, C. M. Yakacki, R. Shandas, *Journal of the Mechanics and Physics of Solids* **2008**, 56, 1730.

[6]   D. Ratna, J. Karger-Kocsis, *J Mater Sci* **2008**, 43, 254.

[7]   P. T. Mather, X. Luo, I. A. Rousseau, *Annual Review of Materials Research* **2009**, 39, 445.

[8]   T. Xie, *Nature* **2010**, 464, 267.

[9]   T. Xie, *Polymer* **2011**, 52, 4985.

[10]   K. Yu, T. Xie, J. Leng, Y. Ding, H. J. Qi, *Soft Matter* **2012**, 8, 5687.

[11]   J. L. Hu, Y. Zhu, H. H. Huang, J. Lu, *Progress in Polymer Science* **2012**, 37, 1720.

[12]   M. Behl, K. Kratz, U. Noechel, T. Sauter, A. Lendlein, *Proc Natl Acad Sci U S A* **2013**, 110, 12555.

[13]   Y. Mao, J. M. Robertson, X. Mu, P. T. Mather, H. Jerry Qi, *Journal of the Mechanics and Physics of Solids* **2015**, 85, 219.

[14]   Q. Zhao, H. vvvidefviJ. Qi, T. Xie, *Progress in Polymer Science* **2015**, 49-50, 79.

[15]   Y. B. Lim, S. O. Han, H. U. Kong, Y. Lee, J. S. Park, B. Jeong, S. W. Kim, *Pharmaceut Res* **2000**, 17, 811.

[16]   Y. B. Lim, Y. H. Choi, J. S. Park, *J Am Chem Soc* **1999**, 121, 5633.

[17]   Y. H. Choi, F. Liu, J. S. Choi, S. W. Kim, J. S. Park, *Hum Gene Ther* **1999**, 10, 2657.

[18]   N. Murthy, J. R. Robichaud, D. A. Tirrell, P. S. Stayton, A. S. Hoffman, *J Control Release* **1999**, 61, 137.

[19]   L. B. Luo, M. Kato, T. Tsuruta, K. Kataoka, Y. Nagasaki, *Macromolecules* **2000**, 33, 4992.

[20]   M. Sardar, R. Agarwal, A. Kumar, M. N. Gupta, *Enzyme Microb Tech* **1997**, 20, 361.

[21]   L. H. Gan, Y. Y. Gan, G. R. Doon, *Macromolecules* **2000**, 33, 7893.

[22]   W. M. Huang, B. Yang, L. An, C. Li, Y. S. Chan, *Applied Physics Letters* **2005**, 86.

[23]   Y. C. Jung, H. H. So, J. W. Cho, *J Macromol Sci B* **2006**, 45, 453.

[24]   R. Mohr, K. Kratz, T. Weigel, M. Lucka-Gabor, M. Moneke, A. Lendlein, *P Natl Acad Sci USA* **2006**, 103, 3540.

[25]   P. R. Buckley, G. H. McKinley, T. S. Wilson, W. Small, W. J. Benett, J. P. Bearinger, M. W. McElfresh, D. J. Maitland, *Ieee T Bio-Med Eng* **2006**, 53, 2075.

[26]   A. M. Schmidt, *Macromolecular rapid communications* **2006**, 27, 1168.

[27]   U. N. Kumar, K. Kratz, W. Wagermaier, M. Behl, A. Lendlein, *Journal of Materials Chemistry* **2010**, 20, 3404.

[28]   V. Shibaev, A. Bobrovsky, N. Boiko, *Progress in Polymer Science* **2003**, 28, 729.

[29]   H. J. Andreas Lendlein, Oliver Ju¨ nger & Robert Langer, *Nature* **2005**, 434, 876.

[30]   H. Y. Jiang, S. Kelch, A. Lendlein, *Advanced Materials* **2006**, 18, 1471.

[31]   M. H. Li, P. Keller, *Philos Trans A Math Phys Eng Sci* **2006**, 364, 2763.

[32]   C. J. Kloxin, T. F. Scott, H. Y. Park, C. N. Bowman, *Adv Mater* **2011**, 23, 1977.

[33]   K. M. Lee, H. Koerner, R. A. Vaia, T. J. Bunning, T. J. White, *Soft Matter* **2011**, 7, 4318.

[34]   J. Ryu, M. D'Amato, X. Cui, K. N. Long, H. Jerry Qi, M. L. Dunn, *Applied Physics Letters* **2012**, 100, 161908.

[35]   Y. Liu, J. K. Boyles, J. Genzer, M. D. Dickey, *Soft Matter* **2012**, 8, 1764.

[36]   Y. Liu, M. Miskiewicz, M. J. Escuti, J. Genzer, M. D. Dickey, *Journal of Applied Physics* **2014**, 115, 204911.

[37]   Y. Liu, J. Genzer, M. D. Dickey, *Progress in Polymer Science* **2016**, 52, 79.

[38]   A. M. Hubbard, R. W. Mailen, M. A. Zikry, M. D. Dickey, J. Genzer, *Soft Matter* **2017**, 13, 2299.

[39]   D. J. Broer, G. N. Mol, J. A. M. M. van Haaren, J. Lub, *Advanced Materials* **1999**, 11, 573.

[40]   T. J. White, N. V. Tabiryan, S. V. Serak, U. A. Hrozhyk, V. P. Tondiglia, H. Koerner, R. A. Vaia, T. J. Bunning, *Soft Matter* **2008**, 4, 1796.

[41]   C. L. van Oosten, D. Corbett, D. Davies, M. Warner, C. W. M. Bastiaansen, D. J. Broer, *Macromolecules* **2008**, 41, 8592.

[42]   T. J. White, S. V. Serak, N. V. Tabiryan, R. A. Vaia, T. J. Bunning, *Journal of Materials Chemistry* **2009**, 19, 1080.

[43]   T. J. White, S. A. Cazzell, A. S. Freer, D. K. Yang, L. Sukhomlinova, L. Su, T. Kosa, B. Taheri, T. J. Bunning, *Adv Mater* **2011**, 23, 1389.

[44]   D. Liu, C. W. Bastiaansen, J. M. den Toonder, D. J. Broer, *Angew Chem Int Ed Engl* **2012**, 51, 892.

[45]   D. Liu, C. W. Bastiaansen, J. M. den Toonder, D. J. Broer, *Langmuir : the ACS journal of surfaces and colloids* **2013**, 29, 5622.

[46]   T. Ikeda, M. Nakano, Y. L. Yu, O. Tsutsumi, A. Kanazawa, *Advanced Materials* **2003**, 15, 201.

[47]   T. F. Scott, A. D. Schneider, W. D. Cook, C. N. Bowman, *Science* **2005**, 308, 1615.

[48]   T. F. Scott, R. B. Draughon, C. N. Bowman, *Advanced Materials* **2006**, 18, 2128.

[49]   Y. Mao, Z. Ding, C. Yuan, S. Ai, M. Isakov, J. Wu, T. Wang, M. L. Dunn, H. J. Qi, *Scientific reports* **2016**, 6, 24761.

[50]   C. Colosi, S. R. Shin, V. Manoharan, S. Massa, M. Costantini, A. Barbetta, M. R. Dokmeci, M. Dentini, A. Khademhosseini, *Adv Mater* **2016**, 28, 677.

[51]   J. P. Armstrong, M. Burke, B. M. Carter, S. A. Davis, A. W. Perriman, *Adv Healthc Mater* **2016**, 5, 1724.

[52]   K. A. Homan, D. B. Kolesky, M. A. Skylar-Scott, J. Herrmann, H. Obuobi, A. Moisan, J. A. Lewis, *Scientific reports* **2016**, 6, 34845.

[53]   J. R. Tumbleston, D. Shirvanyants, N. Ermoshkin, R. Janusziewicz, A. R. Johnson, D. Kelly, K. Chen, R. Pinschmidt, J. P. Rolland, A. Ermoshkin, E. T. Samulski, J. M. DeSimone, *Science* **2015**, 347, 1349.

[54]   J. W. Stansbury, M. J. Idacavage, *Dental Materials* **2016**, 32, 54.

[55]   J. Wallace, M. O. Wang, P. Thompson, M. Busso, V. Belle, N. Mammoser, K. Kim, J. P. Fisher, A. Siblani, Y. S. Xu, J. F. Welter, D. P. Lennon, J. Y. Sun, A. I. Caplan, D. Dean, *Biofabrication* **2014**, 6.

[56]   Z. Ding, C. Yuan, X. Peng, T. Wang, H. J. Qi, M. L. Dunn, *Sci Adv* **2017**, 3, e1602890.

[57]   K. N. Long, M. L. Dunn, T. F. Scott, L. P. Turpin, H. J. Qi, *Journal of Applied Physics* **2010**, 107, 053519.

[58]   K. N. Long, T. F. Scott, M. L. Dunn, H. Jerry Qi, *International Journal of Solids and Structures* **2011**, 48, 2089.

[59]   J. Ma, X. Mu, C. N. Bowman, Y. Sun, M. L. Dunn, H. J. Qi, D. Fang, *Journal of the Mechanics and Physics of Solids* **2014**, 70, 84.

[60]   D. P. Nair, N. B. Cramer, J. C. Gaipa, M. K. McBride, E. M. Matherly, R. R. McLeod, R. Shandas, C. N. Bowman, *Advanced Functional Materials* **2012**, 22, 1502.

[61]   D. P. Nair, N. B. Cramer, M. K. McBride, J. C. Gaipa, R. Shandas, C. N. Bowman, *Polymer (Guildf)* **2012**, 53, 2429.

[62]   D. P. Nair, N. B. Cramer, M. K. McBride, J. C. Gaipa, N. C. Lee, R. Shandas, C. N. Bowman, *Macromol Symp* **2013**, 329, 101.

[63]   H. Peng, D. P. Nair, B. A. Kowalski, W. Xi, T. Gong, C. Wang, M. Cole, N. B. Cramer, X. Xie, R. R. McLeod, C. N. Bowman, *Macromolecules* **2014**, 47, 2306.

[64]   D. J. Glugla, M. D. Alim, K. D. Byars, D. P. Nair, C. N. Bowman, K. K. Maute, R. R. McLeod, *ACS applied materials & interfaces* **2016**, 8, 29658.

[65]   K. N. Long, M. L. Dunn, H. Jerry Qi, *International Journal of Plasticity* **2010**, 26, 603.

[66]   K. N. Long, Dunn, M.L., Scott, T.F., Qi, H. J., *International Journal of Structural Changes in Solids* **2010**, 2, 41.

[67]   R. Long, H. J. Qi, M. L. Dunn, *Soft Matter* **2013**, 9, 4083.

[68]   J. S. Smith, *Unpublished manuscript, 2005.* http://www.bitsofsmith.co.uk/history.htm. *First edition published as Booklet 1 in a series by the British Origami Society, 1972.*

[69]   R. J. Lang, *Phys World* **2007**, 20, 30.

[70]   E. D. Demaine, M. L. Demaine, G. Konjevod, R. J. Lang, *Lect Notes Comput Sc* **2009**, 5878, 1074.

[71]   V. N. Dubey, L. S. Dai, *Ind Robot* **2006**, 33, 82.

[72]   W. N. Wu, Z. You, *P Roy Soc a-Math Phy* **2011**, 467, 2561.

[73]   C. L. Randall, E. Gultepe, D. H. Gracias, *Trends Biotechnol* **2012**, 30, 138.

[74]   M. Jamal, E. Gultepe, K. Laflin, D. Gracias, *Abstracts of Papers of the American Chemical Society* **2012**, 243.

[75]   D. H. Gracias, *Current Opinion in Chemical Engineering* **2013**, 2, 112.

[76]   P. Parkinson, Y. H. Lee, L. Fu, S. Breuer, H. H. Tan, C. Jagadish, *Nano letters* **2013**, 13, 1405.

[77]   S. M. Felton, M. T. Tolley, B. Shin, C. D. Onal, E. D. Demaine, D. Rus, R. J. Wood, *Soft Matter* **2013**, 9, 7688.

[78]   Q. Ge, H. J. Qi, M. L. Dunn, *Applied Physics Letters* **2013**, 103, 131901.

[79]   Q. Ge, C. K. Dunn, H. J. Qi, M. L. Dunn, *Smart Materials & Structures* **2014**, 23, 094007.

[80]   X. Mu, N. Sowan, J. A. Tumbic, C. N. Bowman, P. T. Mather, H. J. Qi, *Soft Matter* **2015**, 11, 2673.

[81]   C. J. Kloxin, T. F. Scott, C. N. Bowman, *Macromolecules* **2009**, 42, 2551.

[82]   K. N. Long, T. F. Scott, H. Jerry Qi, C. N. Bowman, M. L. Dunn, *Journal of the Mechanics and Physics of Solids* **2009**, 57, 1103.

[83]   K. K. Westbrook, V. Parakh, T. Chung, P. T. Mather, L. C. Wan, M. L. Dunn, H. J. Qi, *Journal of Engineering Materials and Technology* **2010**, 132, 041010.

[84]   R. Long, H. J. Qi, M. L. Dunn, *Journal of the Mechanics and Physics of Solids* **2013**, 61, 2212.

[85]   M. D. Goodner, C. N. Bowman, *Chem Eng Sci* **2002**, 57, 887.

[86]   Z. Zhao, X. Mu, N. Sowan, Y. Pei, C. N. Bowman, H. Jerry Qi, D. Fang, *Soft Matter* **2015**, 11, 6134.

[87]   Z. Zhao, X. Mu, J. Wu, H. J. Qi, D. Fang, *Extreme Mechanics Letters* **2016**, 9, 108.

[88]   W. X. Xi, H. Y. Peng, A. Aguirre-Soto, C. J. Kloxin, J. W. Stansbury, C. N. Bowman, *Macromolecules* **2014**, 47, 6159.

[89]   S. J. Ma, S. J. Mannino, N. J. Wagner, C. J. Kloxin, *Acs Macro Letters* **2013**, 2, 474.

[90]   M. Podgorski, D. P. Nair, S. Chatani, G. Berg, C. N. Bowman, *ACS applied materials & interfaces* **2014**, 6, 6111.

[91]   A. A. Alzahrani, D. P. Nair, D. J. Smits, M. Saed, C. M. Yakacki, C. N. Bowman, *Chem Mater* **2014**, 26, 5303.

[92]   C. M. Yakacki, M. Saed, D. P. Nair, T. Gong, S. M. Reed, C. N. Bowman, *RSC Adv.* **2015**, 5, 18997.

[93]   X. Fernández-Francos, A.-O. Konuray, A. Belmonte, S. De la Flor, À. Serra, X. Ramis, *Polym. Chem.* **2016**, 7, 2280.

[94]   J. S. Sodhi, I. J. Rao, *Int J Eng Sci* **2010**, 48, 1576.

[95]   L. W. Hill, *Progress in Organic Coatings* **1997**, 31, 235.

[96]   C. N. B. K.S. Anseth, *Polym. React. Eng. 1* **(1992–1993)**

4520–4999.

[97]   T. M. Lovestead, A. K. O'Brien, C. N. Bowman, *Journal of Photochemistry and Photobiology A: Chemistry* **2003**, 159, 135.

[98]   T. M. Lovestead, K. A. Berchtold, C. N. Bowman, *Macromolecular Theory and Simulations* **2002**, 11, 729.

[99]   E. M. Arruda, M. C. Boyce, *Journal of the Mechanics and Physics of Solids* **1993**, 41, 389.

[100]   M. Rubinstein, R. H. Colby, *Polymer Physics*, Oxford University Press, New York 2003.

[101]   M. L. Williams, R. F. Landel, J. D. Ferry, *Phys Rev* **1955**, 98, 1549.

[102]   E. A. Di Marzio, A. J. M. Yang, *J Res Natl Inst Stan* **1997**, 102, 135.

[103]   L. R. G. Treloar, *The Physics of Rubber Elasticity*, Clarendon Press, Oxford 1958.

[104]   X. Mu, T. Bertron, C. Dunn, H. Qiao, J. Wu, Z. Zhao, C. Saldana, H. J. Qi, *Mater. Horiz.* **2017**, 4, 442.

[105]   H. Cong, J. Wang, B. Yu, J. Tang, *Soft Matter* **2012**, 8, 8835.

[106]   I. Pulko, J. Wall, P. Krajnc, N. R. Cameron, *Chem-Eur J* **2010**, 16, 2350.

[107]   M. R. Abidian, D. H. Kim, D. C. Martin, *Advanced Materials* **2006**, 18, 405.

[108]   X. Y. Yang, L. T. Chen, B. Huang, F. Bai, X. L. Yang, *Polymer* **2009**, 50, 3556.

[109]   Y. J. Zhang, S. P. Wang, M. Eghtedari, M. Motamedi, N. A. Kotov, *Advanced Functional Materials* **2005**, 15, 725.

[110]   S. D. Kimmins, N. R. Cameron, *Advanced Functional Materials* **2011**, 21, 211.

[111]   C. D. Wood, B. Tan, A. Trewin, F. Su, M. J. Rosseinsky, D. Bradshaw, Y. Sun, L. Zhou, A. I. Cooper, *Advanced Materials* **2008**, 20, 1916.

[112]   Y. Kou, Y. H. Xu, Z. Q. Guo, D. L. Jiang, *Angew Chem Int Edit* **2011**, 50, 8753.

[113]   Y. Wang, C. C. He, W. H. Xing, F. B. Li, L. Tong, Z. Q. Chen, X. Z. Liao, M. Steinhart, *Advanced Materials* **2010**, 22, 2068.

[114]   D. C. Wu, F. Xu, B. Sun, R. W. Fu, H. K. He, K. Matyjaszewski, *Chemical reviews* **2012**, 112, 3959.

[115]   Y. S. Nam, J. J. Yoon, T. G. Park, *J Biomed Mater Res* **2000**, 53, 1.

[116]   A. Salerno, M. Oliviero, E. Di Maio, S. Iannace, P. A. Netti, *J Mater Sci-Mater M* **2009**, 20, 2043.

[117]   H. Lo, M. S. Ponticiello, K. W. Leong, *Tissue Eng* **1995**, 1, 15.

[118]   Y. S. Nam, T. G. Park, *Biomaterials* **1999**, 20, 1783.

[119]   W. L. Li, W. J. Zhang, X. Q. Dong, L. S. Yan, R. G. Qi, W. C. Wang, Z. G. Xie, X. B. Jing, *Journal of Materials Chemistry* **2012**, 22, 17445.

[120]   M. Susec, S. C. Ligon, J. Stampfl, R. Liska, P. Krajnc, *Macromolecular rapid communications* **2013**, 34, 938.

[121]   D. Maniglio, Y. Ding, L. Wang, C. Migliaresi, *Polymer* **2011**, 52, 5102.

[122]   J. S. Arora, T. Ponnusamy, R. Zheng, P. Venkataraman, S. R. Raghavan, D. Blake, V. T. John, *Soft Matter* **2015**.

[123]   Q. Hou, D. W. Grijpma, J. Feijen, *Biomaterials* **2003**, 24, 1937.

[124]   X. H. Yan, G. J. Liu, M. Dickey, C. G. Willson, *Polymer* **2004**, 45, 8469.

[125]   I. Cooperstein, M. Layani, S. Magdassi, *J Mater Chem C* **2015**, 3, 2040.

[126] H. Lee, N. X. Fang, *Jove-J Vis Exp* **2012**.

[127] N. A. Sears, P. S. Dhavalikar, E. M. Cosgriff-Hernandez, *Macromolecular rapid communications* **2016**.

[128] S. C. Cox, J. A. Thornby, G. J. Gibbons, M. A. Williams, K. K. Mallick, *Mat Sci Eng C-Mater* **2015**, 47, 237.

[129] H. Qiao, S. Basu, C. Saldana, *Procedia CIRP* **2016**, 45, 335.

[130] N. A. Alcantar, E. S. Aydil, J. N. Israelachvili, *J Biomed Mater Res* **2000**, 51, 343.

[131] S. Mohanty, K. Sanger, A. Heiskanen, J. Trifol, P. Szabo, M. Dufva, J. Emneus, A. Wolff, *Mater Sci Eng C Mater Biol Appl* **2016**, 61, 180.

[132] C. M. Yakacki, R. Shandas, C. Lanning, B. Rech, A. Eckstein, K. Gall, *Biomaterials* **2007**, 28, 2255.

[133] W. G. Yang, H. B. Lu, W. M. Huang, H. J. Qi, X. L. Wu, K. Y. Sun, *Polymers* **2014**, 6, 2287.

[134] X. Crispin, F. L. E. Jakobsson, A. Crispin, P. C. M. Grim, P. Andersson, A. Volodin, C. van Haesendonck, M. Van der Auweraer, W. R. Salaneck, M. Berggren, *Chem Mater* **2006**, 18, 4354.

[135] X. Zheng, H. Lee, T. H. Weisgraber, M. Shusteff, J. DeOtte, E. B. Duoss, J. D. Kuntz, M. M. Biener, Q. Ge, J. A. Jackson, S. O. Kucheyev, N. X. Fang, C. M. Spadaccini, *Science* **2014**, 344, 1373.

[136] H. Yang, K. Yu, X. Mu, X. Shi, Y. Wei, Y. Guo, H. J. Qi, *Soft Matter* **2015**, 11, 6305.

[137] H. Yang, K. Yu, X. Mu, Y. Wei, Y. Guo, H. J. Qi, *RSC Adv.* **2016**, 6, 22476.

[138] Z. Zhao, J. Wu, X. Mu, H. Chen, H. J. Qi, D. Fang, *Macromolecular rapid communications* **2016**.

[139]   Z. Zhao, J. Wu, X. Mu, H. Chen, H. J. Qi, D. Fang, *Sci Adv* **2017**, 3, e1602326.